Dynamics of Bose-Einstein Condensate in Linear and Non-Linear Regime

A Thesis

Submitted in partial fulfillment of the requirements of the degree of

Doctor of Philosophy
in Physics

by

Gunjan Verma
Registeration ID 20123231

Department of Physics
Indian Institute of Science Education and Research
Pune-411008, India
2018

Dedicated to

My Mother
"For her unbreakable faith, encouragement, friendship, love and courage which always inspired me"

My Father
"For his unconditional love, encouragement and strength to face the hardest times gracefully and fly high"

My Teachers
"Sunder Singh Verma: the very first guru, the most precious friend and philosopher who brought the best out of me"
"Reeta Sharma: who taught me to be bold in my actions and to live life to the fullest"
"Pranjal Trivedi: who always motivated and believed in me. A person who infected me with his enthusiasm and love for physics"
"Umakant Rapol and Rejish Nath: who transformed me from a student to a researcher and taught me to never give up even in the worst situations"

My love, Naren
"His simplicity and love has always guided me to be a better human being"

CERTIFICATE

Certified that the work incorporated in the thesis entitled "Dynamics of Bose-Einstein Condensate in Linear and Non-Linear Regime" submitted by Ms. Gunjan Verma was carried out by the candidate, under my supervision. The work presented here or any part of it has not been included in any other thesis submitted previously for the award of any degree or diploma from any other University or institution.

U.D.

Dr. Umakant D. Rapol

(Supervisor)

Date: 8th March, 2019

Declaration

I declare that this written submission represents my ideas in my own words and where others ideas have been included, I have adequately cited and referenced the original sources. I also declare that I have adhered to all principles of academic honesty and integrity and have not misrepresented or fabricated or falsified any idea/data/fact/source in my submission. I understand that violation of the above will be cause for disciplinary action by the Institute and can also evoke penal action from the sources which have thus not been properly cited or from whom proper permission has not been taken when needed. The work presented in this thesis was done under the guidance of Dr. Umakant D. Rapol and in collaboration with Dr. Rejish Nath, at the Indian Institute of Science Education and Research, Pune.

(Gunjan Verma)

Roll No. 20123231

Date: 8th March, 2019

Acknowledgements

I am deeply thankful to many people for the successful completion of my PhD thesis. First and foremost I am grateful to my PhD supervisor, Dr Umakant Rapol whose contagious enthusiasm and inquisitive nature for experiments and endless patience with his students make him close to an ideal mentor. I want to thank him for introducing me to the exciting field of ultracold atoms and giving me an opportunity to work in his lab. He has always been encouraging, approachable and understanding throughout out the ups and downs of my PhD.

I am also indebted to Dr Rejish Nath for his endless support and motivation. I thank him for giving me an opportunity to explore the world of numerical simulations where I had full freedom to explore my imaginations and understand my subject in a better way. I will always cherish the stimulating scientific discussions I had with him. Those discussions contributed to the most pleasant time of my PhD. I truly enjoyed learning the subject under him.

I am thankful to my Research Advisory committee (Dr Rejish Nath and Dr Shivprasad Patil) for evaluating my research yearly and providing fruitful suggestions to improve it further. I thank the Department of Science and Technology for funding our strontium project.

I thank IISER Pune for providing the PhD fellowship. I am grateful to the administration and academic staff (Prabhakar, Tushar, Nayana, Sayalee) for helping me with many documents and thesis submission process. I want to thank technical officer Nilesh Dumbre and technical assistant Prashant Kale for aiding me during the experiments.

I am grateful to Italian Physical Society for giving me an opportunity and financially supporting my visit to attend “Enrico Fermi School” on “Atom

Interferometry" in 2013. I am thankful to IISER Pune for providing me with travel support for the same.

I thank all my lab members who made this journey not only smooth but memorable. When I joined the lab, Sunil, Noaman, Sindhu and Sumit helped me to get acquainted with the lab. I am thankful to Noaman who invested his time in explaining to me the working of the system, and I remember he was the one who entertained most of my questions regarding the experiment. I am thankful to Chetan who is the dearest, reliable and most lovable lab member of our lab. Working with him in building up the strontium setup has been a memorable and exciting experience, and I will always look forward to work with him. I acknowledge Jay for helping me to set up and carry out the "Bouncing BEC" experiment and reviewing my thesis. I thank Sainath for helping to improve my computer programs and to work with the Arduino Board. I will miss the days where I, Chetan and Sai watched Mahabharat episodes to release our stress. I want to thank Jithin (the youngest lab member during my tenure) who always kept the lab environment lively and stimulated. I want to thank Chinmayee, Yashwant, Ankita and Supriti who became valuable friends over the last three years. I want to thank the young members of our lab (Kushal, Shivsagar, Pranab and Korak) who never refrained from extending help at any time. I will cherish all the time and memories I spent with my lab members on and off the experiments; they all have been very supportive during this long journey.

I would like to thank all my friends from IISER (Nishtha, Himani, Jyoti, Manna, Harshini, Babar, Sanku, Panja, Shishir, Tanu, Daanveer, Adarsh, Sharma, Namrata, Charu, Bag and many more), NCRA and IUCAA (Jyotirmay (Doda), Samir (kaka), Sushma, Naina, Naidu, Rahul, Prakash, Binny, Sravani) who made my stay during my PhD a pleasant experience with various kinds of discussions and chats over tea and dinner, birthday celebrations, trekking, movie, shopping, cooking, lunch at Tamil mess etc. I especially thank Himani for turning me into a health-conscious person; I truly enjoyed my work out sessions at the gym with her. I will cherish the memories of evening walks in Pune university campus, tea time at Tapari and Chef's Cafe, dinner time at Sukanta and Naren's flat which consisted of mainly scientific and philosophical discussions with Samir, Doda and Naren. I would also like to thank my good friends Bharat and Ishita who remained in touch since college days. I missed them during the ups and downs of my PhD.

I heartfully thank Gopi bhiya and his family for taking care of me like their kids. His family will always remain for me a home away from home. The quality time spent while playing and studying with the kids, eating delicious food in the fresh air of selfless love and welcoming gesture is something which could never be forgotten.

I would like to thank my teachers who believed in me. First and foremost, I would like to acknowledge Sunder Singh Verma. He deserves a big thank you. He is my closest friend and guide. I am grateful to Reeta Sharma who came in my life during class X; I honestly love her immortal spirit and confidence. She has been a great teacher and friend. I want to thank Dr. Pranjal Trivedi and Dr. Agam Kumar Jha who not only taught me during my BSc but made me learn how to enjoy Physics.

In the end I grateful to parents for their love and support. Without their guidance, I would have never reached this stage. I thank my lovely sisters (Nisha, Himanshi, Chander) for always being there for me. I acknowledge the young member of the family Nanhi and Manhi, although I got very less time to spend with them, but it was lovely to play and learn with them. I am hugely thankful to my husband Naren, who has contributed the most to this beautiful journey. He was always there to listen to my problems, to encourage and to calm me down. I enjoyed discussing my work in detail with him. He was invariably there to provide fruitful suggestions for my work. His will to change things for better always aspire me to do good. He has been a fantastic friend, philosopher and scientist to guide me throughout my PhD.

Gunjan Verma
8th March 2019, Pune

Abstract

The fascinating field of exploring non-linear systems exhibits rich dynamics and these systems are found in almost every part of nature, whether it is the periodic beating of the heart, the ripples of sand dunes, complex shapes in snowflakes, or the existence of stripes on Jupiter and on animals. Beyond rich spatial and temporal patterns, nonlinearity present in any system can lead to the formation and evolution of localized structures which have unusual features such as solitons and vortices.

Solitons are spatially localized structures or waves which arise due to the balance of dispersion and nonlinearity in a system. These structures maintain their shape during propagation, are remarkably stable against any perturbations or mutual collision, and show particle-like properties. In general, solitons underlie the understanding of tidal bores, cyclones, massive ocean waves like tsunamis, signal conduction in neurons, and natural phenomena such as “Morning Glory” (hundreds of kilometers of cloud waves). Solitons have been actively studied in many different domains including in mathematics and physics (such as in the context of the solution of the Korteweg-de Vries equation, in shallow water, in magnetic thin films and optical fibers). Solitons have given a massive impetus to today’s telecommunications industry due to the ability of optical pulses to propagate as solitons for vast distances without significant loss or dispersion.

In this thesis, we explored, through experiments and numerical simulations, the behaviour and dynamics of the Bose-Einstein Condensate (BEC) in two different regimes: linear (interactions in the system are negligible) and non-linear regime (interactions in the system becomes dominant). A BEC of dilute atomic vapor not only provides a clean and well-controlled environment to study a variety of physics problems of superfluid systems including

solitons and vortices but also opens up avenues to investigate the interface between the quantum and the classical systems.

While probing the nonlinear regime of the condensate (through numerical simulations), we focused on the formation and dynamics of dark solitons in a 2D Rb BEC. Solitons in a BEC can be of two types: bright (for attractive inter-particle interaction) and dark (for repulsive inter-particle interaction). A matter wave dark soliton formed in a BEC is a dip in atom density with a phase gradient across the dip. This phase across the dip determines the propagation speed of the solitons in the condensate. Stationary solitons are called dark solitons while moving solitons are called gray solitons. Within the framework of mean field approximation, we used a non-linear Schrödinger equation called Gross-Pitaevskii equation to numerically realise the formation of dark solitons in a 2D Rb BEC using various techniques such as phase imprinting and density engineering. In this part of our numerical study, we imprinted a smooth phase gradient (experimentally likely condition) and contrasted it with imprinting a sharp phase gradient (usually found in literature) onto the condensate. We studied the outcomes of these imprintings on the generation and instability dynamics of solitons and were able to highlight the effects of the imprinting on long-term vortex decay dynamics. We pointed out the rich dynamics exhibited by the vortex dipoles stemming from the unstable dark soliton and consolidated an alternate method to generate dark solitons in double well potential under periodic modulation of interactions. We also explored the formation of a transient soliton lattice and the existence of an intriguing phase wherein the Faraday pattern and soliton lattice were found to coexist under certain conditions.

It needs to be pointed out that the limitation of this study arose from the fact that we had access only to a 3D Rb condensate in our lab. Therefore, in the final phase of the current research, we investigated the limitations of experimentally realizing the above-mentioned numerical study of phase imprinting of a 2D Rb condensate. In the same vein, we studied the possibilities of modifying our experimental set-up to overcome this limitation.

We also conducted an experimental and numerical study to probe the linear regime of the condensate. To investigate the linear regime, bouncing dynamics of the 3D spherical Rb condensate from a Gaussian barrier were studied; this is popularly known as the ‘Quantum Bouncer’ problem. This part of the study resulted in the emergence of unusual fringe patterns in the condensate. We also looked at the possibility of transforming the fringe pattern into solitons, which was numerically confirmed by changing the interaction strength in the condensate.

Table 1: List of Symbols

μ_B	Bohr magenton
k_B	Boltzman constant
$\hbar$	Reduced Planck constant
a_s	S-wave scattering length
m	Mass of Rb atom
ξ	Healing length

List of Publications

1. **G. Verma**, U. D. Rapol, and R. Nath, "Generation of dark solitons and their instability dynamics in two-dimensional condensates", 2017, *Phys. Rev. A* **95**, 043618. Available from: https://link.aps.org/doi/10.1103/PhysRevA.95.043618
2. **G. Verma**, J. Mangaonkar, R. Nath and U. D. Rapol, "Bouncing dynamics of Bose-Einstein condensate from a Gaussian barrier". *Manuscript under preparation.*

Other Contributions

1. C. Vishwakarma, J. Mangaonkar, K. Patel, **G. Verma**, S. Sarkar and U. D. Rapol, “A simple atomic beam oven with a metal thermal break”, 2018, *Manuscript under review.* Available from: https://arxiv.org/abs/1810.09090
2. **G. Verma**, C. Vishwakarma, C. V. Dharmadhikari and U. D. Rapol, “A compact atomic beam based system for Doppler-free laser spectroscopy of strontium atoms”, 2017, *Rev. Sci. Instrum.* **88**, 033103. Available from: https://doi.org/10.1063/1.4977593 (G. V. and C. V. contributed equally to this work.)
3. S. Sarkar, S. Paul, C. Vishwakarma, S. Kumar, **G. Verma**, M. Sainath, U. D. Rapol and M. S. Santhanam, “Non-exponential decoherence and subdiffusion in atom-optics kicked rotor”, 2017, *Phys. Rev. Lett.* **118**, 174101. Available from: https://link.aps.org/doi/10.1103/PhysRevLett.118.174101
4. S. Kumar, S. Sarkar, **G. Verma**, C. Vishwakarma, Md. Noaman and U. Rapol, “Bose-Einstein condensation in an electro-pneumatically transformed quadrupole-Ioffe magnetic trap”, 2015, *New J. Phys.* **17**, 023062. Available from: http://stacks.iop.org/1367-2630/17/i=2/a=023062

Contents

List of Figures **xxi**

1 Introduction **1**

1.1 Dilute Weakly-Interacting Atomic Gases 4
  1.1.1 Experimental Realization of BEC 6
1.2 Experiments with Ultracold Quantum Gases - The state of the art . . . 7
1.3 Nonlinear Regime of the Condensate 9
  1.3.1 Solitons 10
  1.3.2 Vortices 13
1.4 Linear Regime of the Condensate 15
1.5 Dissertation Outline 16

2 BEC: Theoretical Background **19**

2.1 Introduction 19
2.2 Weakly Interacting Bose Gas 19
2.3 Mean Field Approach 20
2.4 Excitations of BEC 25
2.5 Dimensionless Gross-Pitaevskii Equations 26
  2.5.1 Scaling of GPE in the Absence of a Trap 26
  2.5.2 Scaling of GPE in the Presence of Trap 27
  2.5.3 Dimensionless GPE for Condensate in Lower Dimensions 28
2.6 Thomas-Fermi Approximation 30
2.7 Numerical Simulation: Imaginary Time Propagation Method 32
2.8 Dark Solitons and Snake Instability 33
2.9 Faraday Pattern in BEC 35

2.9.1 Faraday Instability 36

3 Dynamics of BEC: Non-Linear Regime 39

3.1 Introduction 39

3.1.1 Dark Solitons: Generation and Instability Dynamics 39

3.2 Snake Instability 41

3.3 Vortex Dynamics 47

3.4 Alternative Techniques for Soliton Generation 51

3.4.1 Gaussian Barrier and Time Dependent Interaction 51

3.4.2 Linear Variation of g in Time 51

3.4.3 g Periodic in Time 53

3.5 Experimental Realization 56

3.6 Summary 56

4 Dynamics of BEC: Linear Regime 59

4.1 Introduction 59

4.2 Experimental Setup: BEC Production 60

4.2.1 Experimental Sequence 62

4.2.2 Detection Scheme 66

4.3 Observation of BEC 68

4.4 Trap Frequencies 69

4.4.1 Numerical Modelling 70

4.4.2 Experimental Measurement 74

4.5 Bouncing BEC Experiment 78

4.5.1 Experimental Setup: Bouncing BEC 78

4.5.2 Experimental Results 80

4.5.3 Simulation Results 91

4.6 Summary 95

5 Summary and Conclusion 97

6 Future Outlook 99

6.1 Lower Dimensional Condensate and Previous Studies 99

6.2 2D Optical Dipole Trap 101

6.3 Double Well Potential 102

6.4 Modulation of Interaction or Barrier Strength 103
6.5 Detection 103
6.6 Summary 103

Bibliography **105**

List of Figures

3.1 **Dynamics of dark soliton:** The time evolution of the scaled condensate density $n(x, y, t) = |\psi(x, y, t)|^2$ of a rubidium BEC with $N = 10^5$ atoms , $a = 109\ a_0$ (where a_0 is the Bohr radius), $\omega_x = \omega_y = 2\pi \times 10$ Hz and $\omega_z = 2\pi \times 700$ Hz, with an initial phase: $\theta(x) = \pi/2$ for $x < 0$ and $\theta(x) = -\pi/2$ for $x \geq 0$. (a) The condensate density at $t = 22\ \mu$s shows the formation a nodal stripe which eventually transforms into a stationary DS. (b) The SI first develops at the center of the condensate. (c) A transient stripe of VDs emerge, and in (d) we show the VDs at the centre of the condensate. The phase and velocity fields corresponding to (d) are shown in (e) and (f) respectively. 42

3.2 **Width of dark soliton across the condensate:** (a) The TF density profile $\left(|\psi(x, y = 0)|^2\right)$ at $t = 0$ (dashed line) and the emerged solitons at $t = 6.75$ ms (solid line). (b) The numerical results (filled circles) for the width $l_s(y)$ of the stationary DS as a function of y is compared with that of LDA with a TF profile (filled squares). The BEC setup is same as that of the Fig. 3.1. 43

3.3 **The subsonic local velocity v_s along the x-axis of the dark soliton as a function of b at different locations along the y-axis**. For both curves, we calculated the velocity at $x = 1.5\ l_z$. At large values of b, v_s saturates to the speed of sound c, and also the center of the soliton moves faster compared to the edges. The setup is same as that in Fig. 3.1. 44

3.4 **The SI dynamics for different b is depicted through the condensate density:** (a) The SI develops first at the centre for $b = 0.05\ l_z$. (b) The SI develops both at the centre and the edges simultaneously for an intermediate value of $b = 0.2\ l_z$. (c) For sufficiently large values of $b = 0.75\ l_z$ the instability occurs first at the edges. In the later stage, the whole DS breaks up into vortex dipoles. Note that, larger the b shallower the soliton is, hence faster it propagates. The setup is same as that in Fig. 3.1. 45

3.5 **Vortex dynamics:** (a) Two lone vortices are approached by two vortex dipoles and in (b) when they reach close to each other. In (c), an exchange of vortices has been taken place and a new pair of vortex dipoles are created. The setup is same as that in Fig. 3.1 with an initially imprinted sharp phase gradient. The initial and final VDs are indicated by ellipses and direction of propagation of VDs are shown by arrows. 46

3.6 **Vortex dynamics:** (a) The collision of two counter-propagating VDs. (b) Upon collision they exchange vortices and form a new pair of VDs. The new pairs propagate opposite to each other in a direction perpendicular to the axis of collision, as shown in (c). The initial and final VDs are indicated by ellipses and direction of propagation of VDs are shown by arrows. 48

3.7 **Long term decay of vortices:** Plot shows the number of vortices as a function of time for two different b. Larger the value of b, faster the decay of vortices. The filled circles and squares are obtained by starting from a TF solution with an imprinted phase, whereas the empty circles and squares are for the cases in which time evolution starts with the dark solitons in a clean background (CB). The solid lines are calculated using the rate equation given in Eq. (3.2) with $\Gamma(0) = 0.053\ \mathrm{s}^{-1}$ and $\Gamma(0.74) = 0.22\ \mathrm{s}^{-1}$. The oscillations in the vortex decay curve is due to the transitions between vortexoniums to VDs and vice versa. The setup is same as that in Fig. 3.1. The origin of the time is taken at the point at which the DS completely breaks up into VDs, which is of the order of milli seconds. 50

3.8 **Generation of gray solitons in a double well potential under temporal variation of short range interactions:** (a) The density profiles $\tilde{n}(x, y = 0) = l_z^2|\psi(x, y = 0)|^2$ for the ground state (GS) (black solid line) and the emerged solitons for different ramp times, $\tau = 1/\alpha = 0.45$ ms (blue solid line) and $\tau = 3$ ms (red dashed line) are shown. All plots are renormalized with its corresponding maximum density and the snapshots are taken at different instants of time for different τ. (b) Relative soliton depth (filled circles) for the width $d = 1\ l_z$ and $d = 2\ l_z$ (filled squares) as a function τ is plotted. The soliton depths are calculated at the same location [$x = 46.5\ l_z$, shown with a box in (a)] in the condensate, shown by dashed vertical line in (a). The definition of $\Delta\tilde{n}$ is schematically shown in the inset of (b), which corresponds to the box in (a). The BEC setup is same as that of the Fig. 3.1, and for both (a) and (b) we take $\delta g = -g_{2D}/2$. 52

3.9 **Periodicity of DS lattice:** Plot shows the change in DS lattice periodicity as a function of modulation frequency, ω_m for $V_0 = 1\ \hbar\omega_z$ (squares) and for $V_0 = 3\ \hbar\omega_z$ (circles) with $\gamma = 0.2\ \omega_z$ and $b = 0.86\ l_z$. The two insets show the density snapshots for $V_0 = 3\ \hbar\omega_z$ at $\omega_m = 0.25$ and $\omega_m = 0.6\ \omega_z$. The dashed line shows, $1/k = 1/\epsilon^{-1}(\omega_m)$, the wavenumber corresponding to the Bogoliubov frequency ω_m. The BEC setup is same as that of the Fig. 3.1. 54

3.10 **Competition between Faraday pattern and DS lattice formation:** (a) Faraday patterns for $V_0 = 0$. (b) Co-existence of Faraday patterns and 2D DS lattice for $V_0 = 0.003\ \hbar\omega_z$. (c) Formation of pattern-free, transient DS lattice for $V_0 = 0.1\ \hbar\omega_z$. For all plots $\alpha = 0.2$ and $\omega_m = 0.6\ \omega_z$. The BEC setup is same as that of the Fig. 3.1. The extended time evolution of (b) and (c) are shown in Fig. 3.12. 54

3.11 **DS lattice lifetime:** Plot shows the lifetime of the lattice ($\tau_{lattice}$) as a function of V_0 for two different ω_m. The setup is same as that for the Fig. 3.10. The lifetime $\tau = \tau_2 - \tau_1$, where τ_1 is the time at which the lattice is stabilized to a time-independent periodicity, and τ_2 is the time at which the outer DSs are unstable. 56

3.12 **Instability dynamics of DS lattice:** (a) and (b) shows the extended time evolution of the state shown in Fig. 3.10 (b). The phase plots corresponding to (a) and (b) are shown in (e) and (f) respectively. (c) and (d) show the extended time evolution of the state shown in Fig. 3.10 (c), with corresponding phase plots in (g) and (h). (a) and (b) are for $V_0 = 0.003\ \hbar\omega_z$ whereas (c) and (d) are for $V_0 = 0.1\ \hbar\omega_z$. All other details of the setup are same as that of Fig. 3.10. 57

4.1 **Energy level diagram:** Plot shows D1 and D2 transiton of ^{87}Rb. Red dashed lines with arrows shows different transitions involved in cooling and imaging. Our experiment involves transitions between the hyperfine levels of D2 line only. Cooling and imaging of atoms happens on the cyclic transition $|F=2\rangle \longrightarrow |F^{'}=3\rangle$. Repumper beam uses $|F=1\rangle \longrightarrow |F^{'}=2\rangle$ transition to pump atoms back into $|F=2\rangle$ (upper hyperfine ground state). 61

4.2 **Experimental sequence:** Plot shows the ON and OFF time for different optical and magnetic fields. First, two of the three camera trigger pulses overlap with two probe laser pulses with a wait time of 200 ms between them which depicts the detection scheme. 64

4.3 **Time-of-flight absorption images showing the typical phase transition of the thermal atomic cloud to a BEC phase:** Images in panels (a), (b) and (c) shows the integrated optical density of the atoms and the plots below the images show the central 1D cross-section of the corresponding image along the horizontal direction. Solid red lines in 1D plots show fitting to the optical density distribution and dashed blue lines show the contribution from the thermal cloud in each of the images. These images are taken after a 14 ms time-of-flight. (a) Bimodal density distribution showing the onset of phase transition with $N \sim 1.85 \times 10^5$ atoms at a temperature about of 200 nK (final power in each dipole beams is kept $\sim$ 14 mW), (b) with $N \sim 1.3 \times 10^5$ atoms at temperature 130 nK (final power in the dipole beams $\sim$ 6.9 mW) showing the enhancement in the condensate fraction, (c) with $N \sim 7.2 \times 10^4$ atoms at temperature 51 nk, formation of almost pure condensate at final power in the dipole beams $\sim$ 3.6 mW. The field of view of the images is 0.2 mm × 0.2 mm. 65

4.4 **Magnification of the imaging system:** Plot shows the center position of an atomic cloud falling freely under gravity. Dashed black line shows the linear fit to data. From the slope of the straight line, magnification of our imaging system is estimated as 1.61 68

4.5 **Time evolution of the condensate aspect ratio:** Plot shows the aspect ratio of BEC to be $\sim$ 90% with $N = 7 \times 10^4$ atoms 70

4.6 **Orientation of optical dipole and barrier beam in the experimental setup:** (a) Schematic: Side view of experimental setup [1]. (b) Schematic showing orientation of red detuned dipole beam and the blue detuned barrier beam with respect to imaging axis (y-direction). 110 MHz beam makes an angle $\theta_1 \sim -25^\circ$ and 120 MHz beam makes an angle $\theta_2 \sim 30^\circ$. The optical barrier beam is oriented at $\theta_3 \sim 10^\circ$. 72

4.7 **Modelling of the total trapping potential:** (a) Cross sections along x, y, z direction of the numerically simulated trapping potential (U_{Total}) across the trap minima at $P = 3.6$ mW. (b) Shows the second order polynomial fit (solid black lines) to the cross sections near the trap minima. from the fit, trap frequencies are extimated to be $\nu_{\mathrm{x}} = 116$ Hz , ν_{y} = 99 Hz , $\nu_{\mathrm{z}} = 83$ Hz 74

4.8 **Trap frequency measurement using parametric heating method:** (a), (b), (c) shows parametric resonances at different end power of the dipole trap where solid and dashed red line represents the first (2ν) and second (ν) harmonic of the trap frequency respectively while black and red color of line shows non degenerate frequencies of the trap. (a) Resonances at P $\sim$ 3.6 mW power in dipole beam, (b) P $\sim$ 7.2 mW, (c) P $\sim$ 14.4 mW. All Resonances are found to be in agreement with $\nu \propto \sqrt{P}$ scaling. (d) shows the time evolution of Thomas-Fermi radius of condensate. The solid line shows the fitted profile. Trap frequency from the fit found to be $\nu_x \sim 62$ Hz and $\nu_y \sim$76 Hz. 76

4.9 **Optical layout for barrier beam preparation** 79

4.10 **Image showing the setup to generate optical barrier:** (a) Beam prepared on a separate optical table using a tunable DLpro laser diode. The output of this laser diode is split into two beams. one of the beams is transported to the main optical table and another beam is sent to wavemeter for monitoring the wavelength of the beam. (b) Shows the assembly of fiber coupler and three lenses, mounted on 3D stage to align the beam with respect to atomic cloud 79

4.11 **Bouncing dynamics of BEC from a Gaussian barrier:** Left panel: shows absorption images of free fall evolution of BEC in the presence of optical barrier with 12.5 mW of optical power, beam waist, $w_{\text{barrier}} \sim 30\ \mu$m at frequency, $\omega_{\text{barrier}} = 384.76553$ THz. Barrier beam is placed $\sim 100\ \mu$m below the in-trap condensate position. Right panel: shows 1D vertical cross-section of the center of the condensate. (a) Shows the initial condensate after a TOF of 0.21 ms (b) Shows the first hit at the barrier after a TOF of 4.61 ms (c) Shows the squeezing of the condensate along the vertical direction where it interacts with the barrier for about 0.6 ms before reverting 82

4.12 **Free fall evolution of BEC in the presence of barrier continues:** (d) Condensate moving upward, starts to develop double peak structure along the z axis (e) Double peak feature enhances (f) Wave packet continues to squeeze along the vertical direction and optical density of the condensate decreases due to quick expansion along the x direction . . . 83

4.13 **Further free fall evolution of BEC in the presence of barrier:** (g) Splitting of the condensate along vertical direction becomes prominent (h) Condensate reaches the initial height and after this point, it starts to come downwards again where the vertical split of the condensate starts to merge (i) Splitting feature has disappeared 84

4.14 **Continuation of free fall evolution of BEC in the presence of the barrier:** (j) Second hit of the condensate at the barrier. The extent of the condensate along horizontal direction becomes much larger than the barrier (k) Central part of the condensate interacts with the barrier and reflected back while rest of the condensate continues to fall downwards 85

4.15 **Evolution of the secondary reflection from barrier continues:** (l) Interference fringes starts to appear at the corners of outer arms of the condensate (m) A deformation of barrier beam profile has lead to the formation of the fringes in the top reflected part (n) Contrast of the fringe pattern enhances. Misalignment of the barrier ($\sim 10\ \mu$m) with respect to centre of the condensate causes an overall tilt with respect to the vertical axis (asymmetry) in the reflection which causes fringes to appear only on one side of the arm 86

4.16 **Bouncing dynamics of BEC from a Gaussian barrier:** Left Panel: Absorption images of freely falling BEC in the presence of barrier placed $\sim 130\ \mu$m below the trap center. Power and detuning of the barrier beam kept unaltered. Right panel: shows the corresponding 1D vertical cross section of the images through the center of cloud (a) Condensate after a TOF of 0.21 ms (b) First hit at the barrier, wave packet shrinks along the vertical direction and subsequent increment in the OD is observed (c) Reflected wave packet starts to develop splitting feature 87

4.17 **Continuation of the evolution of the condensate after the first hit at barrier:** (d) Splitting feature along vertical direction enhances (e) Wave packet reaches the maximum altitude and continues to squeeze along the vertical direction (f) Condensate starts to revert and splitting feature starts to disappear 88

4.18 **Absorption images of the falling condensate during second hit on the barrier:** (g) Extent of the cloud becomes larger than the barrier size during the second hit therefore, the only central part is reflected back (h) Shows the emergence of fringe pattern in the falling side arm of the condensate. Asymmetric reflection makes the fringes appear only at the right side of the condensate arc 89

4.19 **Absorption images of the reflected condensate for two different barrier strength:** Images taken after a TOF of 12.01 ms. Barrier is placed 100 μm below the condensate. (a) Reflection for barrier beam power, P = 12.5 mW (b) Reflection for barrier beam power, P = 7.4 mW. Arc length of the reflected condensate is found to be more in case of weaker barrier. Also, the curvature of the arc is larger for weaker barrier 89

4.20 **Illustration showing the reflection of the atoms from a Gaussian barrier:** For reduced barrier power, atoms can penetrate deep into the barrier resulting in longer reflected arc compared to a strong barrier. Also, the curvature of the reflected arc will be larger in case of a weak barrier 90

4.21 **Numerical solution of effective 2D GP equation:** Barrier is placed 60 μm below the condensate with barrier beam power, P = 11.5 mW. (a) A color plot shows the secondary reflection of the condensate at TOF of 11.8 ms. (b) Shows the zoom in area of the same plot where the formation of the fringe pattern similar to what we observed in the experiment can be seen. The plot shows the scaled density of the cloud. 94

4.22 **Numerical simulation:** Comparison of reflected condensate for two different barrier strength at TOF of 7.73 ms. Barrier is placed 60 μm below the condensate. (a) Power in the barrier beam P = 10.3 mW (b) Power in the barrier beam P = 5.6 mW. In agreement with the experimental observation, length and curvature of the reflected arc is found to be more in case of weaker barrier 95

GLOSSARY

Chapter 1

Introduction

Bose-Einstein Condensate (BEC), a macroscopic quantum state of matter was first predicted in 1924 [2] and experimentally realized in 1995 [3–5]. Bose-Einstein Condensate continues to amaze scientists around the world with its unique properties and intriguing nature. As opposed to the classical world where things are governed by laws of classical physics, BEC provides a platform to the surprising and not-so-intuitive quantum world. Roots of the much-developed understanding of quantum world go back to some of the ground-breaking experiments starting from the observation of black-body spectrum and its explanation [6] followed by the discovery of photoelectric effect [7] which was explained by Einstein in 1905 using Planck's quantum hypothesis, during which he introduced the concept of wave-particle duality for light [8]. In 1924, de Broglie extended this theory to postulate the wave-particle duality for matter [9]. In 1925 Einstein predicted a new state of matter, which was later called as a Bose-Einstein Condensate (BEC) using the photon statistics developed by Satyendra Nath Bose [10]. Bose developed the theory of statistical mechanics of photons and re-derived the Planck's law of blackbody radiation by treating photons as a bunch of identical particles. Einstein generalised his theory to an ideal gas of non-interacting massive bosons and derived the Bose-Einstein distribution, $f(\epsilon_\mathrm{i})$, which described the statistical distribution of bosons over single particle energy states,

$$f(\epsilon_\mathrm{i}) = \frac{1}{e^{(\epsilon_\mathrm{i} - \mu/k_\mathrm{B}T)} - 1} \tag{1.1}$$

where ϵ_i is the energy of level i, μ is the chemical potential and T is the temperature of the gas. Quantum mechanics dictates that particles can be broadly classified into two different types viz. Fermions and Bosons. Fermions (such as electrons) have half-integer spin and follow Fermi-Dirac statistics while obeying the Pauli exclusion principle whereas bosons (such as photons) have integer spin and follow the Bose-Einstein statistics and unlike fermions, any number of particles are allowed to occupy the same quantum state. Thus, in the case of bosons, at extremely low temperatures ($T \to 0$), there is a macroscopic occupation of the ground state, which is referred to as a Bose-Einstein condensation.

For an ideal gas of non-interacting bosons (particles with zero or integer spin) in thermal equilibrium at temperature T, the spatial extent of each particle is associated with its thermal de Broglie wavelength, conventionally defined as

$$\lambda_{\mathrm{db}} = \sqrt{\frac{2\pi\hbar^2}{mk_{\mathrm{B}}T}} \tag{1.2}$$

where m is the mass of the particle. At high temperature, the thermal de Broglie wavelength of each particle is small compared to the average interatomic particle distance. Thus, the dynamics of the gas is governed by particle-like behaviour following the classical Boltzmann distribution. The de Broglie wavelength associated with the particles increases as the temperature of the gas is lowered. Below a critical temperature T_λ, the wavelength corresponding to each particle becomes larger than the interparticle separation which leads to the suppression of individual identity of particles and enhancement in their collective behaviour. At this point, a significant fraction of particles occupies the lowest single-particle quantum state while a small fraction of remaining atoms gets distributed over the excited states [11]. This allows the gas to emerge as a giant single coherent entity called Bose-Einstein condensate. Bose-Einstein condensation for an ideal gas of N atoms (non-interacting) with uniform density in volume V occurs when the phase space density, $\rho = n\lambda_{\mathrm{db}}^3$ becomes larger than 2.612, where $n = N/V$ is the number density of atoms and λ_{db} is the thermal de Broglie wavelength. The fraction of atoms condensed in the ground state is given by

$$\frac{N_0}{N} = 1 - (T/T_\lambda)^{3/2} \tag{1.3}$$

where N_0 is the number of atoms in ground state and corresponding critical temperature is given by

$$T_\lambda = \frac{2\pi\hbar^2}{mk_{\mathrm{B}}} \left(\frac{\rho}{2.612}\right)^{2/3} \tag{1.4}$$

Initial concepts related to BEC and quantum gases were first explored in the context of liquid ^{4}He. Below a critical temperature of 2.17 K helium undergoes a phase transition [12, 13] becoming a superfluid (fluid with zero viscosity which is capable of supporting quantized vortices). This superfluid phase is identified as He II. In 1938, London [14, 15] interpreted the properties of this phase as a manifestation of Bose-Einstein condensation of helium atoms. At first, this idea was not widely accepted as the strong interactions present among the helium atoms was far away from the Einstein's description of BEC of non-interacting gas of bosons. Later, Landau [16] gave the first successful description of He II hydrodynamics with two fluid model wherein a mixture of superfluid fraction and a normal viscous fluid fraction co-existed with the fraction depending on the temperature. Above the critical temperature the entire fluid is identified with the normal fluid, and as the temperature is lowered, the proportion of normal fluid reduces while the volume of superfluid increases. It was also shown by Landau that a dispersion relation which is linear at low momenta accounts for the superfluid behaviour of helium at low temperatures. Later Bogoliubov [17] showed that precisely similar dispersion law is supported by a weakly-interacting Bose gas which indicated that Bose-Einstein condensation was indeed the fundamental mechanism behind superfluidity of liquid helium. Although Bose-Einstein condensation is now known to be the driving force behind helium II superfluidity, less than 10 % of helium atoms undergo condensation due to the inherent strong interactions present in the liquid helium.

The concept of BEC has been used in a broader context over the years covering diverse topics such as condensation of Kaons in neutron stars [18], cosmogenesis and exotic superconductivity [19]. Independent of the condensation process, ^{4}He exists as bosonic gas. The fermionic neutrons, protons, and electrons in a ^{4}He atom bind to form a composite boson at energies much higher than the superfluid transition temperature. However, in a broad range of physical systems, the binding of the fermions to form composite bosons and the condensation of those bosons into a macroscopically occupied state occurs together which is the well-known BCS (Bardeen-Cooper-Schrieffer) mechanism. BCS theory is best known for providing the microscopic physical mechanism of superconductivity [20, 21]. The Bose-condensed "cooper pairs (a pair of electrons bound together)” in BCS theory occurs not only in superfluid fermionic ^{3}He isotope [22] but are relevant also to the dynamics of large nuclei [23] and the neutron stars.

1.1 Dilute Weakly-Interacting Atomic Gases

Although Einstein predicted the phenomena for a non-interacting ideal gas, experimentally realized BEC are resultant of weakly interacting and dilute gases. Since 1995, BEC of many different species have been realized such as BEC of alkali atoms where short-range and isotropic contact interaction are dominant (^{87}Rb [3], ^{85}Rb [24], ^{23}Na [4], ^{7}Li [5],^{41}K [25], ^{133}Cs [26]), BEC of alkaline atoms (^{40}ca [27], ^{84}Sr [28, 29], ^{86}Sr [30],^{88}Sr [31]), BEC of spin-polarized H atoms [32], BEC of metastable ^{4}He (in the lowest triplet state) [33], BEC of rare earth metal where long range and aniosotropic dipole-dipole interactions are dominant (^{52}Cr [34], ^{168}Er [35],^{174}Yb [36],^{164}Dy [37], where Dy has the largest magnetic moment), BEC of quasi-equilibrium magnons (elementary particle of a spin-wave) [38], BEC of excitons (a bound state of electron-hole pair in a semiconductor, transports energy without transporting the net electric charge) [39], BEC of exciton-polaritons (quasi-particles arises from the strong coupling of photons with excitons in the material) [40, 41] and BEC of mixtures of different species (^{41}K - ^{87}Rb [42],^{87}Rb - ^{133}Cs [43],^{6}Li - ^{7}Li [44]) and this list continues to grow.

Each species with their unique atomic properties and range of interactions expands the horizon to observe rich and fascinating phenomena. Einstein’s ideal gas predictions provide a good estimate of critical temperature for these gases as these gases are dilute enough ($\sim 10^{12} - 10^{13}$ atoms/cm^{3}) and exists at ultra-low temperatures ($\sim 10^{-6} - 10^{-9}$ K). In dilute gases, elastic binary collisions dominate over three body collision avoiding the transition of gas to liquid or solid phases. These binary collisions or interactions in ultracold gases are characterised by the s-wave scattering length, a_{s}. This parameter a_{s} emerges from the physics of two-body, low energy scattering of particles. At such low temperatures, scattering due to contribution from the s-wave dominates over higher energy p-wave and d-wave terms [45] in the partial waves. The s-wave scattering cross-section is related to s-wave scattering length through $\sigma = 4\pi {a_{\mathrm{s}}}^{2}$. A positive a_{s} indicates repulsive interactions between the atoms and can be thought of as a measure of the effective geometric radius of repelling atoms. For a gas to be called as weakly interacting and dilute, the density of the gas along with the scattering length should satisfy the condition that $n^{1/3}a_\mathrm{s} \ll 1$, in other words, a_s should be much smaller than the average inter-atomic distance. This allows 99% atoms to go to the BEC regime unlike the case of liquid He where only 10% atoms are converted into superfluid helium due to strong interactions. BEC produced out of these ultracold dilute gases delivers the purest form of BEC which can be well controlled and manipulated in the lab. There are also scenarios where BEC with negative scattering length can also be produced under certain conditions [5].

It is important to note that for an ideal Bose gas (non-interacting gas) with no external trap, BEC can only form in 3D systems. Density of states $\rho(E)$ can be used to understand this fact. For a uniform non-interacting gas, $\rho(E) \propto E^{\frac{(d-2)}{2}}$, where d is the dimensionality of the space. For a 3D gas, the number of excited states close to ground state goes to zero since $\lim_{E\to 0}\rho(E) = 0$, as a result, the thermal fluctuations do not destroy the condensate. In contrast to this, in 1D and 2D systems, thermal population diverges in the thermodynamic limit resulting in the absence of BEC. However, the presence of an external harmonic trap modifies the density of states of the ideal gas, $\rho(E) \propto E^{(d-1)}$ which allows the formation of BEC in 2D and forbidding the condensation in 1D even in the presence of an external trap.

For a weakly interacting dilute gas in an external trap (as in the case of most of the experimental setups), this picture changes. The trap geometries often used in experiments are spherical (3D), pancake (2D) and cigar shaped (1D). Condensate with the repulsive interaction between the atoms ($a > 0$) is stable in all dimensions for any given number of particles and confined in any trap configuration. Uniform condensates with attractive interactions (without any external trap) are stable only in 1D and become unstable against local collapse in 2D and 3D. However, a trap can provide stability to condensate with attractive interactions in two and three-dimensions, provided that the condensate contains lower than a critical number of atoms [46–49]. The condensate undergoes a global collapse above the critical number.

Since a uniform 1D condensate (with no trap and attractive interactions) is stable, the stability of such a system is studied by preparing the BEC in a quasi 1D or cigar-shaped trap and then releasing from the trap [50, 51].

Short-range interactions or the scattering length a_s in the condensate can be tuned using magnetic field induced or optical field induced Feshbach resonances [52]. Excellent control over tuning of scattering length has been achieved using these techniques. The strength of the interaction in the condensate can be changed spatially (over a length scale of $\sim$ 100 nm) and temporally [53]. With such control over the level of purity (no impurities), interactions and manipulation, a condensate becomes an ideal test bed for the observation of quantum effects at a macroscopic scale.

1.1.1 Experimental Realization of BEC

Realization of true atomic BEC at temperatures $\sim$ 100 nK became possible only after the advancement of laser cooling [54–56] and evaporative cooling [57] techniques for neutral atoms. Laser cooling techniques relied on dissipative optical forces exerted on atoms by laser radiation and evaporative technique relied on the removal of higher energy atoms from the trap resulting in re-thermalisation of the atoms to lower temperatures and higher phase space densities. The research groups of Carl Wieman and Eric Cornell at the University of Colorado and the group of Wolfgang Ketterle at MIT were the first to experimentally realize the Bose-Einstein condensation of rubidium and sodium atoms respectively in 1995 which led to a Physics Nobel prize award for Wieman, Cornell, and Ketterle in 2001 [58, 59].

Original attempts were made to condense spin polarised hydrogen atoms, which was finally achieved after overcoming a lot of challenges [32, 60, 61]. The creation of a condensate generally begins by the accumulation of $\sim 10^9$ atoms in a Magneto-Optical Trap (MOT), which are initially slowed by a Zeeman slower [62] (Zeeman slower reduces the velocity of the incoming atoms from few hundred meters per second to few tens of meters per second using a spatially varying magnetic field and a laser beam propagating opposite to the direction of atom flow) or using a 2D MOT [63] or directly from a low background vapor pressure [64]. These slowed atoms are loaded in a 3D MOT (formed by laser beams and magnetic fields) where atoms are further cooled up to $\sim 1\ \mu$K. Later, evaporative cooling is employed to reduce further the temperature of the gas to the nK regime and to increase the Phase Space Density (PSD) where confining trap is modified carefully to let higher energy atoms escape from the system while the lower energy atoms thermalize to a reduced temperature. This last step results in a very narrow velocity distribution of atoms marking a macroscopic occupation of the ground state and hence the formation of BEC.

1.2 Experiments with Ultracold Quantum Gases - The state of the art

The first generation of experiments with ultracold quantum gases were focused on understanding the various properties of BECs (coherence and superfluidity etc.) which included ground-breaking experiments like on demonstration of matter wave interference [65], four-wave mixing [66], quantized vortices [67], Bogoliubov excitations [68], long phase coherence [69], atom laser [70], extremely slow propagation of light in BEC [71], propagation of nonlinear excitations (solitons) in condensate [72], observation of dispersive shock waves [73] and Hanbury Brown Twiss Effect [74], Demonstration of the storage of light energy into matter and back into light showing how optical information could be stored on a BEC [75] and realization of low dimensional (1D, 2D) condensate [76, 77]. Besides, efforts were underway in the creation process of the BEC in more efficient, robust and simple ways by improving upon the experimental design of cooling and trapping. In parallel, researchers started exploring realization of degenerate Fermi gases [78, 79] to get an insight into the behaviour of electrons in solids.

Later, the interest in community shifted from understanding the properties of degenerate gases to experiments that could use the unique properties of condensates. One of the areas that came into light in this context was to study quantum gases in periodic optical lattices. An optical lattice is a periodic intensity pattern formed by a combination of standing waves of monochromatic light. Atoms can be trapped at intensity minima or maxima in the lattice depending on the detuning of the lattice laser wavelength with respect to the electronic transition of an atom. It is possible to make 1D, 2D and 3D periodic lattice using light beams which can resemble the crystal structure of a material. Atoms in such lattices mimic in many ways the electrons moving in the periodic coulomb potential of a solid state crystal. Over conventional solids, optical lattice provides the freedom to tune the depth and periodicity of the potential by changing the intensity and wavelength of the laser beams. It also allows the dynamic control over the lattice parameter to transform it into moving lattice [80, 81]. Implementation of Bose-Hubbard Model [82] and observation of superfluid to Mott-insulator transition [83] in an optical lattice were the first steps towards the realization of model Hamiltonians of condensed matter systems. This shift was fueled by a simple and profound idea [84] that quantum mechanical systems and models should be simulated on a quantum system which is controllable and mimics the original system. In general, classical computers have limitations in performing this task, while ultracold gases offer the opportunity to implement this idea. Ultracold gases allow for preparing highly controllable single-particle states, strongly correlated quantum systems (Tonks-Girardeau gas) [76, 85] and interacting many-body systems [81, 86, 87].

In the recent past, efforts are going on in exploring the phenomena of spin-orbit coupling [88] and topological phases, to investigate resemblance of classical nonlinear systems (presence of solitons, patterns, vortices), to search for new phases of matter such as quantum time-crystal [89, 90], Supersolids, to understand the dynamics of out-of-equilibrium quantum systems and to achieve quantum information processing in the pure and highly controllable cold atom systems. Besides this, attempts are being made to improve the precision of Atom Interferometers [91] and Atomic Clocks. Atomic clock plays a vital role in supporting broadband communication networks, and navigation with global positioning systems (GPS) while atom interferometers find a broad range of applications in both applied and fundamental physics. To name a few, atom interferometers are used in earth gravity gradient and curvature measurements [92], development of navigation sensors, the precise estimation of Newtonian gravitational constant G [93], the fine structure constant α [94], detection of quantum gravity effects [95] and gravitational waves [96, 97].

Beyond single species BEC, a realization of more complex systems like dual species BECs (Bose-Bose, Bose-Fermi mixtures, Fermi-Fermi mixtures), spinor condensates [98], Dipolar BEC with anisotropic long-range interactions is also of current interest in the community. This allows to study the ultracold chemistry, exotic quantum phases (Supersolid [99], quantum liquid crystal [100] phases), transport phenomena and impurity physics [101, 102], to simulate core properties of general relativity and to test quantum gravity effects where already it has been shown that density waves propagation in BEC forms an analogue gravity system [103, 104]. The field of ultracold quantum gases has been moving ahead with a lateral advancement on the technological front which made the production of dilute BEC a routine along with the improvement in the detection techniques to realize measurements with single-atom resolution [105–107].

Above, I have tried to provide a general account of some of the leading interests of the cold atom physics community, however, by no means is this an attempt to make a complete list of all fascinating experiments that have been conducted within this field.

BEC being a macroscopic quantum system has paved the way not only to test the theories in fundamental physics but also on technological advancements and quantum technologies. Overview of this vibrant field can be found in Ref. [45, 108–110].

1.3 Nonlinear Regime of the Condensate

Atom-atom interactions present in the condensate gives rise to nonlinearity in the system, and nonlinear systems are the doors to the most amazing phenomena in science. Nonlinearity present in any classical or quantum system leads to the formation and evolution of complex patterns and localized structures, e.g. Faraday pattern, solitons and vortices. Theoretical work has proved to be of great importance regarding realising the dynamics and exciting phenomena of BEC, where an effective mean-field theory is developed leading to the Gross-Pitaevskii equation (GPE) [108] given as

$$i\hbar\frac{\partial}{\partial t}\psi(r,t) = \left[-\frac{\hbar^2}{2m}\nabla^2 + V(r) + gN|\psi(r,t)|^2\right]\psi(r,t) \tag{1.5}$$

GPE governs the evolution of wave function $\psi(r,t) = \sqrt{n(r,t)}\exp[-i\phi(r,t)]$ which parametrises the condensate in a given external trapping potential $V(r)$, and in the presence of interactions g, in the system. Here $n(r,t)$ is the density of the condensate, $\phi(r,t)$ is the phase of the condensate and $g = \frac{4\pi\hbar^2 a_{\mathrm{s}}}{m}$ represent the strength of short-range interactions present in a 3D system which are solely characterized by scattering length a_{s}. External trapping potential in the GPE represents the potential which confines the atoms in experiments which in general is a harmonic trap. These traps are conservative and usually formed with magnetic [111] or optical fields. Optical traps (optical dipole trap [112] or optical lattices [113]) are preferred over magnetic traps due to less complexity involved in implementing these traps and possibility of implementing flexible trap geometries (highly anisotropic, dynamics and multi-well traps). GPE is valid only in dilute gas limit such that scattering length is much smaller than the average separation between the atoms. This equation is a variant of nonlinear Schrödinger equation and used in many other areas of physics including nonlinear optics [114, 115], plasma physics [116], astrophysics.

Modelling the BEC using a full many-body Schrödinger equation is difficult, and can be avoided by using the GPE which allows capturing the statics and dynamics of a BEC over a range of experimental parameters [117, 118]. GPE is not restricted to conservative systems but also a variant of this equation such as complex Ginzburg-Landau equation [119] is used to model dissipative systems and extensively used in the context of pattern formation [120]. GPE not only allows to understand the behaviour of condensate probed in experiments but also used as a tool to look for the interesting nonlinear effect such as solitons and vortices. When interaction in the system becomes negligible ($g \sim 0$), GPE reduces to regular Schrödinger equation representing a single particle.

1.3.1 Solitons

As mentioned above, solitons are a signature of nonlinearity present in the system, and atom-atom interaction in case of BEC makes it a nonlinear system. Solitons are spatially localized structures or waves which arise due to the balance of dispersion and nonlinearity in a system. These structures maintain their shape during propagation, and are remarkably stable against any perturbations or mutual collision and show particle-like properties. Historically, the first signature of soliton was observed in 1845 by John Scott Russel in a water channel [121], and he called them 'waves of translation'. Initially, solitons were just purely a mathematical concept until experimental verification came and these structures were found in various domains of physics. In 1965, Zabusky and Kruskal introduced the term "Soliton" for the first time [122] while studying the solution of the Korteweg-de Vries equation. A rigorous mathematical theory was later developed [123] which allowed the construction of a general solution to a certain class of equations regarding soliton to describe the modes of nonlinear partial differential equations which happened to be integrable using the inverse scattering technique [124]. In physics, other types of localized solutions are also named as "solitons", however, mathematicians strictly use the term to describe the nonlinear modes of the integrable nonlinear differential equation.

In the 1990s, the limitation of the theory was understood when the solitary waves were found to exist in a variety of systems, though they did not behave exactly as the classical theory. Particularly, a case of soliton-like pulse propagation in an optical fiber which satisfies the equation that has a solution in the form of solitons but it does not allow the integrability of the system due to the inclusion of additional terms. The additional terms added in such equations may describe physical effects of conservative or non-conservative nature which can modify the properties of the solitons still leaving them as localized solutions of the system. Thus the theory was extended to cover localized solution in conservative and non-conservative systems. Although localized solutions of these systems appear in physical systems and describe a specific class of phenomena. However, these solutions could not be used in a superposition to construct a general solution of the system. These are generally referred as solitary pulse or waves in case of conservative systems and dissipative solitons in case of nonconservative system (where gain and loss of energy/matter is taken into account). Now it is mostly accepted in the scientific community that although the properties of these structures are peculiar, interestingly 'Solitons are everywhere'.

Solitons, in general, underlie the understanding of tidal bores, cyclones, massive ocean waves like tsunamis, signal conduction in neurons and biomembranes [125], collective motion in proteins and DNA [126], and natural phenomena such as "Morning Glory" (hundreds of kilometers cloud waves) [127]. To note, these are a class of dissipative soliton or solitons in dissipative systems which are far from equilibrium where a major balance occurs between gain and loss of matter or energy [128]. Solitons have been actively studied in many different domains including in mathematics and physics (such as in the context of the solution of the Korteweg-de Vries equation, in shallow water, in magnetic thin films and optical fibers etc) [129, 130]. Solitons have given a massive push to today's telecommunications industry due to the ability of optical pulses to propagate as solitons for vast distances without significant loss or dispersion. Their appearance in BEC is unique and valuable in itself. A Bose-Einstein Condensate (BEC) of dilute atomic vapor not only provides a clean and well-controlled environment to study these structures and link a macroscopic quantum system with other domains but also opens an avenue into looking at the interface between quantum and the classical systems.

In the case of condensate, solitons are stable and robust and found to exist with long lifetimes [131] in 1D. In higher dimension, solitons either collide inelastically or become unstable to decay into more stable structures [132–134]. There are mainly two kinds of solitons, bright [135] (supported by condensate with attractive atom-atom interactions or called focusing nonlinearity) and dark [136] (supported by condensate with repulsive atom-atom interactions also called defocussing nonlinearity). Bright solitons can be easily pictured by a hump or localised peak in the condensate density. These are self-bound matter waves and occur as a density peak on zero background density. Stable bright solitons occur only in 1D condensate and are unstable in higher dimensions. Bright solitons were first observed in lithium condensate confined in quasi 1D magnetic trap [50, 51].

In a uniform condensate, a bright soliton solution [142] can be represented as

$$\psi(z,t) = \psi_0 \operatorname{sech}\left(\frac{z-vt}{\xi}\right) \exp\left[i\left(kz-\omega t\right)\right] \tag{1.6}$$

where $n_0 = |\psi_0|^2$ is the peak density, ξ provides the spatial width of the soliton, k is the soliton wavenumber and, ω is the frequency which is related to the v is the velocity of soliton.

Bright solitons have been observed in plasma physics [116, 137], acoustics [138], optical physics [139, 140], fluids and biological systems etc. In contrast to Bright Solitons, Dark Solitons (DS) are less explored. DS is a nonlinear wave characterised by a density dip and phase gradient across it. The depth of solitons or the phase across the dip determines the propagation velocity of the soliton in the condensate [141, 142]. In 1D uniform condensate, the DS solution [142] can be written as

$$\psi(z,t) = \psi_0 \left[\frac{iv}{c} + \sqrt{1-\frac{v^2}{c^2}}\tanh\left(\frac{z-vt}{\xi}\sqrt{1-\frac{v^2}{c^2}}\right)\right] \tag{1.7}$$

where $n_0 = |\psi_0|^2$ is the homogenous background density of the condensate, ξ provides the spatial width of the soliton and c is the sound speed in the condensate. If the condensate density at the dip becomes zero, then the corresponding velocity of the solitons is zero or they are called stationary solitons while solitons with non zero density at the dip, acquires velocity and are called as gray solitons. The phase and velocity of a soliton are interrelated to each other. The finite sharp phase difference, δ across the soliton dip satisfies the following equation

$$v = c\cos\left(\frac{\delta}{2}\right) \tag{1.8}$$

Dark solitons in 2D and 3D are dynamically unstable and decay into a chain of vortices through snake instability. A detailed description of the GPE and dark solitons will be provided in chapter 2. Besides vast literature on theoretical studies of dark solitons, there exist many experimental results on dark solitons including observation of dark solitons in optical fibers [143, 144] and waveguides [145], in parametrically driven shallow liquids [146], discrete mechanical systems [147], magnetic thin films [148], dissipative solitons in a complex plasma [149] and in water wave tanks [150, 151].

In the context of BEC, theoretical studies on dark soliton started in 1971 [152] where the exact solutions of the GPE were found and connected to the solitons of Korteweg-de Vries (KdV) equation (which is used to describe the dynamics of shallow water waves) in the small amplitude limit. Dark solitons have been explored in the context of its formation, interaction, collisions and dynamics in the presence of perturbation. Dark solitons were first realized in condensate [72, 153] by phase imprinting method. These structures are found to be unstable in higher dimensional condensate and decay into vortex rings and chain of vortex dipoles [154] due to their instability to transverse excitations. We will review the various method of dark soliton generation and its properties in detail in chapter 2.

Interest in studying Dark solitons in the condensate is due to several reasons. One of them is that these structures are nonlinear analogues of excited states of a “prototype” quantum harmonic oscillator which is the case of a BEC confined in harmonic trap [155]. On the other side, due to a phase jump at their density minima, these structures provide a “degenerate” one dimensional (1D) analogue of vortices that are found in diverse branches of physics and subject of great importance [156]. Besides this, matter wave dark solitons are similar to vortices and quite fundamental structures which arise spontaneously during the BEC phase transition [157, 158], and can provide a tool to probe the rich physics of purely quantum systems at the mesoscale [159]. Although the above reasons are in the context of fundamental physics, on the application front, these structures can be used to monitor the phase acquired in atomic matter wave interferometer in the non-linear regime [160] and also can be used as qubits [161] for quantum information processing. Recently efforts are being taken to study the collective aspect of so-called quantum gases and to use dark solitons to probe many-body physics.

1.3.2 Vortices

Vortices in BEC are topological non-linear excitations supported by GPE [162] and differ significantly in their size and origin from the vortices in classical fluids. Vortices in the condensate/superfluids are features identified by a localised dip in the density with a phase singularity in its centre. Around the vortex in a closed path, the phase undergoes a $2\pi n$ winding, where n is an integer which denotes the circulation or charge on the vortices. Phase singularity results in a velocity field that makes the fluid to circulate around the vortex core. A standard method to generate vortices is through the rotation of superfluid [163]. In case of liquid helium the rotations are induced by rotating the container or vessel carrying the fluid and in case of the atomic BEC's stirring is done using laser beams [67] or through the rotation of the full magnetic trap [164]. During rotation of the fluid, vortices start to nucleate by lowering the energy of the system, and when fluid is rotated above a critical speed, it forms a lattice at the centre of rotation [118, 165]. Formation of vortices can also result from symmetry breaking after a fast quench across the BEC phase transition known as Kibble-Zurek mechanism [166, 167]. This mechanism allows the creation of small pockets of phase coherence in the condensate instead of a uniform phase where these pockets grow and form the boundaries and discontinuities creating the vortex lines. Other than the rotation of the cloud [168] there exist many different methods to produce vortices such as dynamical phase imprinting of the topological defect [169, 170], stirring with the help of a localized laser beam [165, 171], rotation of trap, interference method, through decay of soliton [73, 154] and density engineering of the condensate [169, 172]. To study the dynamics of vortices, BEC offers an advantage over superfluid He as the structure of individual vortex can be resolved much comfortably due to large vortex core through imaging techniques.

Vortices generated in classical fluids might look similar to quantum vortices but there are some subtle differences. One of them being that the classical vortices can be created with any degree of fluid rotation which characterises the continues change of circulation of the fluid. However quantum vortices circulation is quantised and restricted to occur in an integer multiple of the quantum circulation identify by a phase gradient of $2\pi n$ across the vortex core.

Vortices in quantum fluid has been realised experimentally in various configurations and trap geometries such as vortex lines [73], vortex rings [154], tangles [173], lattices [174], quasi-2D turbulence [175], vortex dipoles [176], giant vortices [177] and multiply charged vortices [178]. In experiments to probe vortex core which typically has a size smaller than the imaging resolution is observed by releasing the condensate from the trap where condensate expands before imaging [175, 179]. Nowadays imaging techniques have evolved including real-time and non-destructive imaging of the condensate [180, 181] which makes condensates to be an attractive medium for exploring the quantum behaviour.

All these efforts led to the mapping of interesting phenomena related to vortices, pattern formation and instabilities from fluids to BEC such as realization of Bénard-von Kármán Vortex Street [182, 183], the existence of Faraday pattern [184] and instabilities [185]. On the other side, GPE has allowed getting a good description of all these phenomena along with the micro-scale phenomena such as vortex nucleation [179], sound emission due to vortex reconnections [186] and Kelvin wave excitation [187], interaction of vortices with rarefaction solitary waves [188], role of vortices in superfluid turbulence [189].

1.4 Linear Regime of the Condensate

In a case where atom-atom interaction in the condensate becomes negligible ($g \sim 0$), GPE reduces to regular linear Schrödinger equation representing a single particle. Condensate can be taken to linear regime either by tuning the interactions to zero using Feshbach resonances or by releasing the condensate from the confining (trapping) potential. In the GPE, nonlinearity term is directly proportional to the density of the condensate. Thus, when the condensate is released from the trap, it starts to expand which makes the condensate density to decline, and within first few ms of trap removal, atom-atom interactions become negligible, putting the condensate in the linear regime. As the nonlinearity vanishes from the system, the condensate behaves more like an ideal gas. This regime can be used to model the textbook problem in quantum mechanics. One of the famous case being the “Quantum Bouncer” problem which has been already studied in the context of ultracold atoms, neutrons, and photon. Quantum Bouncer is a name given to a problem in which dynamics of a quantum particle/wavepacket falling in the presence of gravitational field and reflected from a hard wall is studied. Bouncing off a quantum wavepacket from a hard wall in a gravitational field has been investigated experimentally and theoretically in the various context, e.g. to examine the collapse and revival of the wavepacket, [190, 191], to observe the quantum effect of gravity [192, 193] and to test the equivalence principle [194, 195] etc.

1.5 Dissertation Outline

BEC being a well controlled and clean macroscopic quantum system has paved the path to explore the very puzzling quantum nature of matter and has been of great interest to experimentalists and theorists for a very long time. A lot has been done to explore its properties independently and to draw a link between the phenomena existing in other systems to BEC. In this thesis, we go ahead and contribute to the understanding of the nature and dynamics of a 2D ^{87}Rb Bose-Einstein condensate in two different regimes (non-linear and linear) experimentally and numerically. In non-linear regime, short-range atom-atom interactions present in the system remain dominant and in linear regime interaction present in the system becomes negligible. This thesis consists of parts

1. Numerical study: In this work, we probed the non-linear regime of the condensate through numerical simulations where we solve the nonlinear GPE. We revisited the phase imprinting method to generate matter wave dark solitons in the 2D condensate and studied the outcomes of imprinting smooth phase gradients (closer to experimental conditions) compared to a sharp phase gradient. We highlighted the effect of smooth phase gradient on the generation of the dark soliton, its instability, and long-term vortex decay dynamics. We pointed out the rich dynamics of the vortex dipoles stemming from the unstable soliton and proposed an alternate method to generate dark solitons in double well potential. We also reported a transition from Faraday pattern to transient soliton lattice in the condensate.

2. The second part of the thesis was pursued in motivation to implement the above numerical study in an existing experimental setup. In this part, we discuss the limitation to implement this numerical study and the possibility of modification of the setup to realize the same. We briefly describe our experimental setup and sequence which leads to the production of BEC followed by the characterization of condensate and the trap. In the latter part, we describe the results of an experimental and numerical study to probe the linear regime of the condensate. To investigate the linear regime, bouncing dynamics of the 3D spherical Rb condensate from a Gaussian barrier was studied which is popularly known as ‘Quantum Bouncer’ problem. This study resulted in the emergence of unusual fringe pattern in the condensate.

Chapter 2: Outlines the formalism and theoretical background of Bose-Einstein condensation. We present the derivation of theoretical concepts and mean-field methodology to derive nonlinear Schrödinger Equation called Gross Pitaevskii equation (GPE) which can model a dilute weakly interacting atomic Bose gas at zero temperature. We present the scaling or reduction of GPE to dimensionless form in 1D, 2D, 3D. These scaled equations are used to simulate the dynamics of the condensate numerically.

Chapter 3: Reviews the different method of solitons generation in condensate and describes the numerically conducted study to probe the nonlinear regime of the condensate. The content of this chapter is mainly adapted from the results of our published paper [196]. We discussed the popular phase imprinting method in the context of 2D condensates and studied the outcomes of imprinting a smooth phase gradients (experimentally likely condition) compared to the sharp phase gradient on the generation and instability dynamics of solitons. This chapter also highlights the effect of smooth phase gradient on long-term vortex decay dynamics and the formation of vortex dipoles stemming from the unstable soliton. Also, an alternate method to generate dark solitons in double well potential under periodic modulation of interactions is presented. We present the formation of a transient soliton lattice and coexistence of Faraday pattern and soliton lattice.

Chapter 4: Outlines the development of an experiment to probe the linear regime of the condensate. Part of the chapter presents the experimental setup and sequence used to prepare a 3D Rb BEC in a cross optical dipole trap and characterization of the trap. Rest of the chapter discusses the results of an experimentally and numerically conducted study to probe linear regime where the dynamics of a bouncing BEC from a Gaussian barrier is studied, and formation of unusual fringes is reported. The chapter also discusses some of the limitations of implementing the numerical study (mentioned in chapter 3) in the existing experimental setup.

Chapter 5: Summarizes and concludes the work of the thesis.

Chapter 6: Explores the possibility and discusses a modification to the existing setup for realizing the soliton lattice (discussed in chapter 3).

Chapter 2

BEC: Theoretical Background

2.1 Introduction

In this chapter, we lay out the foundation of essential theoretical concepts related to Bose-Einstein Condensation (BEC) of dilute weakly interacting gas. We derive Gross-Pitaevskiii Equation (GPE) under the mean-field approximation and present a dimensionless form of GPE which is more relevant and used in case of numerically simulating the dynamics of the condensate. This chapter also discusses a particular method used for numerically solving the GPE. In the end, we describe concepts related to Dark Solitons (DS), Vortices, Faraday Pattern (FP), and Boglibouv excitations.

2.2 Weakly Interacting Bose Gas

Modelling the dynamics of a dilute and weakly interacting Bose gas containing N atoms in an external potential at remarkably low temperature requires the construction of an N-body quantum wave function which would satisfy the Schrödinger equation. However, it is a complex task that is avoided by adopting a mean-field approach. This approach is based on two critical approximations:

1. The gas has to be dilute enough such that only two body (binary) interactions are relevant where these interactions are assumed to be a contact interaction, described by a delta function [45, 108, 110] of the form

$$V(\mathbf{r}-\mathbf{r}') = g\delta(\mathbf{r}-\mathbf{r}')$$

where $\mathbf{r}$, $\mathbf{r}'$ denotes the location of interacting particles and g denotes the interaction strength. All other interactions involving a higher number of particles are ignored.

2. The second approximation assumes that all the particles in the condensate are described by a single macroscopic wave function, $\Phi(\mathbf{r}, t)$ which is the classical field as all the particles share the same phase and quantum state. It is also assumed that no particles contribute to thermal or quantum fluctuations which is justified only in the limit of zero temperature. Although the theory has been extended and models have been built to account for finite temperature effects. However, in this thesis, we deal with zero temperature model (Gross-Pitaevskii Equation) which is capable of describing all the stationary and dynamic properties of the condensate to an excellent degree.

2.3 Mean Field Approach

In this section, we derive the Gross-Pitaevskii equation using mean field approximation [197]. To describe a closed system containing a dilute weakly interacting Bose gas of N atoms, an N-body wave function $\psi(\mathbf{r_1}, \mathbf{r_2}...\mathbf{r_N}, t)$ can be considered which obeys the Schrödinger equation

$$i\hbar\frac{\partial}{\partial t}\psi(\mathbf{r_1}, \mathbf{r_2}...\mathbf{r_N}, t) = \hat{H}\psi(\mathbf{r_1}, \mathbf{r_2}...\mathbf{r_N}, t) \tag{2.1}$$

where $\mathbf{r_i}$ denotes the position of i^{th} particle and $\hat{H}$ is the system Hamiltonian of the form,

$$\hat{H} = \sum_{k=1}^{N} \hat{h}_0(\mathbf{r_k}, t) + \frac{1}{2}\sum_{k,l=1}^{N} \hat{V}(\mathbf{r}_k, \mathbf{r}_l) \tag{2.2}$$

where $\hat{h}_0(\mathbf{r}, t) = -\frac{\hbar^2}{2m}\nabla^2 + V_{\text{ext}}(\mathbf{r}, t)$ denotes the contribution coming from the effects of a single particle in an external potential. The second term in the Hamiltonian comes from the binary interaction arising from the collision between the two atoms. The factor of half accounts for the fact that interactions are counted only once over the entire sum. Reformulating this system in a different representation using an orthonormal basis called occupation number basis, the wave function can be mapped as

$$\psi(\mathbf{r_1}, \mathbf{r_2}...\mathbf{r_N}, t) \to |\psi(t)\rangle = \sum_{n_1...n_\infty} c(n_1...n_\infty, t)\, |n_1...n_\infty\rangle \tag{2.3}$$

This basis arises from the fact that all the considered particles are indistinguishable and multiple particles can share any energetically accessible state. Here the number of particles in each state i is denoted by n_i which correspond to states with fixed energy ϵ_i. In the system, the number of states is infinite. However, the no. of particles (bosons) in the system is kept fixed as N. This implies that there are at most N states occupied. Here $c(n_1...n_\infty, t)$ are the appropriately chosen complex coefficients following the particle statistics rules (such as for bosons, coefficient must be symmetric) and normalization condition, so that sum over all the probabilities is 1 (unity),

$$\int |\psi|^2 d\mathbf{r} \rightarrow \sum_{n_1...n_\infty} |c(n_1...c_\infty)|^2 \frac{N!}{n_1!...n_\infty!} = 1 \tag{2.4}$$

Since the particles are indistinguishable, the term $\frac{N!}{n_1!...n_\infty!}$ is used to account for the fact that some sets of occupation numbers correspond to multiparticle states. Evolution of the system is entirely embedded in the values of complex coefficients c and the state vectors $|n_1...n_\infty\rangle$ remain time invariant. Movement of bosons between different states or energy levels can be conceived as the simultaneous destruction of a particle in a given state j and creation of a particle in the state i which can be mathematically described using creation $\hat{a}^\dagger$ and annihilation operators $\hat{a}$,

$$\hat{a}_j |n_1...n_i...n_j...n_\infty\rangle = \sqrt{n_j}\, |n_1...n_i...n_j - 1...n_\infty\rangle \tag{2.5}$$

$$\hat{a}_i^\dagger |n_1...n_i...n_j...n_\infty\rangle = \sqrt{n_i + 1}\, |n_1...n_i + 1...n_j...n_\infty\rangle \tag{2.6}$$

Annihilation and creation operators satisfy the bosonic commutation relations as follows,

$$[\hat{a}_i, \hat{a}_j^\dagger] = \delta_{ij} \tag{2.7}$$

$$[\hat{a}_i, \hat{a}_j] = [\hat{a}_i^\dagger, \hat{a}_j^\dagger] = 0 \tag{2.8}$$

Movement of a particle from state j to i is described through a product $\hat{a}_i^\dagger \hat{a}_j$ and binary interactions present in dilute gas is described by two particle changing state product $\hat{a}_i^\dagger \hat{a}_k^\dagger \hat{a}_j \hat{a}_l$. Using this formulation, original description of the system as given by Eq. (2.1) and Eq. (2.2) can be written as

$$i\hbar \frac{\partial}{\partial t} |\psi\rangle = \hat{H} |\psi\rangle \tag{2.9}$$

with,

$$\hat{H} = \sum_{ij} \langle i| \hat{h}_0 |j\rangle \hat{a}_i^\dagger \hat{a}_j + \frac{1}{2} \sum_{ijkl} \langle ik| \hat{V} |jl\rangle \hat{a}_i^\dagger \hat{a}_k^\dagger \hat{a}_j \hat{a}_l \tag{2.10}$$

where,

$$\langle i| \hat{h}_0 |j\rangle = \int \phi_i{}^*(\mathbf{r}) \hat{h}_0 \phi_j(\mathbf{r}) d\mathbf{r}$$

$$\langle ik| \hat{V} |jl\rangle = \int \int \phi_i^*(\mathbf{r}) \phi_k^*(\mathbf{r}') \hat{V}(\mathbf{r} - \mathbf{r}') \phi_l(\mathbf{r}') \phi_j(\mathbf{r}) d\mathbf{r}' d\mathbf{r}$$

where $V(\mathbf{r} - \mathbf{r}')$ is the two body interaction potential and $\phi_i(\mathbf{r})$ are the single particle eigenstates or the solutions of Schrödinger equation with no interaction present. Next, we introduce the Bose field operators for further simplification,

$$\hat{\psi}(\mathbf{r}, t) = \sum_i \hat{a}_i(t) \phi_i(\mathbf{r}) \tag{2.11}$$

$$\hat{\psi}^\dagger(\mathbf{r}, t) = \sum_i \hat{a}_i^\dagger(t) \phi_i^*(\mathbf{r}) \tag{2.12}$$

where $\hat{\psi}(\mathbf{r}, t)$ and $\hat{\psi}^\dagger(\mathbf{r}, t)$ represent the removal and addition of a particle at time t and location r respectively. The commutation relation for the Bose field operators can be written as

$$[\hat{\psi}(\mathbf{r}, t), \hat{\psi}^\dagger(\mathbf{r}', t)] = \delta(\mathbf{r} - \mathbf{r}')$$

and,

$$[\hat{\psi}(\mathbf{r}, t), \hat{\psi}(\mathbf{r}', t)] = [\hat{\psi}^\dagger(\mathbf{r}, t), \hat{\psi}^\dagger(\mathbf{r}', t)] = 0$$

Using these Bose operators, the Hamiltonian of the system can be written as

$$\hat{H} = \int \hat{\psi}^\dagger(\mathbf{r}, t) \hat{h}_0 \hat{\psi}(\mathbf{r}, t) d\mathbf{r} + \frac{1}{2} \int \int \hat{\psi}^\dagger(\mathbf{r}, t) \hat{\psi}^\dagger(\mathbf{r}', t) V(\mathbf{r} - \mathbf{r}') \hat{\psi}(\mathbf{r}', t) \hat{\psi}(\mathbf{r}, t) d\mathbf{r}' d\mathbf{r}$$

where $\hat{h}_0(\mathbf{r}, t) = -\frac{\hbar^2}{2m} \nabla^2 + V_{\text{ext}}(\mathbf{r}, t)$ is the single particle Hamiltonian as mentioned before. Using the earlier mentioned assumption which says the all interactions in the dilute gas at low temperature occur through elastic contact collisions, interaction potential can be written in the form of a delta function. The strength of the interaction is solely governed by s-wave scattering length a_s which results from the leading order approximation when scattering theory is employed to address the collisions in the condensate.

$$V(\mathbf{r} - \mathbf{r}') = g\delta(\mathbf{r} - \mathbf{r}')$$

where $g = \frac{4\pi\hbar^2 a_s}{m}$. By substituting the expression for the interaction potential in the Hamiltonian, we get,

$$\hat{H} = \int \hat{\psi}^\dagger(\mathbf{r},t)\hat{h}_0\hat{\psi}(\mathbf{r},t)d\mathbf{r} + \frac{g}{2}\int \hat{\psi}^\dagger(\mathbf{r},t)\hat{\psi}^\dagger(\mathbf{r},t)\hat{\psi}(\mathbf{r},t)\hat{\psi}(\mathbf{r},t)d\mathbf{r}$$

Now, we evaluate the evolution of Bose operators over time according to the Heisenberg equation of motion,

$$i\hbar\frac{\partial}{\partial t}\hat{\psi}(\mathbf{r},t) = [\hat{\psi}(\mathbf{r},t), \hat{H}] \tag{2.13}$$

By substituting the expression for $\hat{H}$ and expanding the commutator, Eq. (2.13) can be written as

$$i\hbar\frac{\partial}{\partial t}\hat{\psi}(\mathbf{r},t) = \int [\hat{\psi}, \hat{\psi}^\dagger \widehat{h_0}\hat{\psi}]d\mathbf{r} + \frac{g}{2}\int [\hat{\psi}, \hat{\psi}^\dagger\hat{\psi}^\dagger\hat{\psi}\hat{\psi}]d\mathbf{r}$$

$$= \int [\hat{\psi}, \hat{\psi}^\dagger]\widehat{h_0}\hat{\psi} + \hat{\psi}^\dagger[\hat{\psi}, \widehat{h_0}\hat{\psi}]d\mathbf{r} + \frac{g}{2}\int [\hat{\psi}, \hat{\psi}\dagger]\hat{\psi}^\dagger\hat{\psi}\hat{\psi} + \hat{\psi}^\dagger[\hat{\psi}, \hat{\psi}^\dagger]\hat{\psi}\hat{\psi} + \hat{\psi}^\dagger\hat{\psi}^\dagger[\hat{\psi}, \hat{\psi}\hat{\psi}]d\mathbf{r}$$

$$= \hat{h}_0\hat{\psi}(\mathbf{r},t) + g\hat{\psi}^\dagger(\mathbf{r},t)\hat{\psi}(\mathbf{r},t)\hat{\psi}(\mathbf{r},t)$$

Considering the mean-field approach, the field operator can be decomposed into two field operators which simplify the equation of motion further.

$$\hat{\psi} = \hat{\Psi}(\mathbf{r},t) + \hat{\delta}(\mathbf{r},t) \tag{2.14}$$

where $\hat{\Psi}(\mathbf{r},t)$ represent the field operator corresponding to the condensate in the lowest macroscopically occupied quantum state and $\hat{\delta}(\mathbf{r},t)$ represents the field operator for non-condensate atoms which can be atoms in the higher excited state or the atoms influenced by quantum mechanical fluctuations. Using the Bogoliubov approximation [17], condensate field operator can be replaced by a classical field $\Phi(\mathbf{r},t)$ which is associated with the macroscopic wave function of the condensate,

$$\hat{\Psi}(\mathbf{r},t) \approx \Phi(\mathbf{r},t) + \hat{\delta}(\mathbf{r},t) \tag{2.15}$$

where precisely, $\Phi = \langle\hat{\Psi}\rangle$ represents the ensemble average of the full field operator in a given ensemble which breaks the symmetry with respect to phase [198]. Additionally, it is assumed that due to a large number of particles in the condensate ($N_0 \gg 1$), the exact value of N_0 does not affect the state of the system significantly. In the limit of $T \to 0$, the contribution from the non-condensed part can be neglected, $\langle\hat{\delta}\rangle = 0$ and the condensate density with the total number of N_0 particle, therefore, can be written as

$$n(\mathbf{r}, t) = |\Phi(\mathbf{r}, t)|^2 \tag{2.16}$$

such that $N_0 = \int |\Phi(\mathbf{r}, t)|^2 d\mathbf{r}$. With the above mentioned approximation, Eq. (2.13) reduces to the nonlinear Schrödinger equation which is called as Gross-Pitaevskii Equation (GPE) as shown below

$$i\hbar \frac{\partial}{\partial t}\Phi(\mathbf{r}, t) = \hat{h}_0\Phi(\mathbf{r}, t) + g\Phi^*(\mathbf{r}, t)\Phi(\mathbf{r}, t)\Phi(\mathbf{r}, t) \tag{2.17}$$

$$= \left(-\frac{\hbar^2}{2m}\nabla^2 + V_{\text{ext}}(\mathbf{r}, t) + g|\Phi(\mathbf{r}, t)|^2\right)\Phi(\mathbf{r}, t) \tag{2.18}$$

Finally, we note that for a system in which the particle number is not conserved, calculations should be performed within the grand canonical ensemble [45] which leads to the modification of Hamiltonian $\hat{H} \to \hat{H} - \mu\hat{N}$ where $\hat{N} = \int \hat{\psi}^\dagger\hat{\psi} d\mathbf{r}$ is the number operator and μ is the chemical potential. With this modified Hamiltonian a physically equivalent version of GPE with a chemical potential term can be obtained by repeating the above derivation as

$$i\hbar \frac{\partial}{\partial t}\Phi(\mathbf{r}, t) = \left(-\frac{\hbar^2}{2m}\nabla^2 + V_{\text{ext}}(\mathbf{r}, t) + g|\Phi(\mathbf{r}, t)|^2 - \mu\right)\Phi(\mathbf{r}, t) \tag{2.19}$$

On the right side of the equation, the first two terms represent the energy of a single particle in an external potential, and the third nonlinear term represents the interactions between the multiple particles. The chemical potential, μ in the equation can be thought of as the measure of the energy required to add a particle to a system consisting of a large number of particles N. In terms of kinetic, potential and interaction energies of the system; chemical potential can be expressed as

$$\mu = \frac{(E_{\text{kin}} + E_{\text{pot}} + 2E_{\text{int}})}{N} \tag{2.20}$$

where,

$$E_{\text{kin}} = \int \frac{\hbar^2}{2m}|\nabla\Phi|^2 d\mathbf{r} \tag{2.21}$$

$$E_{\text{pot}} = \int V_{\text{ext}}|\Phi|^2 d\mathbf{r} \tag{2.22}$$

$$E_{\text{int}} = \int \frac{g}{2}|\Phi|^4 d\mathbf{r} \tag{2.23}$$

Time independent form of GPE can be obtained by fixing the potential as time independent with stationary state $\Phi(\mathbf{r}, t) = \Phi_0(\mathbf{r})$. Thus, the stationary GPE can be written as,

$$0 = \left(-\frac{\hbar^2}{2m}\nabla^2 + V_{\text{ext}}(\mathbf{r}, t) + g|\Phi_0(\mathbf{r})|^2 - \mu\right)\Phi_0(\mathbf{r}) \tag{2.24}$$

Although GPE is strictly valid for systems at $T = 0$, however, it successfully models the ultra-cold gases at finite temperatures provided the temperature is small compared to the critical temperature for the BEC [199]. Besides BEC, GPE also qualitatively captures the dynamical effects in liquid He II [200] and pulsars (highly magnetized rotating neutron star) [201] etc.

2.4 Excitations of BEC

Further, we consider the small amplitude excitations of the condensate which can be studied upon linearizing the time-independent GPE Eq. (2.24) around the ground state. Considering the small perturbation of the state Φ_0,

$$\Phi_0(\mathbf{r}, t) = \exp\left(-i\mu t/\hbar\right)\left\{\Phi_0(\mathbf{r}) + \sum_j \left[u_j(\mathbf{r})e^{-i\omega_j t} + v^*(\mathbf{r})e^{i\omega_j t}\right]\right\} \tag{2.25}$$

where u_j and v_j are the eigenfunctions which correspond to the linear response of the condensate to the external perturbations. $\pm\omega_j$ are the corresponding eigen frequencies which are generally complex valued. Substituting the $\Phi_0(\mathbf{r}, t)$ in Eq. (2.24) and keeping only linear terms in u_j and v_j, following coupled equations can be obtained

$$\left[\hat{h}_0 - \mu + 2g|\Phi_0|^2(\mathbf{r})\right]u_j(\mathbf{r}) + g\Phi_0^2(\mathbf{r})v_j(\mathbf{r}) = \hbar\omega_j u_j(\mathbf{r})$$

$$\left[\hat{h}_0 - \mu + 2g|\Phi_0|^2(\mathbf{r})\right]v_j(\mathbf{r}) + g\Phi_0^2(\mathbf{r})u_j(\mathbf{r}) = -\hbar\omega_j v_j(\mathbf{r})$$

where $\hat{h}_0$ is the single particle Hamiltonian. These equations are called Bogoliubov-de Gennes (BdG) equations which in general can be used to do stability analysis of any other stationary state (e.g. solitons) apart from the ground state of the condensate, which we will discuss later in this chapter. These equations provides the amplitude u_j and v_j with eigen frequencies $\omega = \omega_r + \omega_i$ of the normal modes of the system. Frequencies with zero imaginary part, represents the stable configurations. In case of homogeneous condensate $[v_{\text{ext}} = 0]$, the normal mode amplitude u_j and v_j are given as plane waves $u_0 \exp(i\mathbf{k}\cdot\mathbf{r})$ and $v_0 \exp(i\mathbf{k}\cdot\mathbf{r})$. Substituting this in BdG equation leads to the Bogoliubov dispersion relation as

$$(\hbar\omega)^2 = \left(\frac{\hbar^2 k^2}{2m}\right)\left(\frac{\hbar^2 k^2}{2m} + 2gn_0\right) \tag{2.26}$$

This indicates the small amplitude excitations of the stationary state $\Phi_0 = \sqrt{n_0}\exp(-i\mu t/\hbar)$ are always stable for the condensate with repulsive interactions as $\omega_i = 0$ for every $\mathbf{k}$. Small momenta excitations are characterized by a phonon dispersion relation $\omega = |\mathbf{k}|c_s$ where $c_s = \sqrt{gn_0/m}$ is the speed of sound. At large momentum values, dispersion becomes free particle spectrum. In case of attractive interactions ($g < 0$) speed of sound becomes imaginary, which indicates an exponential growth of long wavelength perturbations called modulational instability. As low momentum $\mathbf{k} \to 0$ modes become unstable, this is also referred as phonon instability.

2.5 Dimensionless Gross-Pitaevskii Equations

In numerical simulation of the condensate, scaled dimensionless form of GP equation is generally used. The values of the various parameters in such a equation are normalized on the scale of unity which reduces the chance of errors due to floating point representation in computers. As mentioned earlier, the phenomena of BEC can lead to the existence of superfluid behaviour at any scale ranging from micron size ultracold atomic BEC, to meter size superfluid helium containers, to kilometer scale neutron stars. Thus, a dimensionless equation can allow reformulating the calculations from one scale to another scale. There are mainly two methods to scale the GPE based on the presence or absence of trapping potential. A particular scaling is chosen by the needs of simulation, e.g. in some studies, as in the case of freely falling condensate in a gravitational field, GPE is scaled with the gravitational potential energy of the condensate.

2.5.1 Scaling of GPE in the Absence of a Trap

In case of absence of any external potential in the GPE, an infinite and homogeneous condensate with repulsive interaction can be considered. For this system, the ground state Φ will be independent of position $\mathbf{r}$ and time t, Thus GPE can be written as,

$$0 = \left(g|\Phi(\mathbf{r},t)|^2 - \mu\right)\Phi(\mathbf{r},t) \tag{2.27}$$

which suggests the constant homogeneous density, n to be

$$n = |\Phi(\mathbf{r},t)|^2 = \frac{\mu}{g} \tag{2.28}$$

By rescaling the wave function Φ as,

$$\bar{\Phi} = \frac{\Phi}{\sqrt{n}} \tag{2.29}$$

which suggests the spatial extent and time evolution of the system can be expressed in units of healing length $\xi = \hbar/\sqrt{mgn}$ and in units of $\tau = \frac{\hbar}{gn}$ respectively. The energy of the system and propagation speed of any density variation in the medium can be expressed in units of chemical potential μ and the sound speed of the system, $c_s = \sqrt{\frac{ng}{m}}$ respectively. These scales can be derived from dimensional arguments. These units are called "natural units". With rescaled quantity (denoted by the bar), dimensionless time-dependent GPE can be written as

$$i\frac{\partial}{\partial\bar{t}}\,\bar{\Phi}(\,\bar{\mathbf{r}},\bar{t}\,) = \left(-\frac{1}{2}\bar{\nabla}^2 + |\bar{\Phi}(\,\bar{\mathbf{r}},\bar{t}\,)|^2 - 1\right)\bar{\Phi}(\,\bar{\mathbf{r}},\bar{t}\,) \tag{2.30}$$

with the normalization condition for Φ as,

$$\int |\bar{\Phi}(\,\bar{\mathbf{r}},\bar{t}\,)|^2 d\mathbf{r} = 1 \tag{2.31}$$

where scaled parameters are given as,

$$\bar{t} = \frac{t}{\tau}, \quad \bar{r} = \frac{r}{\xi}, \quad \bar{E} = \frac{E}{\mu}, \quad \bar{v} = \frac{v}{c_s} \tag{2.32}$$

2.5.2 Scaling of GPE in the Presence of Trap

BEC in experiments usually prepared in a harmonic trap. To numerically simulate such cases, a different scaling is convenient. Considering a condensate trapped in a 3D symmetric harmonic trap $V(\mathbf{r}) = \frac{1}{2}m\omega^2\mathbf{r}^2$ with trap frequency ω. By scaling the GPE (2.19) with $\hbar\omega$,the dimensionless equation can be written as,

$$i\frac{\partial}{\partial\bar{t}}\bar{\Phi}(\,\bar{\mathbf{r}},\bar{t}\,) = \left(-\frac{1}{2}\bar{\nabla}^2 + g_{\bar{3D}}|\bar{\Phi}(\,\bar{\mathbf{r}},\bar{t}\,)|^2 + \bar{V}(\bar{\mathbf{r}}) - \bar{\mu}\right)\bar{\Phi}(\,\bar{\mathbf{r}},\bar{t}\,) \tag{2.33}$$

with normalization condition

$$\int |\bar{\Phi}(\,\bar{\mathbf{r}},\bar{t}\,)|^2 d\mathbf{r} = 1 \tag{2.34}$$

where scaled parameters are given as,

$$\bar{t} = t\omega, \quad \bar{r} = \frac{r}{a_0}, \quad \bar{E} = \frac{E}{\hbar\omega}, \quad \bar{\Phi} = \Phi N^{-1/2} a_0^{3/2} \tag{2.35}$$

$$\bar{g}_{3D} = \frac{gN}{\hbar\omega a_0^3} = \frac{4\pi a_{\mathrm{s}} N}{a_0}, \bar{v} = \frac{v}{a_0\omega}, \quad \bar{V} = \frac{1}{2}\bar{\mathbf{r}}^2 \tag{2.36}$$

Thus, in dimensionless form, the spatial extent is expressed in units of $a_0 = \sqrt{\frac{\hbar}{m\omega}}$ which is called harmonic oscillator length. This defines the extent of the wave function in the given harmonic trap in case of no interactions present in the system. Time and energy of the system are expressed in units of ω and $\hbar\omega$ respectively. The density of the condensate is expressed in units of Na_0^{-3}, and propagation speed of any density variation is expressed in units of $a_0\omega$

2.5.3 Dimensionless GPE for Condensate in Lower Dimensions

The low dimensional system exhibits rich physical phenomena and is of great interest in condensed matter physics. The properties of low dimensional condensate achieved in highly anisotropic traps have been studied extensively both theoretically [202] and experimentally [203]. For highly anisotropic trap geometries, GPE can be reduced to lower dimensions. For a given harmonic trapping potential with trap frequencies $\omega_x, \omega_y, \omega_z$ along x, y, z directions, important length scales such as harmonic oscillator length and healing length can be defined as,

$$a_{x,y,z} = \sqrt{\frac{\hbar}{m\omega_{x,y,z}}}$$

$$\xi = \frac{1}{\sqrt{4\pi n a_s}}$$

where a_{s} is the scattering length. If $a_{x,y,z} \gg \xi \gg a_{\mathrm{s}}$, then BEC is treated as a three dimensional entity. And if $a_z \ll \xi \ll a_{x,y}$, the extent of the condensate along the z-axis is so small compared to other two dimensions that effectively, the condensate can be treated as a two dimensional system and is generally referred to as a quasi 2D condensate. In this case, one can assume that the time evolution will not cause any excitation along z-axis. Any excitation along z-axis will require a large energy $\hbar\omega_z$ compared to the energy required to have excitations along the other two axes. Hence, the dynamics along z-direction can be considered effectively frozen by the tight confinement of the trap. Thus, it can be assumed that the condensate wave function along the z-axis is well described by the ground state wave function [204],

$$\Phi(\mathbf{r}, t) = \psi(x, y, t)\phi_0(z) \tag{2.37}$$

where $\phi_0(z) = 1/(\pi^{1/4} a_z^{1/2}) \exp(-z^2/2a_z^2)$ is the ground state of the harmonic trap along z -axis. Substituting the above wave function in Eq. (2.19) followed by multiplication on both sides by wave function ϕ_0 and integrating along z-direction results in an effective 2D GP equation,

$$i\hbar\frac{\partial}{\partial t}\psi(x, y, t) = \Big[-\frac{\hbar^2}{2m}\nabla^2{}_{x,y} + V(x, y) + g_{2D}|\psi(x, y, t)|^2 - \big(\mu - m{\omega_z}^2{a_z}^2/2\big)\Big]\psi(x, y, t)$$

where $g_{2D} = \frac{g}{\sqrt{2\pi}a_z}$. This equation can be made dimensionless by dividing both sides of the equation with $\hbar\omega_z$

$$i\frac{\partial}{\partial\bar{t}}\bar{\psi}(\bar{x}, \bar{y}, \bar{t}) = \Big(-\frac{1}{2}\nabla^2{}_{\bar{x},\bar{y}} + \bar{V}(\bar{x}, \bar{y}) + \bar{g}_{2D}|\bar{\psi}(\bar{x}, \bar{y}, \bar{t})|^2 - \bar{\mu}_{2D}\Big)\bar{\psi}(\bar{x}, \bar{y}, \bar{t}) \tag{2.38}$$

where $\bar{\mu}_{2D} = (\bar{\mu} - \frac{1}{2})$ with the normalization condition

$$\int |\bar{\psi}(\bar{x}, \bar{y}, \bar{t})|^2 d\bar{x}d\bar{y} = 1 \tag{2.39}$$

where scaled parameters are given as,

$$\bar{t} = t\omega_z, \quad \bar{x}, \quad \bar{y} = \frac{x}{a_z}, \quad \frac{y}{a_z}, \quad \bar{E} = \frac{E}{\hbar\omega_z}, \quad \bar{\psi} = \psi N^{-1/2} a_z \tag{2.40}$$

$$\bar{g}_{2D} = \frac{g_{2D}N}{\hbar\omega_z {a_z}^2} = \frac{4\pi a_s N}{\sqrt{2\pi}a_z}, \quad \bar{v} = \frac{v}{a_z\omega_z}, \quad \bar{V} = \frac{1}{2}\Big[\big(\frac{\omega_x}{\omega_z}\bar{x}\big)^2 + \big(\frac{\omega_y}{\omega_z}\bar{y}\big)^2\Big] \tag{2.41}$$

Eq. (2.38) is valid only if $g_{2D}|\psi(x, y, t)|^2 \ll \hbar\omega_z$ is satisfied locally at any time t. If this condition breaks, the wave function along the z-axis is no longer the Gaussian ground state, and a full 3D GPE needs to be solved in such a case.

Similarly for a quasi 1D condensate in a trap geometry with trap frequencies $\omega_x \ll \omega_{y,z}$ or harmonic oscillator length scale $a_{z,y} \ll \xi \ll a_x$, GPE can be reduced to one dimension. Considering the frozen dynamics along y and z direction the wave function of the condensate can be written as $\Phi(\mathbf{r}, t) = \psi(x, t)\phi_0(y, z)$ where $\phi_0(y, z) = 1/(\pi^{1/2} a_y^{1/2} a_z^{1/2}) \exp(-y^2/2a_y^2 - z^2/2a_z^2)$. By substituting this wave function in the time dependent 3D GPE 2.19 and then multiplying it with $\phi_0(y, z)$ term on both sides followed by an integration along y and z direction will lead to an effective 1D GPE,

$$i\hbar\frac{\partial}{\partial t}\psi(x,t)=\Big[-\frac{\hbar^2}{2m}\nabla^2{}_x+V(x)+g_{1D}|\psi(x,t)|^2-\big(\mu-m{\omega_y}^2{a_y}^2/2-m{\omega_z}^2{a_z}^2/2\big)\Big]\psi(x,t)$$

where $g_{1D}=g/2\pi a_y a_z$. This 1D GPE can be made dimensionless by dividing both side of the equation with the $\hbar\omega_z$

$$i\frac{\partial}{\partial\bar{t}}\bar{\psi}(\ \bar{x},\bar{t}\ )=\Big(-\frac{1}{2}\nabla^2{}_{\bar{x}}+\bar{V}(\bar{x})+\bar{g}_{1D}|\bar{\psi}(\ \bar{x},\bar{t}\ )|^2-\bar{\mu}_{1D}\Big)\bar{\psi}(\ \bar{x},\bar{t}\ ) \tag{2.42}$$

where $\bar{\mu}_{1D}=(\bar{\mu}-1)$ with normalization condition

$$\int|\bar{\psi}(\ \bar{x},\bar{t}\ )|^2d\bar{x}=1 \tag{2.43}$$

where scaled parameters are given as,

$$\bar{t}=t\omega_z,\quad \bar{x}=\frac{x}{a_z},\quad \bar{E}=\frac{E}{\hbar\omega_z},\quad \bar{\psi}=\psi N^{-1/2}a_z \tag{2.44}$$

$$\bar{g}_{\rm 1D}=\frac{g_{\rm 1D}N}{\hbar\omega_z a_y a_z}=\frac{4\pi a_s N}{2\pi a_y},\quad \bar{v}=\frac{v}{a_z\omega_z},\quad \bar{V}=\frac{1}{2}\left[\left(\frac{\omega_x}{\omega_z}\bar{x}\right)^2\right] \tag{2.45}$$

Eq. (2.42) is valid only if $g_{\rm 1D}|\psi(x,t)|^2\ll\hbar\omega_z$ is satisfied locally at any time t. If this condition breaks, the y, z dependent wave function is no longer the Gaussian ground state and a full 3D GPE needs to be solved in such a case.

2.6 Thomas-Fermi Approximation

The ground state of a non-interacting bosonic gas of N atoms in a spherical harmonic trap is a Gaussian wave function of the form

$$\Phi_0(\bar{\mathbf{r}})=\sqrt{N}\frac{1}{(\pi a_0^2)^{3/4}}\exp\left[-\mathbf{r}^2/2a_0^2\right] \tag{2.46}$$

where the size of the condensate is fixed by the harmonic oscillator length and the density $|\Phi_0|^2$ grows with N. However, the presence of atom-atom interactions modifies the size and distribution of the condensate in a harmonic trap. For a positive scattering length $a_{\rm s}>0$, interactions in the system are repulsive and for large number of atoms and at low temperatures, interaction energy dominates over the kinetic energy term significantly. Hence, neglecting the kinetic energy term in Eq. (2.24), we get

$$\mu\Phi_0(\mathbf{r})=\Big(V_{\rm ext}(\mathbf{r})+g|\Phi_0(\mathbf{r})|^2\Big)\Phi_0(\mathbf{r}) \tag{2.47}$$

which can be rearranged to get the density of the condensate as

$$|\Phi_0(\mathbf{r})|^2 = \frac{\mu - V_{\text{ext}}(\mathbf{r})}{g} \tag{2.48}$$

where $V_{\text{ext}}(\mathbf{r}) = \frac{1}{2}\mathbf{r}^2$. From this the approximate wave function of the condensate in an external potential can be written as

$$\Phi_0(\mathbf{r}) = \begin{cases} \sqrt{\frac{\mu - V_{\text{ext}}(\mathbf{r})}{g}}, & \text{if } \mu \geq V_{\text{ext}}(\mathbf{r}) \\ 0, & \text{otherwise} \end{cases} \tag{2.49}$$

This is known as the Thomas-Fermi approximation.

In this approximation, it can be seen that the density distribution is no more Gaussian and takes the form of an inverted parabola. This approximate profile plays an important role in initially modelling of the trapped condensate in experiments. This approximation is accurate near the center of the condensate and leads to a marginal error in the true density near the condensate edges or tails. This approximation can be used to analytically estimate the size of condensate. The extent of the condensate trapped in a harmonic trap known as Thomas-Fermi radius R_{TF}, and it is estimated as the distance from the centre (peak density location) to the location where density becomes zero (where $\mu = V_{\text{ext}}(\mathbf{r})$ is satisfied) as,

$$R_{TF} = \sqrt{\frac{2\mu}{m\omega^2}} \tag{2.50}$$

From the normalization condition, a relation between the chemical potential and number of atoms can be derived as

$$\mu = \frac{\hbar\omega}{2}\left(\frac{15Na_s}{a_0}\right)^{2/5} \tag{2.51}$$

where on substituting the value of μ in Thomas-Fermi radius, it can be noticed that the size of the condensate with repulsive interactions increases with the number of atoms as $N^{1/5}$ whereas in the case of a non-interacting case it is fixed by the harmonic oscillator length a_0. In the case of attractive interactions, the density tries to peak at the center as the number of atoms increases in the condensate where kinetic energy simultaneously tries to balance this increase. However, if the number of atoms, N exceeds a critical value N_{cr}, condensate becomes unstable and collapses in case of 2D and 3D geometries [48, 49]. In experiments, it is observed as an explosion of the condensate resulting in a smaller condensate. A critical number of atoms in a spherically symmetric trap can be obtained numerically and given as

$$N_{\mathrm{cr}}|a_{\mathrm{s}}|/a_0 = 0.575 \tag{2.52}$$

2.7 Numerical Simulation: Imaginary Time Propagation Method

To study the dynamics of condensate over time, initially, the ground state of the system needs to be calculated. Although on several occasions ground state of the system can be estimated analytically however numerical solution of ground state becomes necessary in case of complicated potential fields. The ground state is calculated numerically using eigensolvers. There are many methods to implement eigensolver such as inverse iteration and Lanczos method [205], systematic variational techniques [204], boundary eigenvalue methods [206] and imaginary time propagation method [207]. In this thesis, we adopt a simpler and efficient imaginary time propagation method to calculate the ground state numerically. Imaginary time propagation method relies on substitution of real time, t with imaginary time, $-it$ which make the GPE look similar to diffusion equation. On advancing the GPE in time, intially considered solution of the equation reaches a local equilibrium. This can be observed by considering a solution $\psi(r,t) = \sum_n \psi_n(r)\exp(-iE_n t/\hbar)$ as a superposition of eigenfunctions ψ_n with eigenvalues E_n. Using the imaginary time propagation ($t \to -it$), the wave function evolves with time as

$$\psi(r,t_i) = \sum_n \psi_n(r)\exp(-E_n t_i/\hbar) \tag{2.53}$$

It can be seen from the above equation, the wave function exponentially decays over time, and the contribution from higher energy eigenfunctions decays faster compared to low energy contribution. To inhibit the overall decay, the wave function is renormalised during propagation which forces the wave function to converge towards the ground state over sufficient transient time. Once the ground state is estimated, the real-time evolution of this state can be computed. Numerically to solve the GPE, we use time split step method [208]. A general non-linear Schrödinger equation can be written as

$$iu_t = u_{xx} + q|u|^2 u \tag{2.54}$$

or

$$u_t = i(\mathcal{L}u + \mathcal{N}(u)u) \tag{2.55}$$

where $\mathcal{L} = u_{xx}$ and $\mathcal{N}(u) = q|u|^2$. Solution of this equation at a given time $u(x, t+\tau)$ can be related to the earlier time solution as

$$u(x, t+\tau) \approx \exp\left[i\tau(\mathcal{L} + \mathcal{N}(u))\right].u(x,t) \tag{2.56}$$

In general Eq. (2.56) is accurate to first order but in some cases, if $|u|^2$ is time independent, this equation turns out to be exact. In time split method the right hand side of the equation is modified as

$$\exp\left[i\tau(\mathcal{L} + \mathcal{N}(u)\right].u(x,t) \approx \exp\left[i\tau(\mathcal{L})\right].\exp\left[i\tau\mathcal{N}(u)\right].u(x,t) \tag{2.57}$$

This expression is exact if $\mathcal{L}$ and $\mathcal{N}$ commute otherwise the splitting is accurate to first order. Thus ground state of the equation is evolved in small time steps in accordance with Eq. (2.57).

2.8 Dark Solitons and Snake Instability

A dark soliton is a nonlinear wave/structure which can arise in the condensate ($g > 0$) due to the balance of dispersion and nonlinearity (due to repulsive interactions). As mentioned in chapter 1, this structure propagates without distortion and remains remarkably stable against any perturbation or mutual collisions. Dark Soliton appears as a dip in the condensate density accompanied by a phase gradient across the dip. In 1D, the GP equation in the absence of an external trap supports a dark soliton solution given by

$$\psi(z,t) = \psi_0\left(i\frac{v}{c} + \sqrt{1-\frac{v^2}{c^2}}\tanh\left[\frac{z-vt}{\xi}\sqrt{1-\frac{v^2}{c^2}}\right]\right) \tag{2.58}$$

where $n_0 = |\psi_0|^2$ is the homogeneous background condensate density and v represent the velocity of the soliton. The density profile corresponding to the above solution has a minimum at $z = vt$ location and density value at the minima is defined as $n(0) = n_0 v^2/c^2$. For stationary solitons with $v = 0$ the density at minima is zero, and for a moving soliton with $v \neq 0$, the density at minima is nonzero. Due to zero density of a stationary soliton, they are referred to as black solitons whereas, moving solitons are generally referred to as gray solitons. It is important to note that as the velocity of soliton approaches the sound velocity, its depth decreases and width of the soliton defined as $w_s = \xi/\sqrt{1-\frac{v^2}{c^2}}$ increases.

The sharp phase gradient δ across the dip of a soliton wave function, which is another important characteristic of a dark soliton, and is related to its depth n_d and velocity as,

$$\frac{v}{c} = 2\cos\left(\delta/2\right) = \sqrt{1-\left(\frac{n_d}{n_0}\right)} \tag{2.59}$$

where the depth of soliton n_d is defined as the difference between background (unperturbed) density and density at the minima. A stationary soliton has a phase gradient of π across the minima. Dark solitons are stable only in a 1D condensate and become dynamically unstable due to transverse instabilities [132, 133, 209] in 2D and 3D condensate where the extent of the solitons along the other dimensions becomes larger than the healing length. In 2D and 3D condensate, solitons bend like a snake and finally break into a chain of vortex dipoles. Similar behaviour is also observed in the optical system too [210]. This instability is known as snake instability. This kind of instability can be prevented in quasi 1D condensate with tight confinement along the transverse direction [211]. DS is also prone to other instabilities like thermal instabilities which arises due to the interaction of soliton with the thermal cloud, leading to the acceleration of soliton towards the edge of the condensate and eventually, a disappearance of it [212]. As DS is the solution of a homogeneous system, the presence of an external trap/confinement breaks the integrability of the equation leading to another type of dynamical instability where solitons decay via sound emission while moving across an inhomogeneous background density [213, 214]. Solitons are also sensitive to quantum fluctuations as well [215].

In a 2D condensate, soliton exists like a depleted density line or a band while in 3D condensate it looks like a planar node. Solitons in 2D and 3D can also be generated in the form of a dark ring (called dark ring soliton) and nodal spherical shell (called spherical shell soliton) respectively [216, 217]. Many different theoretical studies have been conducted to stabilise solitons in higher dimensions using various techniques one of them being the using the long-range interactions [218]. Unstable solitons serve a way to generate a pool of vortices and anti-vortices [154] in the condensate which is not possible in case of general stirring techniques.

To comment on the stability of a DS in 2D and 3D, we consider a DS in a homogeneous condensate with uniform short-range repulsive interactions ($g > 0$). The homogeneous density of the condensate can be written as $n_0 = \mu/g$ and corresponding healing length is defined as $\xi = \hbar/\sqrt{mgn_0}$. Assuming a stationary DS along the z-direction (a nodal line in y-direction or plane in xy direction). The stationary solution of this kind of system can be given by the following GP equation

$$\mu\psi_0(z) = \left[-\frac{\hbar^2}{2m}\frac{d^2}{dz^2} + g|\psi_0(z)|^2\right]\psi_0(z) \tag{2.60}$$

$$\psi_0(z) = \sqrt{n_0}\tanh\left(z/\xi\right) \tag{2.61}$$

A simple solution $\psi_0(z)$ describing a DS in the z direction is exhibited by equation Eq. (2.60). The stability of this solution can be analyzed by means of Bogoliubov theory where small amplitude modulation of the nodal line or plane is considered in the form $\chi(\vec{r}, t) = u(z)\exp\left[i(\vec{q}\cdot\vec{\rho} - \epsilon t/\hbar)\right] + v(z)^*\exp\left[-i(\vec{q}\cdot\vec{\rho} - \epsilon^* t/\hbar)\right]$ where q corresponds to the momentum of transverse mode with energy ϵ and u and v are the perturbation eigenfunctions. Here $\vec{\rho} \in x, y$ and $\vec{r} \in x, y, z$. Introducing the ansatz $\psi_0(z) + \chi(\vec{r}, t)\exp\left(-i\mu t/\hbar\right)$ into Eq. (2.60) and linearizing in χ, leads to Bogoliubov-de Gennes (BDG) equations for the excitation energy ϵ and corresponding eigenfunctions $f_\pm = u \pm v$,

$$\epsilon f_-(z) = \left[-\frac{\hbar^2}{2m}\left(\frac{d^2}{dz^2} - q^2\right) + g|\psi_0(z)|^2 - \mu\right] f_+(z) \tag{2.62}$$

$$\epsilon f_+(z) = \left[-\frac{\hbar^2}{2m}\left(\frac{d^2}{dz^2} - q^2\right) + 3g|\psi_0(z)|^2 - \mu\right] f_-(z) \tag{2.63}$$

For each q, the lowest eigenvalue $\epsilon(q)$ provides the dispersion law. It is noted that the energy eigenvalues are purely imaginary for $q\xi < 1$. These imaginary modes grow exponentially with time and lead to dynamical instability of dark solitons [211]. This instability causes the nodal line or plane to bend like a snake and break into more vortex dipole pairs or vortex rings and generally called as snake instability.

2.9 Faraday Pattern in BEC

Pattern formation is observed in many different systems all around us such as in fluids, plasmas, in reacting and diffusing chemicals, heart muscle, and networks of excitable neurons in brains etc. Study of spatiotemporal properties of non-equilibrium systems is in itself a broad topic of interest to many scientists. Faraday patterns are spatially periodic patterns on the surface of a liquid that is excited by vertical oscillatory motion of a nonlinear liquid. These patterns were named after Michael Faraday when he first reported some observations of this kind in 1831 [219]. It was found that a certain minimum amount of power was required before the patterns could emerge. It was also noted that patterns appear unaffected by the shape of the container which is a characteristic feature of a nonlinear system and the waves that appear on the surface of fluid oscillate at half the driving frequency.

Faraday excitations are also called parametric resonances, as the oscillation of the fluid layer can be regarded as effective modulation of the acceleration due to gravity, which is one of the parameters of the system. Faraday waves were also found to form in the condensate as a result of the periodic driving of nonlinear interactions. Faraday patterns have been studied in atomic BEC theoretically [184] and experimentally [220]. The very nature of this spontaneous pattern formation is that a uniform state loses its stability against spatially modulated states. Nonlinearity in the condensate can be driven via Feshbach resonances [184] or by varying the trap parameters [220, 221]. The properties of this parametric driving have been explored in various BEC systems [222, 223]. In case of condensate, the patterns can offer important insights about collective excitations, since the periodicity of the pattern is determined by the wavenumber associated with the Bogoliubov excitation in resonance with half the driving frequency [224]. In chapter 3, we present a scenario where we explored a competition between the formation of Faraday pattern and a Dark Soliton lattice in a 2D Rb condensate under periodic modulation of interactions in the system.

2.9.1 Faraday Instability

Considering the evolution of a 2D homogeneous condensate with periodically modulated repulsive interactions described by a reduced 2D GP equation

$$i\frac{\partial}{\partial t}\psi(\vec{\rho},t) = \left(-\frac{1}{2}\nabla^2{}_{x,y} + g(t)|\psi|^2\right)\psi(\vec{\rho},t) \tag{2.64}$$

where $g(t) = g_{2D}[1+2\alpha\cos(2\omega t)]$. Spatially homogeneous temporally periodic solution of this equation can be written as

$$\psi_{\text{hom}}(t) = \exp\left[-i\frac{\mu}{\hbar}\left(t + \frac{\alpha\sin(2\omega t)}{\omega}\right)\right] \tag{2.65}$$

In order to study the symmetry breaking of the homogeneous state, a linear stability analysis can be performed with a suitable ansatz

$$\psi(\vec{\rho}, t) = \psi_{\text{hom}}(t) \left[1 + w(t) \cos(\vec{k} \cdot \vec{\rho})\right] \tag{2.66}$$

where $w(t) = u(t) + iv(t)$ is the amplitude of the perturbation and $\vec{k}$ represent the momenta in the xy plane. Substituting this solution in Eq. (2.64) and retaining only the first order terms in $u(t)$ results in the following Matheiu equation

$$\frac{d^2u}{dt^2} + \frac{1}{\hbar^2}\left[\epsilon(k)^2 + 4\alpha g_{2D} n_{2d} E_k \cos(2\omega t)\right] u(t) = 0 \tag{2.67}$$

where $\epsilon(k) = \sqrt{{E_k}^2 + 2g_{2D} n_{2d} E_k}$ is the Bogoliubov excitations with $E_k = \frac{\hbar^2 k^2}{2m}$, $g_{2D} = \frac{g}{\sqrt{2\pi} a_z}$ and n_{2d} is the homogeneous density of the condensate. Floquet theorem suggests the solutions of Mathieu equation is of the form $u(t) = c(t) \exp(\sigma t)$ where $c(t) = c(t + 2\pi/\omega)$ and $\sigma(k, \omega, \alpha)$ are the so-called Floquet exponent. For $\text{Re}(\sigma) > 0$, the amplitude of the perturbation grows, and the periodically modulated state becomes dynamical unstable against the formation of Faraday waves. The wavelength of the waves is dominated by the most unstable mode, i.e. the one with largest $Re(\sigma)$. For very small driving amplitude the system becomes unstable at the parametric resonances, $\epsilon(k) = n\hbar\omega$ $(n = 1, 2, ...)$. Using the Bogoliubov spectrum for the condensate, for any given driving frequency the most unstable mode is provided by the first resonance $\epsilon(k) = \hbar\omega$ which in turns give the typical size of the Faraday pattern.

Chapter 3

Dynamics of BEC: Non-Linear Regime

3.1 Introduction

In the previous chapter, we laid the basic theory of Bose-Einstein Condensate and the foundations of the Gross-Pitaevskii equation. In this chapter, we use the formulation developed in the previous chapter to numerically simulate the dynamics of a condensate in the nonlinear regime where short-range atom-atom repulsive interactions in the condensate are considered. In this chapter, we focus on the generation of Dark Solitons (DS) in 2D condensate and study their instability dynamics. We revisit the method of phase imprinting and examine the outcomes of imprinting smooth phase gradients (closer to experimental realizations) compared to the sharp phase gradient. In the end, we propose an alternate method to generate DS in a double-well potential under periodic modulation of interactions and report the formation of a transient soliton lattice and coexistence of Faraday Pattern in the condensate under certain conditions. The contents of this chapter are adapted from the results of our published work in ***Physical Review A***, **95**, 043618 (2018) [196]

3.1.1 Dark Solitons: Generation and Instability Dynamics

Dark solitons (DSs) are the most fundamental, localized nonlinear excitations appearing in various systems, [144–149, 225] including Bose-Einstein condensates (BECs) [141, 142, 226], with defocusing non-linearity and they are characterized by a localized dip in the background density. Various techniques have been employed to generate matter wave DSs, for instance, phase imprinting [72, 131, 153, 227], density engineering [73, 228, 229] and a combination of both – also called as quantum state engineering [154, 230–232]. In addition, the formation of DSs has been reported for experiments, in which a condensate is flowing past an obstacle realized via laser induced dipole potential [233, 234], as well as through interference of condensates initially prepared in multi-well potentials [235, 236]. If a bose gas is quenched across the BEC phase transition via Kibble-Zureck mechanism[157, 158, 167], DSs may also appear spontaneously in condensates. Besides the experimental investigations, there has been numerous theoretical studies [237–242] discussing novel ways to generate and study solitons, including their unique properties.

At zero temperature, the stability of a DS demands a quasi-one-dimensional condensate, i.e., the transverse extension of the condensate is required to be less than the healing length [136, 211, 213, 243]. Otherwise, the soliton becomes dynamically unstable against transverse excitations, so-called the snake instability (SI). SI leads to the bending of the nodal stripe (plane) in a two-dimensional [244, 245] (three-dimensional) background, which eventually breaks up into vortices and sound excitations [132]. It has been experimentally observed in both matter wave [154] and optical DSs [134, 210]. At finite temperatures, thermodynamic instability may lead to the decay of dynamically stable DSs [209]. In the trapped case, even at zero temperature, DSs may exhibit dissipative losses due to the emission of sound waves and its repeated collisions with the latter [72, 246–248]. In general, the sound waves mediated dissipation of DS may occur if it encounters an inhomogeneity in the background density [249]. Non-conventional and exotic DS-like excitations are also predicted to exhibit in 2D condensates [245, 250–252].

A dark stripe undergoing SI decays into a chain of vortices with opposite topological charges or the so-called vortex dipoles (VDs), a problem which has been addressed in the context of both non-linear optics [134, 210, 253–255] and in atomic condensates [245, 256–258], including fermionic superfluids [259]. If the transverse extension of the condensate is not large enough, the VDs recombines back to form the dark stripe and will undergo SI again. This process keeps repeating in time [234, 256]. As the transverse size increases, more vortices are formed along the nodal stripe. Complementary to SI dynamics, it has also been shown that the various vortex configurations can be seen as bifurcating states from a DS stripe [260]. The complex dynamics of vortices [261–263] including that of VDs [176, 180, 262, 264–274] in an inhomogeneous interacting condensate is a subject of its own merit. The motion of a vortex is strongly affected by the interaction with other vortices and the geometrical confinement. For instance, two vortices with same topological charge precess around each other, whereas with opposite charges move together with a linear velocity along the direction of flow between them. A VD may annihilate [175, 176, 268, 275–277] upon collision with other vortices or by emitting sound waves [278], a process that might play a big role in realizing the Onsager vortex states [279, 280].

3.2 Snake Instability

DSs can appear as defects in the background density if we drive the initial state of the condensate into a dynamically unstable configuration. A simple way to achieve this is by imprinting a phase gradient in the condensate wave function, and in Sec. 3.4 we discuss alternative techniques to achieve it. In this section, we focus mainly on the real-time dynamics of a 2D TF condensate with a phase gradient imprinted on it. We consider a BEC of N atoms confined in a harmonic trap: $V_t(\mathbf{r}) = m(\omega_x^2 x^2 + \omega_y^2 y^2 + \omega_z^2 z^2)/2$ where ω_α is the trap frequency along the α axis. To simplify, we take $\omega_z \gg \omega_{x,y}$ such that the dynamics of the condensate along the z-axis is frozen and the system can be effectively described by a two-dimensional (2D) Gross-Pitaevski equation (GPE):

$$i\hbar\frac{\partial\psi(x,y,t)}{\partial t} = \left[\frac{-\hbar^2\nabla^2}{2m} + V_t(x,y) + g_{2D}|\psi(x,y,t)|^2\right]\psi(x,y,t), \tag{3.1}$$

where $\psi(x,y,t)$ describes the condensate wave function in the xy plane, $V_t(x,y)$ is the radial part of the harmonic confinement and $g_{2D} = g/\left(\sqrt{2\pi}l_z\right)$ is the effective coupling constant in 2D with $g = 4\pi\hbar^2 aN/m$.

The validity of Eq. (3.1) demands $l_z < \xi$ where $l_z = \sqrt{\hbar/m\omega_z}$ and ξ is the healing length [203]. We solve Eq. (3.1) in real time starting with the initial solution $\psi(x,y,t=0) = \psi_0(x,y)\exp[i\theta(x)]$, where $\psi_0(x,y)$ is the ground state solution of Eq. (3.1) obtained via imaginary time evolution and $\theta(x)$ is the $x-$dependent initial phase. By introducing a phase gradient along the x-axis, the dark solitons are generated with nodal lines parallel to the y-axis [72, 281]. First we take $\theta(x) = \pi/2$ for $x < 0$ and

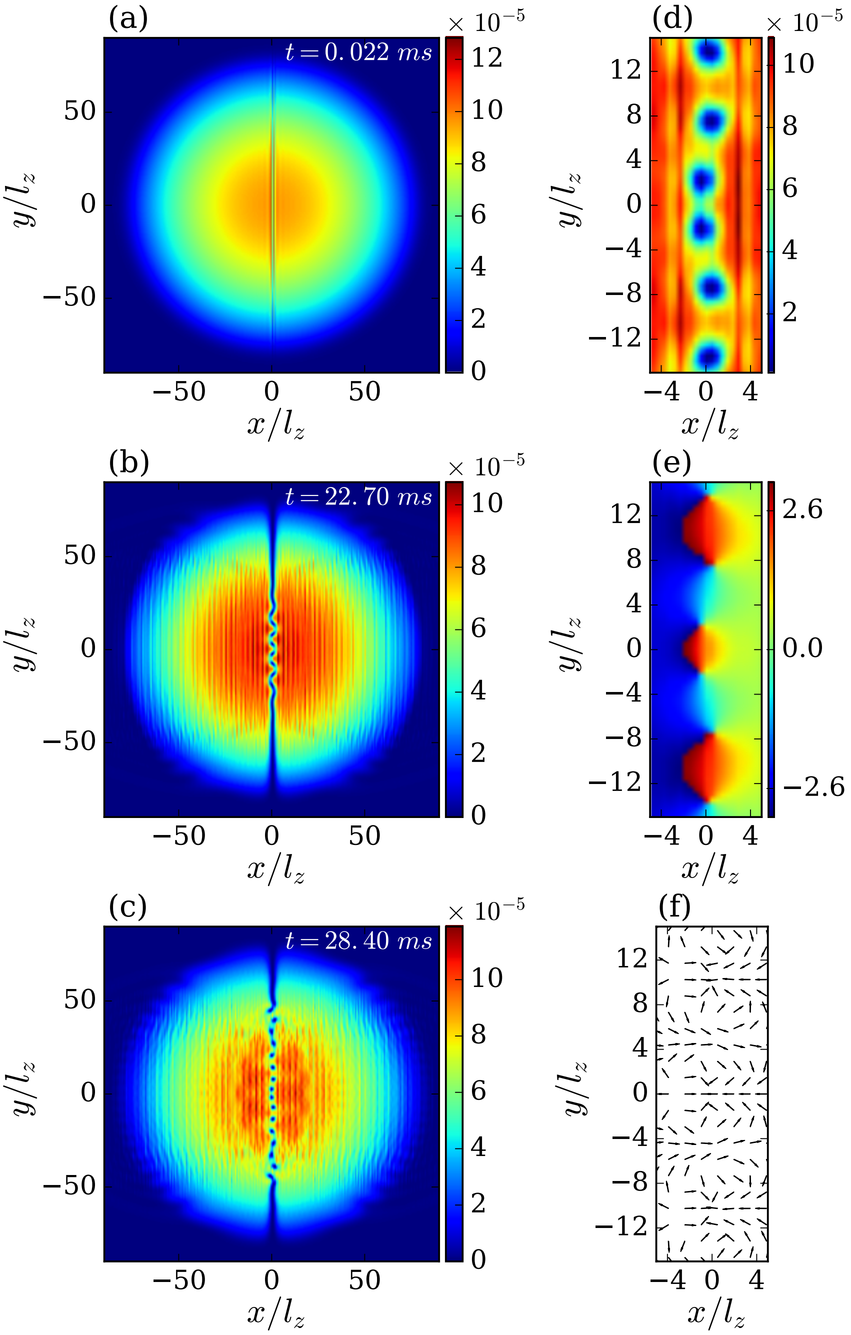

Figure 3.1: Dynamics of dark soliton: The time evolution of the scaled condensate density $n(x, y, t) = |\psi(x, y, t)|^2$ of a rubidium BEC with $N = 10^5$ atoms , $a = 109\ a_0$ (where a_0 is the Bohr radius), $\omega_x = \omega_y = 2\pi \times 10$ Hz and $\omega_z = 2\pi \times 700$ Hz, with an initial phase: $\theta(x) = \pi/2$ for $x < 0$ and $\theta(x) = -\pi/2$ for $x \geq 0$. (a) The condensate density at $t = 22\ \mu$s shows the formation a nodal stripe which eventually transforms into a stationary DS. (b) The SI first develops at the center of the condensate. (c) A transient stripe of VDs emerge, and in (d) we show the VDs at the centre of the condensate. The phase and velocity fields corresponding to (d) are shown in (e) and (f) respectively.

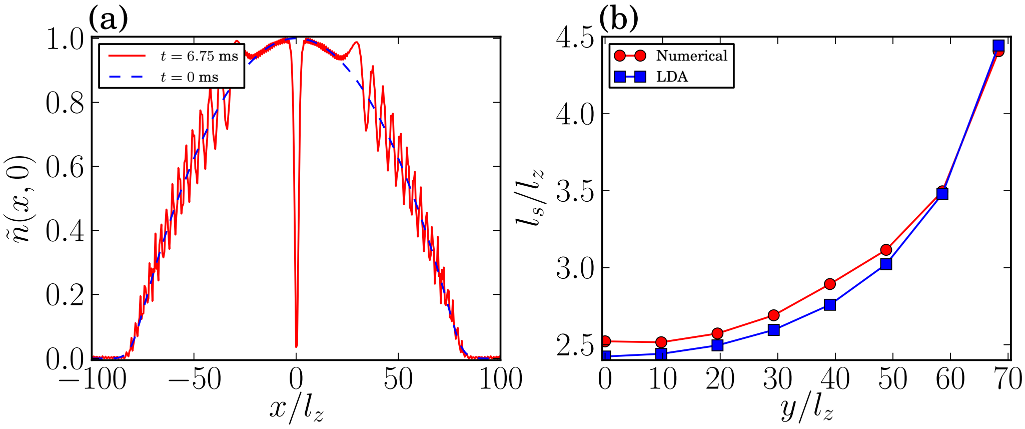

Figure 3.2: Width of dark soliton across the condensate: (a) The TF density profile $\left(|\psi(x, y = 0)|^2\right)$ at $t = 0$ (dashed line) and the emerged solitons at $t = 6.75$ ms (solid line). (b) The numerical results (filled circles) for the width $l_s(y)$ of the stationary DS as a function of y is compared with that of LDA with a TF profile (filled squares). The BEC setup is same as that of the Fig. 3.1.

$\theta(x) = -\pi/2$ for $x \geq 0$, which introduces a sharp gradient at $x = 0$ with a phase difference of π. The resulting dynamics of the condensate is shown in Fig. 3.1(a)-(f).

In the initial stage, a nodal stripe is developed [see, Fig. 3.1(a)] which eventually turns into a stationary DS at the center of the BEC, accompanied by sound waves and very shallow gray solitons. The former then undergoes SI [see, Fig. 3.1(b)], which leads to the formation of a transient stripe of VDs [see, Fig. 3.1(c)] and additional sound excitations [132, 154]. The SI has been attributed to the appearance of imaginary [211] or complex modes [132] in the Bogoliubov spectrum of a DS. Note that, the emanated sound waves during the phase imprinting feed up the unstable modes and enhance the SI. In addition, we observe the formation of a large number of gray secondary solitons.

There are other ways of creating shallow solitons in condensates, for instance, by generating shock waves, which shed DSs or by perturbing a stationary DS [282]. Typically, very shallow DSs disintegrate quickly after hitting the boundary. Since the size of the condensate is much larger than the width (l_s) of the DS, we can describe the stationary soliton using the local density approximation (LDA)[283, 284]. The width l_s of a stationary DS in a homogeneous background is provided by the healing length ξ and is $\propto 1/\sqrt{n_h}$, where n_h is the uniform density of the condensate. Using the LDA, we can approximate the y-dependent width of DS as $l_s(y) = \hbar/\sqrt{m g_{2D} n_0(y)}$ [285]

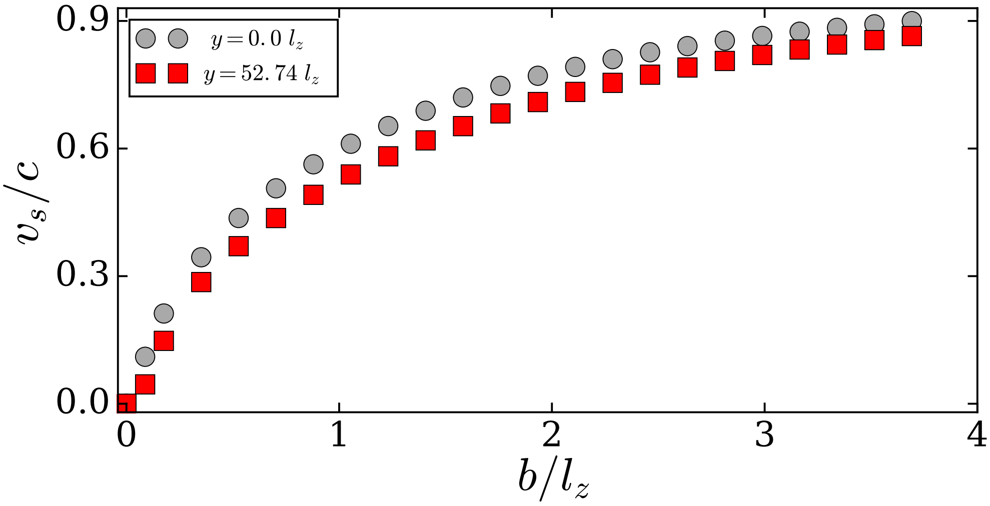

Figure 3.3: The subsonic local velocity v_s along the x-axis of the dark soliton as a function of b at different locations along the y-axis. For both curves, we calculated the velocity at $x = 1.5\ l_z$. At large values of b, v_s saturates to the speed of sound c, and also the center of the soliton moves faster compared to the edges. The setup is same as that in Fig. 3.1.

calculated at $x = 0$, where $n_0(y) = |\psi_0(x = 0, y)|^2$. If we assume a Thomas-Fermi (TF) profile, the condensate density becomes $n_0(x, y) = \mu/g_{2D}\left[1 - x^2/R_x^2 - y^2/R_y^2\right]$ for $\{x \leq R_x\ \&\ y \leq R_y\}$ otherwise $n_0(x, y) = 0$ with $R_{x,y}^2 = 2\mu/\left(m\omega_{x,y}^2\right)$. As we move away from the centre towards the edge of the condensate l_s increases as a function of y since the density decreases. In Fig. 3.2, we compare the numerical results for l_s with that of LDA using TF profile. They are found to be in excellent agreement. For the numerical result, the l_s is calculated at an instant of time at which the nodal stripe has completely developed into a stationary soliton, and after which the width of the DS hardly changes before undergoing SI.

Further, we have noticed that the SI of DS develops first at the center of the condensate [see Fig. 3.1(b)] and later it spreads across the entire soliton. We explain this behaviour using LDA as follows. The SI in a homogeneous background is attributed to the imaginary low-momentum transverse excitations [211] as stated above. They appear for momenta $0 \leq q\xi \leq 1$ with a maximum value of $\mu_h/4$ at $q\xi = 1/\sqrt{2}$, where q is the quasi-momentum and $\mu_h = g_{2D}n_h$ is the chemical potential of the homogeneous density. The maximum imaginary mode provides us the growth rate and hence determines the time scale at which the SI develops, which is $\tau = 4/\mu_h$.

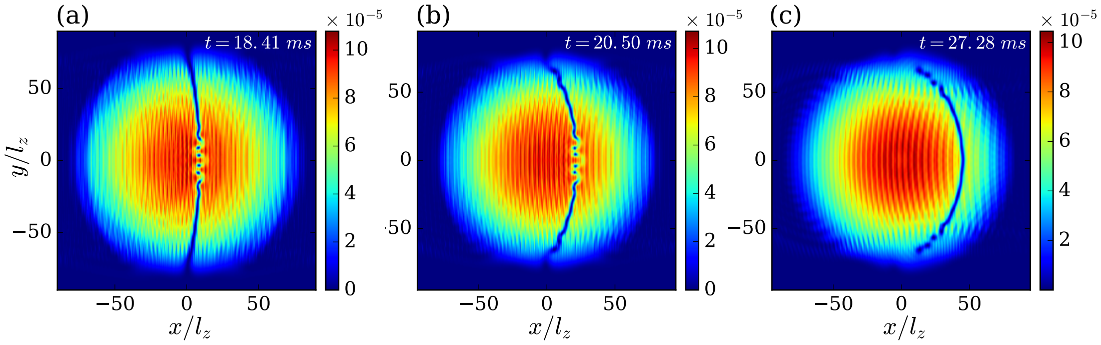

Figure 3.4: The SI dynamics for different b is depicted through the condensate density: (a) The SI develops first at the centre for $b = 0.05\ l_z$. (b) The SI develops both at the centre and the edges simultaneously for an intermediate value of $b = 0.2\ l_z$. (c) For sufficiently large values of $b = 0.75\ l_z$ the instability occurs first at the edges. In the later stage, the whole DS breaks up into vortex dipoles. Note that, larger the b shallower the soliton is, hence faster it propagates. The setup is same as that in Fig. 3.1.

Using LDA for the inhomogeneous case, we get $\tau(y) = 4/[g_{2D}n_0(y)]$, which indicates that the instability grows faster at the center compared to that in the edge. *Smooth phase gradient*: at this point, we replace the sharp phase gradient with a smooth one, $\theta(x) = (\pi/2)\tanh(x/b)$, which varies over a width b [237]. Interestingly, the characteristics, SI and post-SI dynamics of the DS depend crucially on the parameter b. Note that, $b = 0$ corresponds to the sharp gradient scenario discussed above and in that case, a stationary DS is created at the centre of the condensate. When b is nonzero, the phase becomes continuous at $x = 0$ and as expected, instead of a stationary soliton, a primary DS with a nonzero subsonic y dependent velocity $v_s(y) \approx c[1 - n_d/n_0(y)]^{1/2}$ along the x-axis is created, where $c = \sqrt{gn_0^{MAX}/m}$ is the speed of sound calculated at the maximum density n_0^{MAX} and n_d is the density depth of the DS. Since n_d decreases with increase in b, the velocity v_s increases, as shown in Fig. 3.3. At large values of b, the velocity v_s saturates to c [72]. The density dependence of the soliton velocity results in the bending of the nodal stripe during time evolution [see Fig. 3.4], which is unrelated to the SI dynamics.

The SI dynamics is also strongly modified by the parameter b. For small b, the instability process is analogous to that of the stationary case discussed above, in a way that the instability grows first at the center of the soliton stripe, see Fig. 3.4(a), then progress to the rest of the stripe. In contrary, as b increases, the instability appears

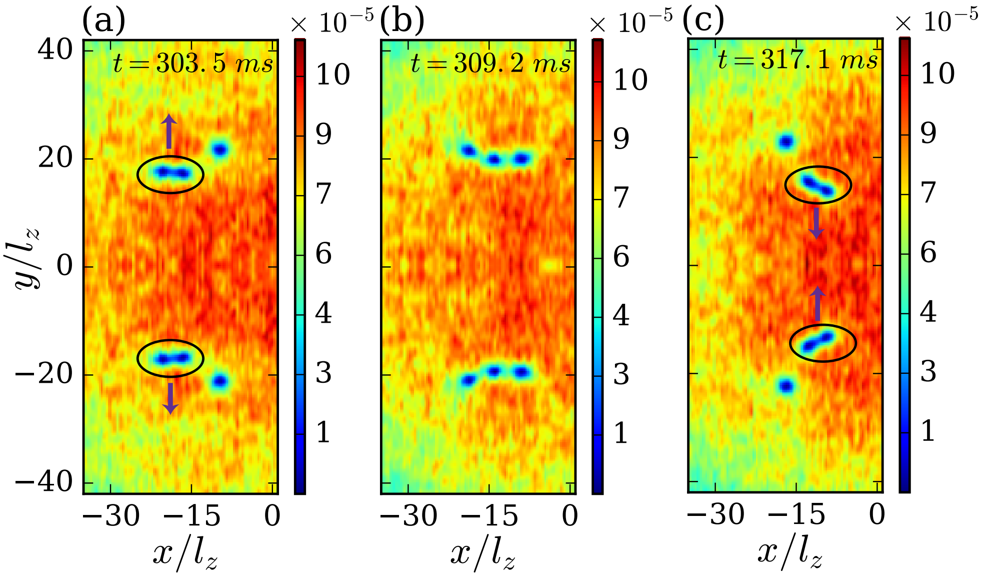

Figure 3.5: Vortex dynamics: (a) Two lone vortices are approached by two vortex dipoles and in (b) when they reach close to each other. In (c), an exchange of vortices has been taken place and a new pair of vortex dipoles are created. The setup is same as that in Fig. 3.1 with an initially imprinted sharp phase gradient. The initial and final VDs are indicated by ellipses and direction of propagation of VDs are shown by arrows.

simultaneously at the center as well as at the edges, leaving an intermediate fragment of DS unaffected. Hence, by the time SI develops in the intermediate region, the vortex dipoles are already created at the center and the edges, see Fig. 3.4(b). If b is further augmented, the instability occurs first at the edges as shown in Fig. 3.4(c), then propagate towards the center. Later, the entire soliton breaks up into VDs. Note that for sufficiently large values of b, very shallow solitons are formed with $v_s \sim c$ which dissipate before the SI develops.

3.3 Vortex Dynamics

The extended time evolution of the phase imprinted condensate reveals very rich and interesting scenarios in the vortex dynamics, especially of VDs. A stationary DS breaks up into an unstable configuration of a stripe of VDs, which eventually disperses into a gas of interacting vortices and VDs. A fraction of vortices break up from the VD stripe disperse towards the trap boundary (low-density regime) and precess around the trap center with either clockwise or anti-clockwise rotation depending on their vorticity. In the course of time, we observe the following frequent events:

1. vortex pair annihilation, where two vortices of opposite charge approach each other, then coalesce into a neutral dark lump [245, 286] (the same is termed as vortexonium [280]) which subsequently into sound excitations. Vortexonium is a spatially localized state, characterized by a phase step identical to that of a dark soliton, and it may revert to vortex dipole by hitting the boundary. VD annihilation has been reported in a BEC experiment [176], including in the context of superfluid turbulence [175]. The vortexonium may annihilate or decays to a smaller one, in the course of collision with a vortex or a VD. The vortexoniums those form at the trap boundary from the vortices which precess, propagate towards the trap center and decays into density excitations.

2. Among vortexoniums we found two scattering events, in one case two of them collide with each other, then emerge out intact and move away [245]. In the second case, after the collision one decays while the other breaks up into a VD. It is difficult to pinpoint on what condition each of these processes occurs independently and may depend on the kinetic energy of the vertexoniums at the instance of collision.

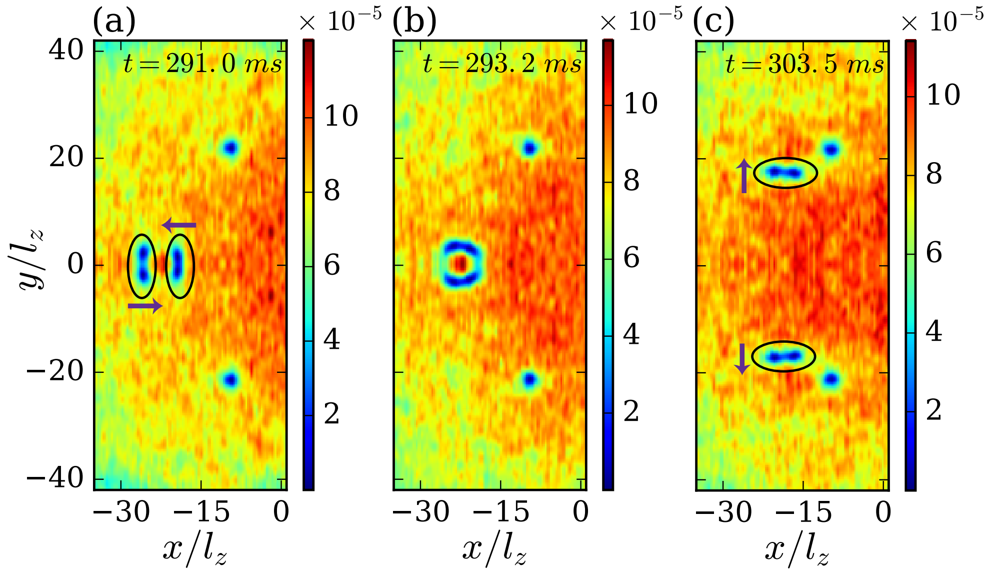

Figure 3.6: Vortex dynamics: (a) The collision of two counter-propagating VDs. (b) Upon collision they exchange vortices and form a new pair of VDs. The new pairs propagate opposite to each other in a direction perpendicular to the axis of collision, as shown in (c). The initial and final VDs are indicated by ellipses and direction of propagation of VDs are shown by arrows.

3. A VD, after colliding with a lone vortex, form a new VD and a new single vortex [197, 286]. Two such process happening simultaneously are shown in Fig. 3.5. The nature of dynamics, either flyby or exchange processes, depends on the relative velocity and the impact distance between theVD and the single vortex [286]. While approaching the single vortex, the VD slows down (also the energy of VD increases) hence, undergoing structural modifications, in particular, the vortex-antivortex separation increases. Finally the antivortex of the original VD merges with the single vortex forming a new VD, accompanied by radiative losses as sound excitations. The new VD propagates in a direction opposite to that of the initial one resulting in a *back scattering.*

4. A pair of VDs upon head to head collision, break up and exchange their partners, leading to the formation of a new pair of VDs, see Fig. 3.6. The new ones move perpendicular to the initial direction of propagation, as well as opposite to each other.

5. Two VDs approaching each other would either convert into two vortexoniums or annihilate one among them upon collision.

The parameter b indirectly influences the vortex dynamics. In particular, for sufficiently large b, the solitons first break from the edges into VDs, as mentioned above, then they quickly coalesce into vortexoniums. Finally, two adjacent vortexoniums collide, and one of them gets annihilated. This process repeats, resulting in the decline of the number of vortices as time progresses. We observed that as b increases the annihilation process is more frequent causing a faster decrement in vortex number, see Fig. 3.7. The oscillations in the vortex decay curve is due to the transitions between vortexoniums and VDs. The effective decay in the number of vortices, N_v, is well captured by the phenomenological rate equation [175],

$$\frac{dN_v}{dt} = -\Gamma(b)N_v^2, \tag{3.2}$$

where the decay coefficient $\Gamma(b)$ depends on b. The results according to the rate equation is shown as solid lines in Fig. 3.7. Another interesting feature we noticed is that, at sufficiently large b, DS travels faster, and breaks directly into vortexoniums at the boundary. This indicates that VDs are not necessarily the direct consequence of SI in 2D, depending on the nature of DS and its background density, it may break directly into vortexoniums. Note that sound excitations are generated during the nucleation of DSs, after the phase imprinting. To understand their role in the dynamics discussed above, we numerically look at the real-time evolution starting from the stationary DS solution of the GPE. The SI is then triggered by a very small initial random noise, which is negligibly small compared to the sound excitations emerge from the phase imprinting. In contrary to the dynamics of the phase-imprinted condensates, here we observe two effects. (i) The SI has slow down, since in the phase-imprinted case the presence of sound excitations enhanced the SI, and (ii) The vortex-anti vortex annihilation process is faster, which is evident from the initial stages of the dynamics, as shown in Fig. 3.7, which also supports the results that the presence of density perturbations may suppress the annihilation processes [275].

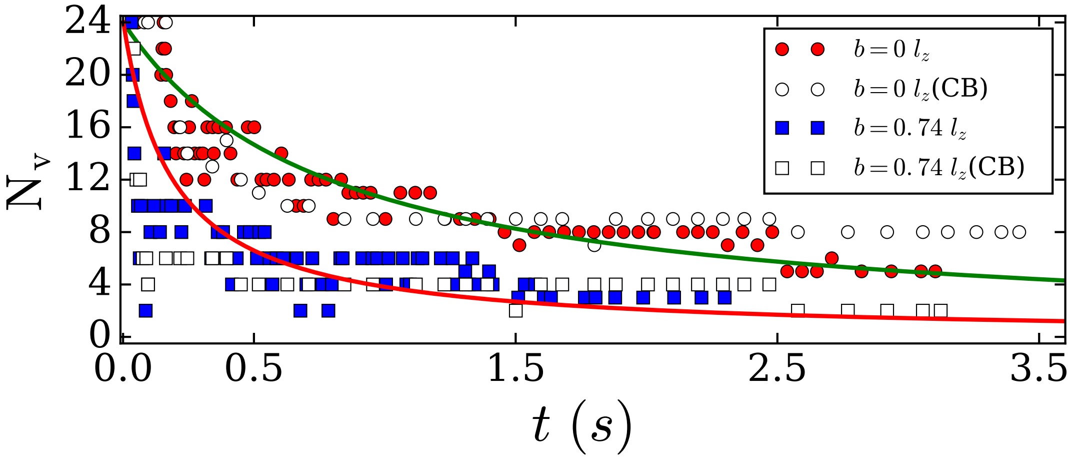

Figure 3.7: Long term decay of vortices: Plot shows the number of vortices as a function of time for two different b. Larger the value of b, faster the decay of vortices. The filled circles and squares are obtained by starting from a TF solution with an imprinted phase, whereas the empty circles and squares are for the cases in which time evolution starts with the dark solitons in a clean background (CB). The solid lines are calculated using the rate equation given in Eq. (3.2) with $\Gamma(0) = 0.053\ \mathrm{s}^{-1}$ and $\Gamma(0.74) = 0.22\ \mathrm{s}^{-1}$. The oscillations in the vortex decay curve is due to the transitions between vortexoniums to VDs and vice versa. The setup is same as that in Fig. 3.1. The origin of the time is taken at the point at which the DS completely breaks up into VDs, which is of the order of milli seconds.

3.4 Alternative Techniques for Soliton Generation

In this section, we discuss alternative techniques for the generation of DSs in BECs and the corresponding dynamics in a 2D condensate. The methods involve the use of an external potential barrier and time-dependent interactions, $g_{2D}(t)$. A potential barrier can be induced by an optical dipole potential or a far-detuned laser field. Generation of 1D solitons due to the sudden removal of the potential barrier is theoretically studied in [231, 287], and is also experimentally demonstrated [228, 233, 234]. It has shown that the creation of DSs require the system to be in a non-linear regime where the interaction energy dominates the kinetic part [234, 288]. The characteristics of the solitons also depend crucially on the initial phase difference between the disconnected condensates, for instance, a phase difference of π may lead to the formation of a stationary soliton [288] accompanied by very shallow solitons, similar to that discussed in Sec. 3.2. The number of solitons can also be controlled by fine tuning the initial separation between the condensates.

3.4.1 Gaussian Barrier and Time Dependent Interaction

We consider the same setup of BEC as in Sec. 3.2 with an additional Gaussian x-dependent potential barrier : $V_G(x) = V_0 \exp(-x^2/2d^2)$ of width d and height V_0, at the center of the trap. Hence, effectively we have a double well potential along the x-axis. Now, introducing the time-dependent interaction leads to the dynamical formation of solitons. In other words, the nodal stripe which is not a DS created by the potential barrier acts as a source of DSs in the presence of $g_{2D}(t)$. Below, we consider both linear and periodic variation of g in time [289]. Note that, any non-zero V_0 breaks the radial symmetry of the condensate, and for sufficiently large V_0 and d, the condensate splits symmetrically into two disconnected BECs along the x-axis.

3.4.2 Linear Variation of g in Time

Here, we consider the linear variation of scattering length a in time t, such that

$$g_{2D}(t) = \begin{cases} g_{2D} + \delta g \ \alpha t, & 0 < \alpha t \leq 1 \\ g_{2D} + \delta g, & \alpha t > 1, \end{cases} \tag{3.3}$$

where δg is the difference and α is the rate at which g is varied over a time $\tau = 1/\alpha$. In the presence of the Gaussian barrier, $g(t)$ leads to the formation of DSs in

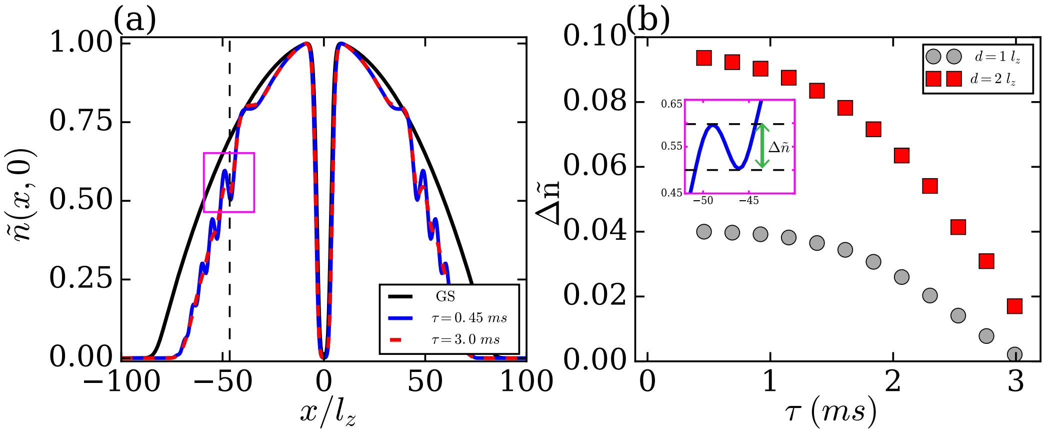

Figure 3.8: Generation of gray solitons in a double well potential under temporal variation of short range interactions: (a) The density profiles $\tilde{n}(x, y = 0) = l_z^2|\psi(x, y = 0)|^2$ for the ground state (GS) (black solid line) and the emerged solitons for different ramp times, $\tau = 1/\alpha = 0.45$ ms (blue solid line) and $\tau = 3$ ms (red dashed line) are shown. All plots are renormalized with its corresponding maximum density and the snapshots are taken at different instants of time for different τ. (b) Relative soliton depth (filled circles) for the width $d = 1\ l_z$ and $d = 2\ l_z$ (filled squares) as a function τ is plotted. The soliton depths are calculated at the same location [$x = 46.5\ l_z$, shown with a box in (a)] in the condensate, shown by dashed vertical line in (a). The definition of $\Delta\tilde{n}$ is schematically shown in the inset of (b), which corresponds to the box in (a). The BEC setup is same as that of the Fig. 3.1, and for both (a) and (b) we take $\delta g = -g_{2D}/2$.

the condensate [see Fig. 3.8(a)]. The properties of the soliton depend on V_0, d, α and δg. Hence, by controlling these parameters, the DSs can be generated in a more controlled way. As we have found, both increment and decrement in g lead to the formation of solitons. If the ramping of $g(t)$ fulfills the adiabatic criteria [290, 291], the condensate adiabatically follows the instantaneous ground state, and as a result, no solitons are generated. This has two immediate consequences on the properties of DSs; as α decreases, for a fixed δg: (i) the number of solitons decreases and (ii) they get shallower and shallower [see Fig. 3.8(b)]. On a similar note, for a fixed α, the soliton depth and also the number of solitons increases withan increase in δg. Note that, even for sufficiently short ramping time τ with $|\delta g| = g/2$, the solitons are very shallow [see Fig. 3.8(b)]. That means, the formed solitons travel close to the speed of sound, that may cause difficulties to track them in the experiments. The life time of DSs created in the setup considered in Fig. 3.8 for $\tau = 0.4$ ms is about $15 - 20$ ms.

Below, we consider the periodic modulation of interactions, there the soliton depths are augmented significantly, with qualitatively new features emerging.

3.4.3 g Periodic in Time

In this section, we take $g_{2D}(t) = g_{2D}[1+2\gamma\sin(2\omega_m t)]$, where γ and ω_m are respectively the amplitude and frequency of the modulation. As we show below, the numerical results for the dynamics of the system depend crucially on whether the initial state has a noise or not. In experimental setups always, there exist noise in the form of thermal or quantum fluctuations. They play an important role in, for instance, spontaneous symmetry breaking (SSB). A prime example for SSB is the formation of FPs in condensates by the parametric modulation of interactions [184, 220], in which the noise triggers the population of Bogoliubov modes according to the wave number selection or parametric resonance condition: $\epsilon(k) = \hbar\omega_m$. The Bogoliubov spectrum of a 2D homogeneous condensate is $\epsilon(k) = \sqrt{E_k\left(E_k + 2g_{2D}n_0\right)}$, where $E_k = \hbar^2k^2/2m$ with k being the quasi-momentum. For sufficiently small values of V_0 and large values of d we can still fairly approximate the spectrum of the trapped case with that of the homogeneous case within LDA for $k > 2\pi/R_{x,y}$. This low momenta cutoff introduces a low-frequency limit for the modulation frequency to observe pattern formation. Also, it has to be less than ω_z to preserve the 2D nature of the condensate.

Noise free:- Without noise, the FPs are not observed with the periodic modulation of the g_{2D}. Even for small V_0 we observe the formation of 2D DSs. In contrary to the linear quench, for the periodic case the depth of the gray soliton increases as a function of time and also the DSs are created continuously from the center of the condensate. As a result, a transient 1D lattice of 2D DSs is formed after a sufficiently long time, with the lattice periodicity depends crucially on the modulation frequency ω_m. Later, the lattice melts due to the SI and results in a denser gas of vortices compared to the previous cases. The periodic modulation eventually results in heating and the destruction of the condensate. Hence the formed vortices may decay thermally as well. The rate of heating depends on both the amplitude and the frequency of modulation.

Note that, due to the inhomogeneity in the density, the periodicity at the centre is different from that of the edges of the condensate. The lattice periodicity, provided by the wavelength $\delta\lambda$, calculated at the center, as a function of ω_m for different V_0 is shown in Fig. 3.9. Interestingly, the behaviour of $\delta\lambda$, is found to be very close to the

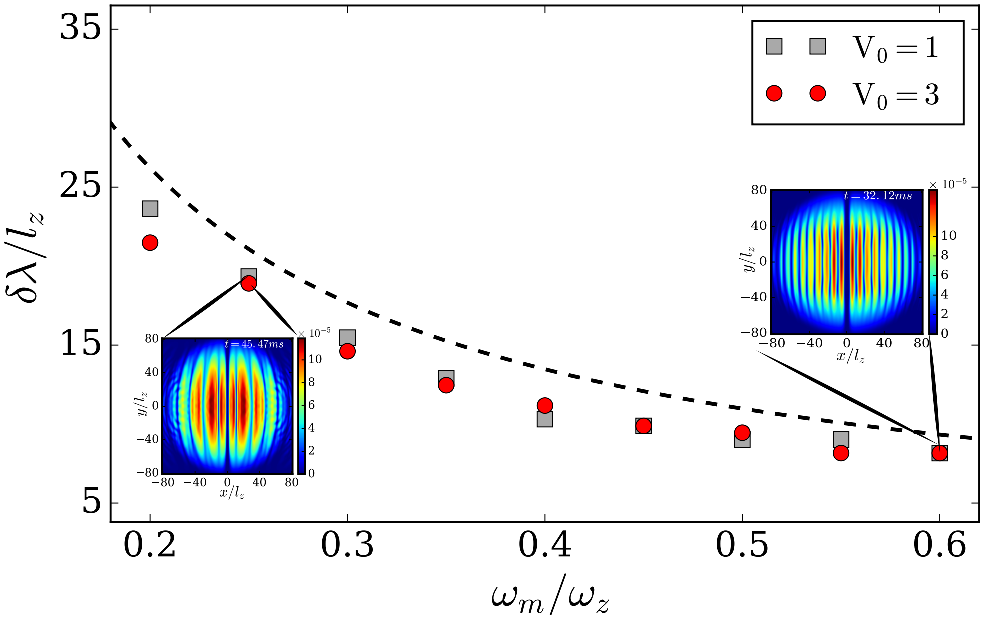

Figure 3.9: Periodicity of DS lattice: Plot shows the change in DS lattice periodicity as a function of modulation frequency, ω_m for $V_0 = 1\ \hbar\omega_z$ (squares) and for $V_0 = 3\ \hbar\omega_z$ (circles) with $\gamma = 0.2\ \omega_z$ and $b = 0.86\ l_z$. The two insets show the density snapshots for $V_0 = 3\ \hbar\omega_z$ at $\omega_m = 0.25$ and $\omega_m = 0.6\ \omega_z$. The dashed line shows, $1/k = 1/\epsilon^{-1}(\omega_m)$, the wavenumber corresponding to the Bogoliubov frequency ω_m. The BEC setup is same as that of the Fig. 3.1.

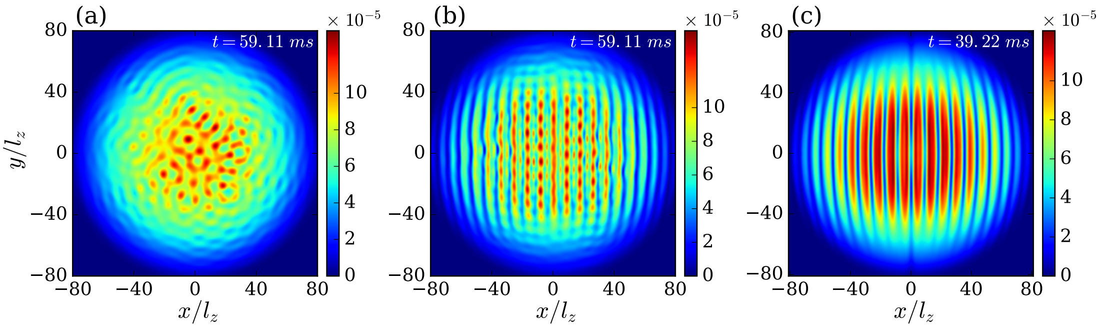

Figure 3.10: Competition between Faraday pattern and DS lattice formation: (a) Faraday patterns for $V_0 = 0$. (b) Co-existence of Faraday patterns and 2D DS lattice for $V_0 = 0.003\ \hbar\omega_z$. (c) Formation of pattern-free, transient DS lattice for $V_0 = 0.1\ \hbar\omega_z$. For all plots $\alpha = 0.2$ and $\omega_m = 0.6\ \omega_z$. The BEC setup is same as that of the Fig. 3.1. The extended time evolution of (b) and (c) are shown in Fig. 3.12.

wave number corresponding to the Bogoliubov frequency ω_m (dashed lines in Fig. 3.9) of the condensate at $V_0 = 0$. This indicates that identical to the case of FPs, there is a wave number selection for DS lattice, closely connected to the Bogoliubov spectrum of the unmodulated condensate. This is also evident from Fig. 3.9 that $\delta\lambda$ hardly changes with V_0 for sufficiently large V_0.

With noise:- The presence of the noise leads to an interesting scenario where the soliton formation and FPs co-exist, depending on the strength of V_0. In the absence of the potential barrier ($V_0 = 0$) the FPs emerge as a result of parametric modulation of g_{2D} [see Fig. 3.10(a)], with the wave number selection governed by the Bogoliubov modes as discussed above. For small and non-zero V_0, the pattern and DS lattice co-exist as shown in Fig. 3.10(b). Due to the presence of DSs, the FP exhibits a 1D character with density modulations along the y axis, and have the same periodicity as that of the DS lattice. Note that, the presence of the pattern reduces the *darkness* of the DSs. For large V_0 we see the formation of a pattern-free DS lattice [see Fig. 3.10(c)], which eventually undergoes snake instability and breaks up into a gas of VDs. With large V_0, the soliton formation is enhanced, resulting in the fast formation of the lattice, which suppresses the pattern formation in the condensate. The lifetime of the lattice ($\tau_{lattice}$) as a function of V_0 is shown in Fig. 3.11 for two different modulation frequencies. At small values of barrier height, $\tau_{lattice}$ depends strongly on V_0, and it saturates for sufficiently large values of V_0.

The instability dynamics crucially depends on the strength of V_0. For any V_0, the instability emerges first at the solitons near the boundary, since they are created before those at the center of the condensate. Interestingly, for low V_0 the presence of Faraday patterns give rise to a characteristically different instability dynamics for the DSs at the center of the condensate. The DS stripes embedded with FP break up into vortexoniums through a transient square pattern of density peaks [see Fig. 3.12(a)-(b)]. In contrary, for large V_0 when there is no FP, they directly break up into VDs [see Fig. 3.12(c)-(d)]. The corresponding phase plots are also shown in Fig. 3.12(e)-(h).

Finally, we want to comment that similar results can be obtained by making either the potential barrier or the trapping frequency become time-dependent instead of interactions.

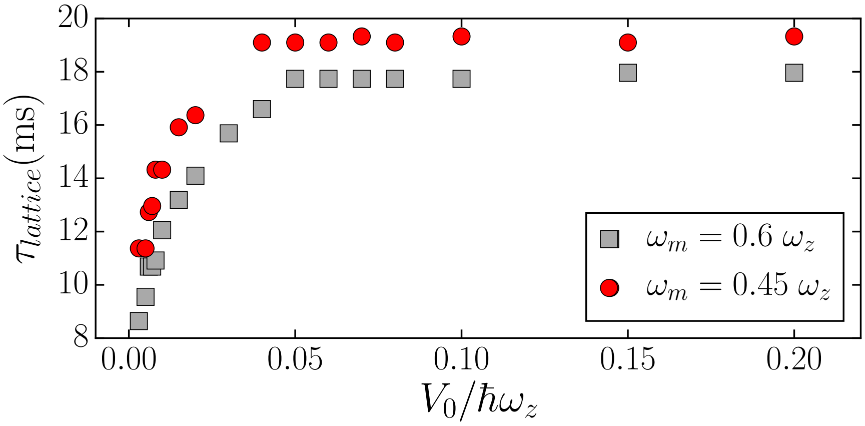

Figure 3.11: DS lattice lifetime: Plot shows the lifetime of the lattice ($\tau_{lattice}$) as a function of V_0 for two different ω_m. The setup is same as that for the Fig. 3.10. The lifetime $\tau = \tau_2 - \tau_1$, where τ_1 is the time at which the lattice is stabilized to a time-independent periodicity, and τ_2 is the time at which the outer DSs are unstable.

3.5 Experimental Realization

Next, we intended to implement the proposed alternative scheme to generate soliton lattice in our existing experimental setup where we routinely produced a 3D condensate of ^{87}Rb in a crossed optical dipole trap. We found that in the given geometry of our trap, in-trap condensate size was small ($\sim$ 15 - 20 μm) compared to the size of the barrier (the blue-detuned optical knife) ($\sim$ 60 μm) which was prepared to split the condensate into two halves. To observe the emergence of 2D soliton lattice, we will need to transform the trap from 3D to 2D, along with imaging system. This work will be pursued in the near future on the existing experimental setup, the route to achieve it will be discussed in chapter 6.

3.6 Summary

In this chapter, we numerically analyzed the long-time dynamics of SI of 2D DSs in a TF condensate of rubidium atoms, with repulsive contact interactions. The DS was dynamically generated in the BEC by an initially imprinted a phase gradient. The soliton properties, as well as the nature of SI and post-instability dynamics, found to depend substantially on the spatial width of the phase gradient. The VDs emerging

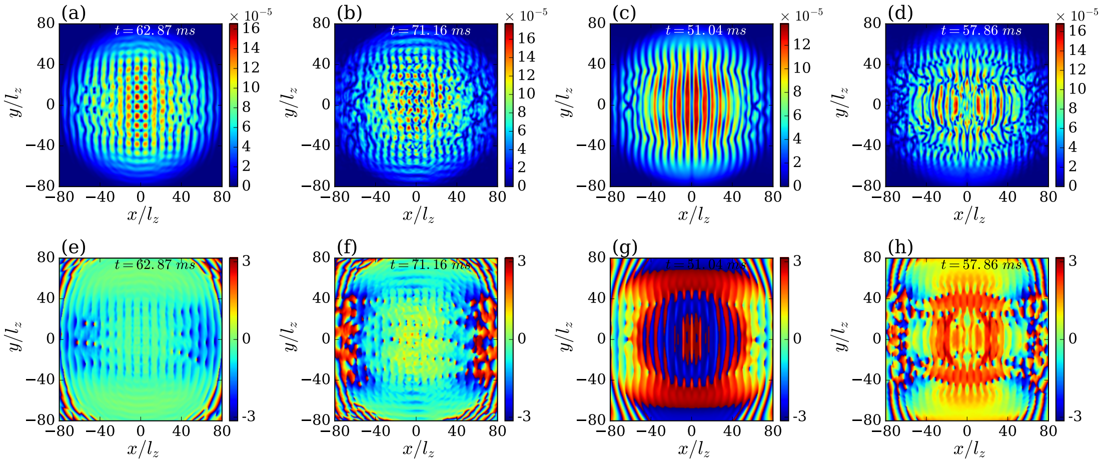

Figure 3.12: Instability dynamics of DS lattice: (a) and (b) shows the extended time evolution of the state shown in Fig. 3.10 (b). The phase plots corresponding to (a) and (b) are shown in (e) and (f) respectively. (c) and (d) show the extended time evolution of the state shown in Fig. 3.10 (c), with corresponding phase plots in (g) and (h). (a) and (b) are for $V_0 = 0.003\ \hbar\omega_z$ whereas (c) and (d) are for $V_0 = 0.1\ \hbar\omega_z$. All other details of the setup are same as that of Fig. 3.10.

from the unstable DS exhibited exciting dynamics such as the formation of vortexoniums, vortex annihilation, and exchange processes. The effective decay in the number of vortices was indirectly influenced by the spatial extension of the phase gradient. We discussed the alternative techniques for the DS generation, based on time-dependent interactions and an external Gaussian barrier. We observed that for the linear variation of interactions, the properties of the DS can be controlled by quench time. A transient DS lattice emerged in the condensate for the parametric modulation of interactions, with lattice periodicity depending on the frequency of modulation. Interestingly, the scenario was perceived to be richer by the co-existence of Faraday patterns and the transient DS lattice together. The SI dynamics of the soliton-lattice was significantly modified by the presence of FP.

Chapter 4

Dynamics of BEC: Linear Regime

4.1 Introduction

In the previous chapter, we discussed numerical results on the generation of solitons by phase imprinting method and their instability dynamics. In addition, the decay dynamics of vortex pairs and an alternative scheme to generate solitons in double well potential was reported. In the end, we discussed some of the limitations in realising this numerical study in our current experimental setup. Numerical studies mentioned in the previous chapter probe the non-linear regime of the condensate where interactions in the system remained dominant. Here, we investigate the other side, where atom-atom interactions in the condensate become negligible. In this chapter, we probe the less explored linear regime of the condensate where it behaves more like an ideal gas.

Condensate could be put in linear regime either by tuning the interactions using Feshbach resonances [292, 293] or by removing the confining (trapping) potential, the latter being a more straightforward way. When the condensate is released from the trap, it starts to expand, which decreases the condensate density. As discussed in chapter 2, the strength of the nonlinearity depends directly on the density of the condensate. Therefore, within first few ms of trap removal, the atom-atom interactions become negligible, whereby the condensate enters into the linear regime.

In this chapter, first, we provide a brief overview of the experimental setup and the sequence to produce a condensate of ^{87}Rb atoms in a crossed optical dipole trap followed by trap characterisation using parametric resonances and numerical modelling. Later, we discuss an experiment where we release the condensate from the trap, let it fall under gravity and encounter an optical barrier (placed below the trap) on its way while it falls. This optical barrier (formed by a focused blue detuned laser beam) is seen as a Gaussian hill by the falling atoms. This experimental scheme is similar to Ref. [294] where the dynamics of a BEC bouncing off an optical flat sheet was studied and multiple reflections of BEC were observed. This setup is generally referred to as a “Quantum Bouncer” and has been studied with ultracold atoms, neutrons, and photons. Bouncing a quantum wave packet from a hard wall in a gravitational field has been investigated experimentally and theoretically in various contexts, e.g. to study collapse and revival of the wave packet, [190, 191], to observe the quantum effect of gravity [192, 193] and to test the equivalence principle [194, 195] etc.

In our setup, we not only witnessed interesting reflection dynamics of the condensate from the Gaussian barrier but also found the emergence of a peculiar fringe pattern in the condensate. We studied this setup numerically using GP equation and mentioned some of the challenges in numerically simulating the dynamics which could qualitatively reproduce the outcomes of the experiment. In the end, we comment on the possibility of converting this fringes into solitons, given the interactions in the system are increased.

4.2 Experimental Setup: BEC Production

Formation of ^{87}Rb condensate was realised in a cross optical dipole trap. The experimental setup mainly consists of an effusive oven source which supplies the thermal beam of atoms, a Zeeman slower to slow down the atoms below the capture velocity, an Ultra High Vacuum science chamber (glass cell) which forms the trapping region, magnetic field generated by a pair of current carrying coils in anti-Helmholtz configuration (quadrupole coil), adequate laser beams for cooling, trapping and imaging system with an EMCCD camera for detection. The entire BEC experiment is controlled with computer programs written in LabView. Atoms slowed by Zeeman slower are loaded in a standard six-beams Magneto-Optical-Trap (MOT) for cooling. The details of the experimental design and setup until MOT stage can be found in the previously published thesis of our lab [1] which describes the production of BEC in an Electro-pneumatically transformed QUIC magnetic trap. The same setup was modified to produce BEC in crossed optical dipole trap where a 1064 nm, 20W CW fiber laser (model No. YLR-20-1064-LP-SF from IPG, Photonics) was used to implement a crossed dipole trap. Two

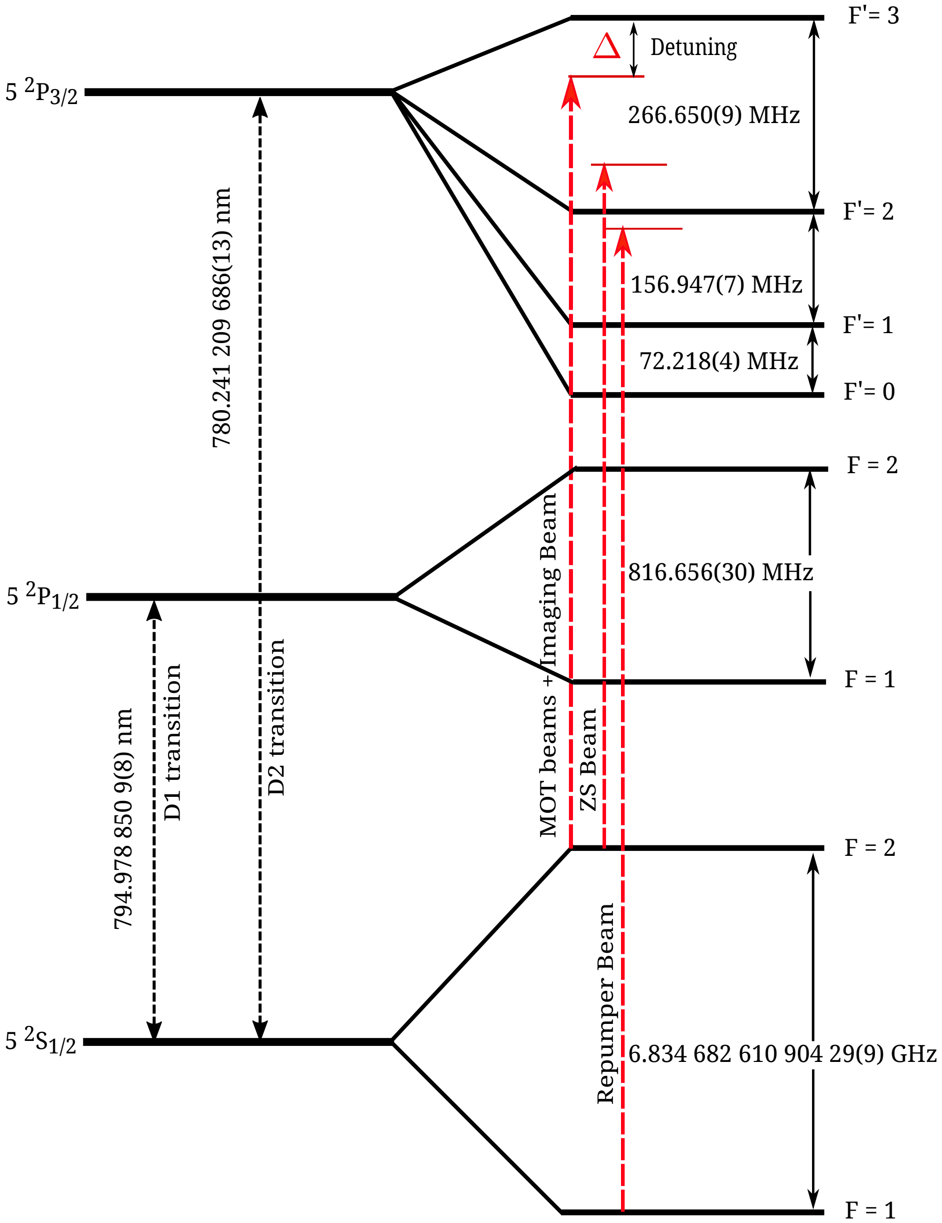
5 $^2P_{3/2}$
5 $^2P_{1/2}$
5 $^2S_{1/2}$
780.241 209 686(13) nm
D2 transition
794.978 850 9(8) nm
D1 transition
F'= 3
Δ
Detuning
266.650(9) MHz
F'= 2
156.947(7) MHz
F'= 1
72.218(4) MHz
F'= 0
F = 2
816.656(30) MHz
F = 1
MOT beams + Imaging Beam
ZS Beam
F = 2
Repumper Beam
6.834 682 610 904 29(9) GHz
F = 1

Figure 4.1: Energy level diagram: Plot shows D1 and D2 transiton of ^{87}Rb. Red dashed lines with arrows shows different transitions involved in cooling and imaging. Our experiment involves transitions between the hyperfine levels of D2 line only. Cooling and imaging of atoms happens on the cyclic transition $|F = 2\rangle \longrightarrow |F^{'} = 3\rangle$. Repumper beam uses $|F = 1\rangle \longrightarrow |F^{'} = 2\rangle$ transition to pump atoms back into $|F = 2\rangle$ (upper hyperfine ground state).

linearly polarised optical beams were derived from this laser using a combination of half wave plate (HWP) and a polarising beam splitter (PBS). Orthogonal polarisation of the beams is used to avoid interference between two optical beams. These beams are prepared from a first-order deflection of Accousto-Optic Modulators (AOM's) which shifts the frequency of each beam by 110 MHz and 120 MHz respectively. AOM's are used for fast switching and to control the power of dipole beams individually. These first order deflections of both the beam are appropriately shaped, collimated and then, focused at the magnetic trap center using a lens of focal length $f = 200$ mm for generating the trapping potential. The complete details of the implementation of cross-dipole trap can be found in Ref. [Sumit's thesis (unpublished)]. In the next section, we describe the experimental sequence used to prepare the BEC.

4.2.1 Experimental Sequence

The experimental sequence is divided primarily into four steps: Loading of Rb atoms in the Magneto-Optical Trap (MOT), Transfer of these atoms from MOT to dipole trap, Evaporative cooling to achieve BEC phase and Detection of the condensate.

During these steps, at various times, the slowing, cooling, trapping and imaging beams along with the magnetic field due to quadrupole coils and camera trigger were turned ON or OFF. This forms the experimental sequence as shown in Fig. 4.2.

Fig. 4.1 shows the low lying energy level diagram of ^{87}Rb. In the experiment, all the transitions that are involved are between the hyperfine levels of D2 line. This D2 line has a natural line width, $\Gamma = 6.065(9)$ MHz. Atoms are cooled on the cyclic transition $|F = 2\rangle \longrightarrow |F^{'} = 3\rangle$ using MOT and Zeeman slower (ZS) beams. During this transition, non resonant excitation can populate $|F^{'} = 2\rangle$ level from this level atoms may decay to $|F = 2\rangle$ or $|F = 1\rangle$ state. Atoms lost to $|F = 1\rangle$ state, comes out of the cyclic cooling transition and can no longer be cooled further. Therefore, a repumper beam tuned from $|F = 1\rangle \longrightarrow |F^{'} = 2\rangle$ level is used which pumps back the atoms from $|5^2S_{1/2}, F = 1\rangle$ level to $|F^{'} = 2\rangle$ level from where atoms can spontaneously decay to $|5^2S_{1/2}, F = 2\rangle$ state, which puts the atoms back into the cyclic transition. Repumber beam is also needed during the imaging, which is described later in the section. Imaging is done using the same cyclic $|F = 2\rangle \longrightarrow |F^{'} = 3\rangle$ transition.

In Fig. 4.2, first, 6 seconds shows the MOT loading phase where atoms are slowed by Zeeman slower and collected in the MOT ($\sim 5 \times 10^7$ atoms). During this phase, the Zeeman slower beam, the six MOT beams, the repumper beam along with the magnetic field of the quadrupole coil (I = 1.3 A) were kept on. Atoms were loaded in the dipole trap directly from the MOT. Therefore, cross dipole beams were turned on from the very beginning of MOT loading. As shown in Fig. 4.2, the power in each dipole beam was ramped up to its maximum ($\sim$ 5.5 W) within the first 1.01 seconds of MOT loading phase and is kept constant at this maximum power until the evaporation phase. During MOT loading, the detuning of the MOT beams ($\Delta \sim 2.6\ \Gamma$ MHz) and repumper beam ($\Delta \sim 1.3\ \Gamma$ MHz) were set quite close to resonance to capture a large no. of atoms in the MOT and to optimise the loading phase. After loading, we turn off the Zeeman slower and hold the atoms in the MOT for 10 ms. For efficient transfer of atoms from the MOT into the dipole trap, atoms were further cooled by decreasing the power and simultaneously increasing the detuning of the MOT beams (from $\Delta \sim 2.6\ \Gamma$ MHz to $\sim 12.6\ \Gamma$ MHz) and repumper (from $\Delta \sim 1.3\ \Gamma$ MHz to $\sim 4.5\ \Gamma$ MHz) in 40.1 ms. Also, the current in the quadrupole coils was slightly increased to compress the cloud (I = 1.85 A). This procedure provides the maximum phase space density ([295]) for trap loading which helps in achieving the condensate later. This is then followed by turning of the repumper beam for 0.8 ms that pumps all the atoms from $5^2S_{1/2}, |F = 2\rangle$ state to $5^2S_{1/2}, |F = 1\rangle$ state of D2 line. This is done to increase the lifetime of atoms in the dipole trap. As atoms in $|F = 2\rangle$ ground state suffer much higher losses due to three body and hyperfine changing collisions than in the $|F = 1\rangle$ ground state.

Once, the atoms are pumped in $|F = 1\rangle$ state, forced evaporative cooling is performed over 7.6 seconds. During the evaporation phase, we reduced the optical power of each dipole beam from 5.5 W to 3.6 mW in five consecutive linear ramps keeping a constant magnetic field ($\mathrm{I}_{\mathrm{helmoltz}} = 1.87$ A) turned on. These five linear ramps form an overall exponential decay of the dipole beam power as shown in Fig. 4.2. By continuously decreasing the power in the dipole beams (the trap depth), hotter atoms from the trap are released which allows remaining atoms in the trap to undergo elastic collisions and thermalise to a lower temperature with higher phase space density, resulting in the formation of Bose-Einstein Condensate (BEC).

We use a standard absorption imaging technique to detect the BEC, where a shadow of atomic cloud is captured on an EMCCD camera (ANDOR) when atoms absorb an on-resonant light. As mentioned earlier, the imaging beam (probe beam) in our setup

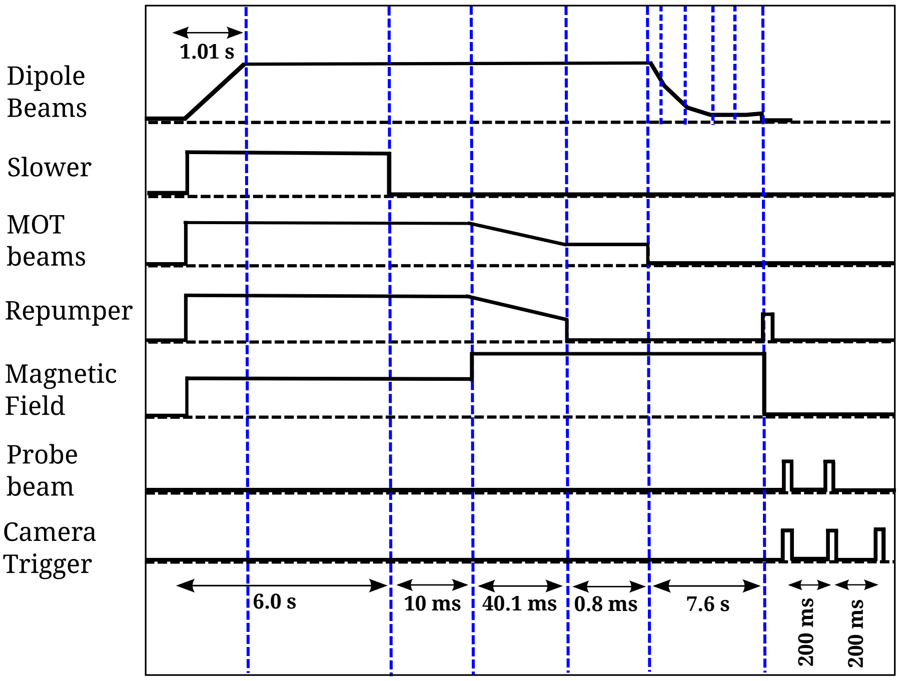
1.01 s
Dipole Beams
Slower
MOT beams
Repumper
Magnetic Field
Probe beam
Camera Trigger
6.0 s
10 ms
40.1 ms
0.8 ms
7.6 s
200 ms
200 ms

Figure 4.2: Experimental sequence: Plot shows the ON and OFF time for different optical and magnetic fields. First, two of the three camera trigger pulses overlap with two probe laser pulses with a wait time of 200 ms between them which depicts the detection scheme.

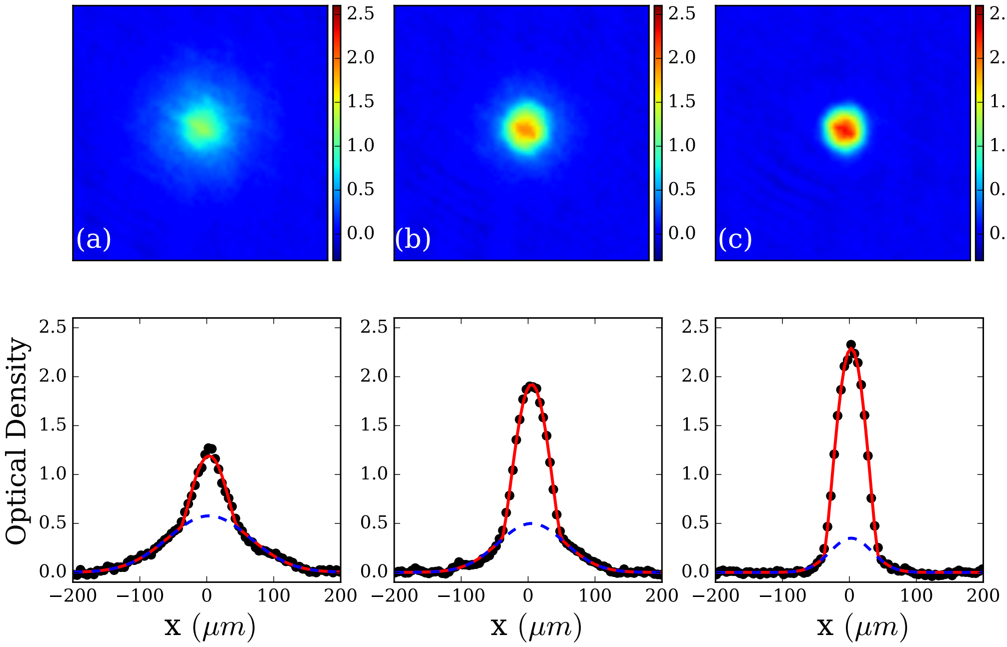

Figure 4.3: Time-of-flight absorption images showing the typical phase transition of the thermal atomic cloud to a BEC phase: Images in panels (a), (b) and (c) shows the integrated optical density of the atoms and the plots below the images show the central 1D cross-section of the corresponding image along the horizontal direction. Solid red lines in 1D plots show fitting to the optical density distribution and dashed blue lines show the contribution from the thermal cloud in each of the images. These images are taken after a 14 ms time-of-flight. (a) Bimodal density distribution showing the onset of phase transition with $N \sim 1.85 \times 10^5$ atoms at a temperature about of 200 nK (final power in each dipole beams is kept $\sim$ 14 mW), (b) with $N \sim 1.3 \times 10^5$ atoms at temperature 130 nK (final power in the dipole beams $\sim$ 6.9 mW) showing the enhancement in the condensate fraction, (c) with $N \sim 7.2 \times 10^4$ atoms at temperature 51 nk, formation of almost pure condensate at final power in the dipole beams $\sim$ 3.6 mW. The field of view of the images is 0.2 mm × 0.2 mm.

is tuned from $|F = 2\rangle \longrightarrow |F^{'} = 3\rangle$ of D2 line which can not be absorbed by condensate as it is prepared in $|F = 1\rangle$ state. Therefore, before imaging the condensate the atoms need to be transferred to $|F = 2\rangle$ state of D2 line which is done by turning on a 60 μs pulse of the repumper beam. The duration of the pulse is kept short enough, so as not to heat the cloud, in addition, the beam is illuminated after turning off the trap to avoid any complexity that may arise from AC stark shift. After turning off the trap and transferring atoms to $|F = 2\rangle$ state, a probe (imaging beam) pulse of 30 μs duration is turned on to irradiate the atomic cloud and simultaneously a trigger pulse is sent to the CCD Camera to record the shadow of the cloud (absorption image).

After a wait time of 200 ms, a second 30 μs probe pulse is turned on. Atomic cloud during this wait time of 200 ms falls under gravity and goes out of the field of view of camera chip which allows capturing only the intensity distribution of probe beam (reference image). After another wait time of 200 ms, the last trigger pulse is sent to the camera to record a frame (background image) where imaging beam and atoms are both absent, and with this one complete experimental sequence ends. These three images are processed further to infer the temperature, size and other properties of condensate which will be described in next Sec. 4.2.2. Fig. 4.3 shows the absorption images of typical phase transition of thermal atoms to BEC as observed in our experiment. As the final optical power in the dipole beams is reduced, a bimodal density distribution starts to appear. This bimodal distribution is the sum of Gaussian and Thomas Fermi distribution representing the thermal atoms and condensate respectively. As the power of the dipole beams is reduced from 14 mW to 3.6 mW, the total number of atoms in the trap reduces while the condensate fraction increases with increasing optical density. In the next section, we describe the detection scheme in detail.

4.2.2 Detection Scheme

As mentioned in the above section, we use absorption imaging method to detect atomic cloud. During each measurement, three frames are recorded: an absorption image, a reference image, and a background image, to estimate the relevant properties of the cloud. Considering the propagation direction of the imaging (probe) beam along the y-axis and using Lambert's Beer Law, intensity distribution $I(x, z)$ of the imaging beam after passing through the atomic cloud can be written as

$$I(x,z) = I_0(x,z)e^{-D(x,z)} \tag{4.1}$$

where $I_0(x,z)$ is the intensity distribution of the imaging beam before the absorption and $D(x,z)$ is the optical density distribution given as $D(x,z) = \sigma_\pi \int n(x,y,z)dy$ where $n(x,y,z)$ is the density of the cloud and σ_π is the photon absorption cross section [1] given as

$$\sigma_\pi = \frac{3\lambda^2}{2\pi} \frac{1}{1+(\frac{2\Delta}{\Gamma})^2} \tag{4.2}$$

λ is the wavelength of the imaging beam, Δ is the frequency detuning with respect to $|F^{'} = 3\rangle$ state.

$$D(x,z) = \ln \left[\frac{(I_{\text{abs}}(x,z) - I_{\text{bg}}(x,z))}{(I_{\text{ref}}(x,z) - I_{\text{bg}}(x,z))} \right] \tag{4.3}$$

Eq. (4.3) is used to estimate the optical density of the atomic cloud using three recorded frames [296], where an absorption image $I_{\text{abs}}(x,z)$, represents the intensity of the imaging beam after passing through the atomic cloud. A reference image, $I_{\text{ref}}(x,z)$ records the intensity distribution of imaging beam without atoms and background image, $I_{\text{bg}}(x,z)$ records the background intensity in the absence of atomic cloud and detection beam.

$$N = \frac{1}{\sigma_\pi M^2} \int D(x,z)dxdz \tag{4.4}$$

Total number of atoms N, can be calculated by integrating the optical density as given in Eq. (4.4), where M is the magnification of the imaging system. A recorded frame is an array of 1000 × 1000 pixels with each pixel of 8 μm × 8 μm size, therefore, integration over the optical density (OD) can be replaced by summation of OD over each pixel. The offset of the image is adjusted to zero before summing over all pixels.

Magnification of the imaging system is found by observing the free fall of the atomic cloud under gravity. After releasing the condensate from the trap, the center position (x,z) of the cloud along gravity (z-direction) over time evolves as

$$z(t) = \frac{a_{\text{g}} t^2/M}{2} + z_0 \tag{4.5}$$

where z_0 is the initial position of the cloud and $a_{\text{g}} = 9.8$ m/s^2 is the acceleration due to gravity. Fig. 4.4 shows the time evolution of the atomic cloud position. Magnification factor of our imaging system is found to be ~ 1.61 by fitting the data with a straight line. Each data point in the plot is obtained by averaging 5 images.

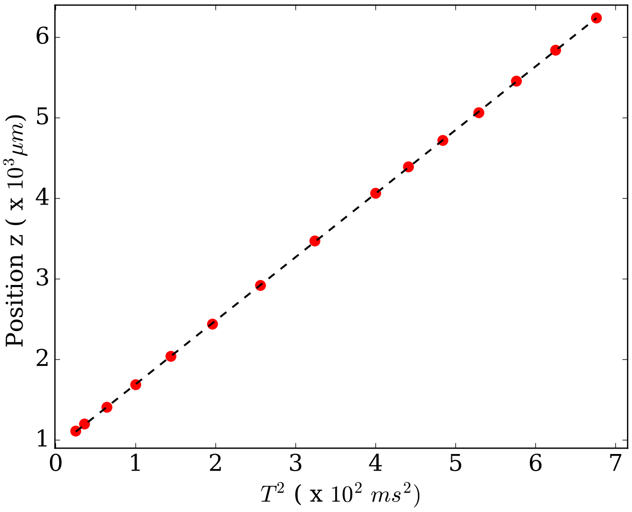

Figure 4.4: Magnification of the imaging system: Plot shows the center position of an atomic cloud falling freely under gravity. Dashed black line shows the linear fit to data. From the slope of the straight line, magnification of our imaging system is estimated as 1.61

4.3 Observation of BEC

In a harmonic trap with trap frequencies ω_x, ω_y, ω_z, the atomic density distribution of the thermal cloud, n_{thermal} and condensate, $n_{\text{condensate}}$ are given as

$$n_{\text{thermal}}(x, y, z) = n_{\text{thermal}}(0, 0, 0)e^{(-\frac{x^2}{\sigma_x^2} - \frac{y^2}{\sigma_y^2} - \frac{z^2}{\sigma_z^2})} \tag{4.6}$$

$$n_{\text{condensate}}(x, y, z) = n_{\text{condensate}}(0, 0, 0)\left[1 - \frac{x^2}{R_x^2} - \frac{y^2}{R_y^2} - \frac{z^2}{R_z^2}\right] \tag{4.7}$$

where R_x, R_y, R_z are the Thomas-Fermi radii of the condensate along x, y and z-direction. After integrating the density distribution along the imaging direction (y-axis), the observed 2D optical density distribution of the condensate, D_{TF} and thermal cloud, D_{thermal} can be written as

$$D_{\text{TF}}(x, z, t) = b_0\left[1 - \frac{x^2}{R_x^2(t)} - \frac{z^2}{R_z^2(t)}\right]^{3/2} \tag{4.8}$$

$$D_{\text{thermal}}(x, z, t) = a_0 \exp\left[-\frac{x^2}{\sigma_x^2(t)} - \frac{z^2}{\sigma_z^2(t)}\right] \tag{4.9}$$

where $a_0 = \sigma_\pi n_{\rm th}(0,0)$ and $b_0 = \sigma_\pi n_{\rm c}(0,0)$ are the peak optical density of the thermal atoms and condensate respectively. The parabolic Thomas Fermi distribution is preserved during the free fall of the cloud while only the aspect ratio of the condensate inverts. For a symmetric trap, the width of the condensate during the expansion evolves as

$$R_i(t) = R_i(0)\sqrt{(1 + (\omega_i t)^2)} \tag{4.10}$$

where i represents the index x, y, z. The temperature of the cloud can be estimated from the width, σ_i of thermal distribution and trapping frequencies as

$$T = \frac{m}{2k_{\rm B}}\left[\frac{{\omega_i}^2}{1 + (\omega_i t)^2}\right]\sigma_i^2(t) \tag{4.11}$$

Fig. 4.3 (a)-(c) shows the transition of atoms from thermal cloud to BEC as the final power of the dipole beam is reduced from 14 mW to 3.6 mW. In the top panel of the figure, absorption images show the optical density, $D(x, z)$ of the cloud recorded after a 14 ms time-of-flight (TOF). The bottom panel shows the corresponding central 1D cross-section along the horizontal direction. These distributions are fitted with a bimodal density distribution (shown by solid red line) which is the sum of thermal $D_{\rm thermal}(x, z)$ (dashed blue line) and Thomas Fermi $D_{\rm TF}(x, z)$ distribution. As we go from fig (a) to (c), reduction in the size (number of atoms) and temperature of cloud while an increase in the condensate fraction can be observed resulting in the condensate of 7.2×10^4 Rb atoms. Here, the temperature of the cloud is estimated using the fitted width of the thermal distribution.

Fig. 4.5 shows the time evolution of aspect ratio of the condensate, i.e. the ratio of the condensate radii along the horizontal and vertical direction. we observed that the aspect ratio of the condensate remains close to ~ 0.9 over time. For a spherically symmetric trap this ratio should be 1. This measurement suggests that our trap is nearly symmetric with a slight difference in the trapping frequencies. In the next section, we estimate the trap frequencies through numerical modelling and experimentally using the method of parametric resonance.

4.4 Trap Frequencies

Trap frequencies are a critical input parameter for numerically simulating the experimental results. In this section, we describe the method to estimate the trap frequen-

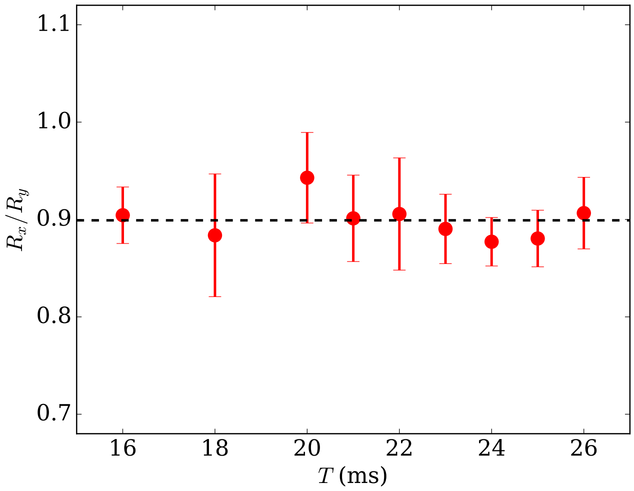

Figure 4.5: Time evolution of the condensate aspect ratio: Plot shows the aspect ratio of BEC to be $\sim 90\%$ with $N = 7 \times 10^4$ atoms

cies by numerically modelling the full trapping potential and experimentally using the method of parametric resonances and evolution of cloud width over time. We also compare the numerically evaluated trap frequencies with the experimental measurements to check consistency.

4.4.1 Numerical Modelling

The full effective trapping potential, U_{Total} is generated by a combination of optical potentials (from the two optical dipole beams), U_{110} and U_{120}, potential due to quadrupole magnetic field, U_{magnetic} and gravitational potential, U_{gravity}

$$U_{\text{Total}} = U_{110} + U_{120} + U_{\text{gravity}} + U_{\text{magnetic}} \tag{4.12}$$

here, 110 and 120 subscripts are used to denote the two dipole beams prepared using 110 MHz and 120 MHz AOM.

$$U_{\text{dip}}(x, y, z) = U_0 I(x, y, z) \tag{4.13}$$

The expression for trapping potential felt by atoms in a far red detuned focused laser beam is given by Eq. (4.13), taken from a detailed review article on optical dipole traps for neutral atoms [112]. Here $U_0 = \frac{3\pi c^2 \Gamma}{2{\omega_0}^3 \delta}$, δ is the detuning of the trapping laser with respect to center of the D1 and D2 transition. $I(x,y,z)$ is the intensity distribution of the far red detuned focused laser beam.

The intensity of a focused elliptic Gaussian laser beam of wavelength λ propagating along y-direction can be written as

$$I(x,y,z) = \frac{2P}{\pi w_x(y) w_z(y)} \exp\left[-2\frac{x^2}{w_x^2(y)} - 2\frac{z^2}{w_z^2(y)}\right] \tag{4.14}$$

Beam waists (where the intensity of beam falls to $1/e^2$ of maximum), $w_x(y)$ and $w_z(y)$ depend on y-coordinate and as

$$w_x(y) = w_{x0}\sqrt{1 + (y/zr_x)^2} \tag{4.15}$$

$$w_z(y) = w_{z0}\sqrt{1 + (y/zr_z)^2} \tag{4.16}$$

where $zr_x = \frac{\pi {w_{x0}}^2}{\lambda}$, $zr_y = \frac{\pi {w_{z0}}^2}{\lambda}$ are the corresponding Rayleigh range, decided by the waist.

To estimate the trap frequency, optical dipole potential formed by a focused Gaussian beam is approximated with a Taylor series since the kinetic energy of atoms is much less than the trap depth. By truncating the Taylor expansion up to second order terms near the minima, the shape of the trap approximates a harmonic potential. The trap frequencies along the three principal axes, defined by the beam propagation axis along with other two perpendicular directions can be estimated directly from the coefficient of the second order term (as the trap is approximated with harmonic potential) in the expansion. However, this Taylor expansion method may not give the correct estimate of the trapping frequency if the propagation axis of the two cross dipole beams are not perpendicular to each other. Also, in case of low power in the dipole beams where the contribution from gravitational and magnetic fields cannot be ignored. In our case, two dipole beams form an angle of 30° and −25° with respect to imaging axis. At the same time, the effects of gravity and the magnetic field need to be taken into account due to low powers at the end in dipole beams. We write the full potential and look at the x, y, z cross-section near the trap minima to estimate the trap frequencies. Fig. 4.6 shows the orientation of 1064 nm optical dipole beams (red arrows) in the x-y plane with respect to the imaging axis (y-direction). These dipole beams are named as 120

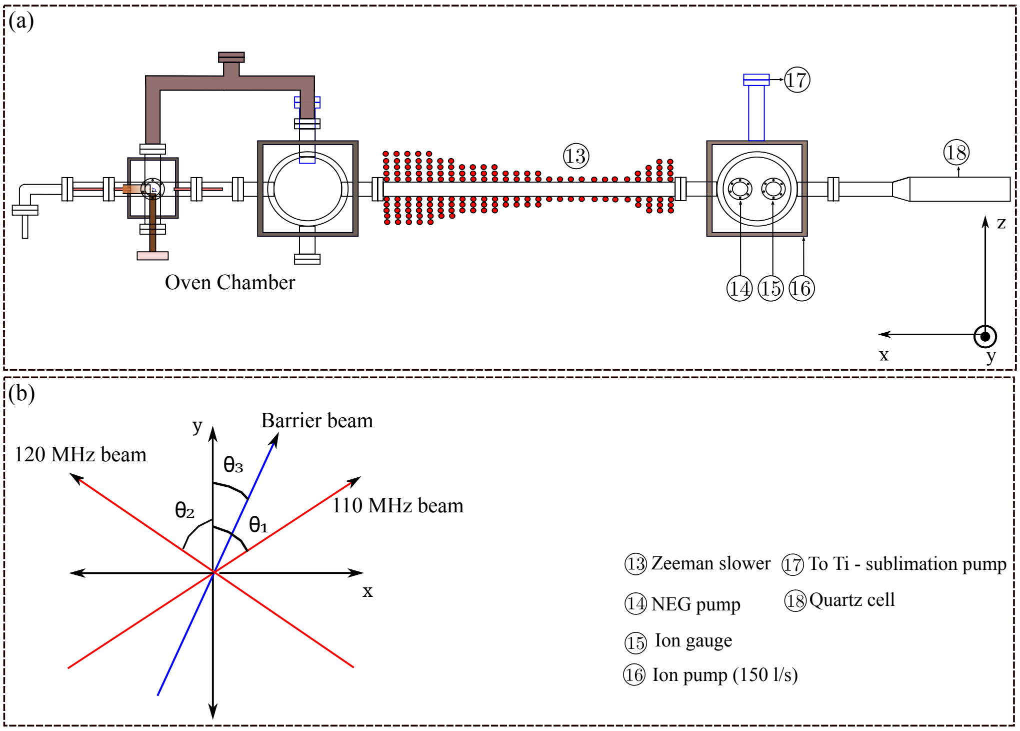
(a)
⑰
⑬
⑱
z
Oven Chamber
⑭ ⑮ ⑯
x
y
(b)
y
Barrier beam
120 MHz beam
θ3
θ2
θ1
110 MHz beam
x
⑬ Zeeman slower
⑰ To Ti - sublimation pump
⑭ NEG pump
⑱ Quartz cell
⑮ Ion gauge
⑯ Ion pump (150 l/s)

Figure 4.6: Orientation of optical dipole and barrier beam in the experimental setup: (a) Schematic: Side view of experimental setup [1]. (b) Schematic showing orientation of red detuned dipole beam and the blue detuned barrier beam with respect to imaging axis (y-direction). 110 MHz beam makes an angle $\theta_1 \sim -25°$ and 120 MHz beam makes an angle $\theta_2 \sim 30°$. The optical barrier beam is oriented at $\theta_3 \sim 10°$.

MHz beam, and 110 MHz beams as the beams are derived from two different AOMs with the corresponding frequency shifts of 110 and 120 MHz respectively.

The optical potential due to these two beam can be written as

$$U_{110} = \frac{2P_1U_0}{\pi w_{z1}(y')w_{x1}(y')} \exp\left[-2\frac{x'^2}{{w_{x1}}^2(y')} - 2\frac{z^2}{{w_{z1}}^2(y')}\right] \tag{4.17}$$

$$U_{120} = \frac{2P_2U_0}{\pi w_{z2}(y')w_{x2}(y')} \exp\left[-2\frac{x'^2}{{w_{x2}}^2(y')} - 2\frac{z^2}{{w_{z2}}^2(y')}\right] \tag{4.18}$$

where $x' = x\cos\theta + y\sin\theta$, $y' = y\cos\theta - x\sin\theta$. P_1, P_2 denotes the power in each dipole beam and w_x and w_z are the corresponding beam waists along x and z direction. Dipole beam is prepared by focusing a collimated beam through a lens of focal length 200 mm. Diameter of both beam at the focusing lens is measured as $D_x = 4.3$ mm and $D_z = 5$ mm. Both the beams have nearly same size and end power. Beam waist are related to the measured diameter (D_x, D_z) as $w_x = \frac{4\lambda_L f}{2\pi D_x}$, $w_z = \frac{4\lambda_L f}{2\pi D_z}$. The contribution from the linearly varying gravitational potential can be written as

$$U_{\text{gravity}} = m a_{\text{g}} z \tag{4.19}$$

where $m = 1.443 \times 10^{-25}$ Kg is the mass of the ^{87}Rb atom, $a_{\text{g}} = 9.8$ m/s^2 is the acceleration due to gravity. Gravitational potential at low powers makes the trap anharmonic. To lift the trap depth against gravity, a low quadrupole field is kept on. The potential felt by atoms in $|5^2S_{1/2}, F = 1\rangle$ ground state due to the magnetic field can be written as

$$U_{\text{magnetic}} = \frac{1}{2}\mu_{\text{B}}\frac{dB}{dz}\sqrt{z^2 + \frac{1}{4}(x^2 + y^2)} \tag{4.20}$$

where $\mu_{\text{B}} = 9.27 \times 10^{-24}$ J/T and dB/dz is the axial magnetic field gradient (1300 Gm^{-1} per unit ampere current). We use 1.87 ampere current in the quadrupole coils to form the trap.

Total effective trapping potential U_{Total}, is numerically computed. Cross sections along x, y, z directions passing through the trap minima as shown in Fig. 4.7(b). The profiles are extracted from the numerically generated potential. We can see due to gravity the potential minima along z axis is shifted below the center of trapping beams. Fig. 4.7(a) shows a second order polynomial,$f(x) = p_1(x - x0)^2 + p_0$ fit to these cross sections near the trap minima. where p_1 and p_0 are the fitting parameter. Using fitting parameter, trap frequency along each direction can be estimated as $\nu = \frac{1}{2\pi m^2}\sqrt{2p_1k_{\text{B}}}$.

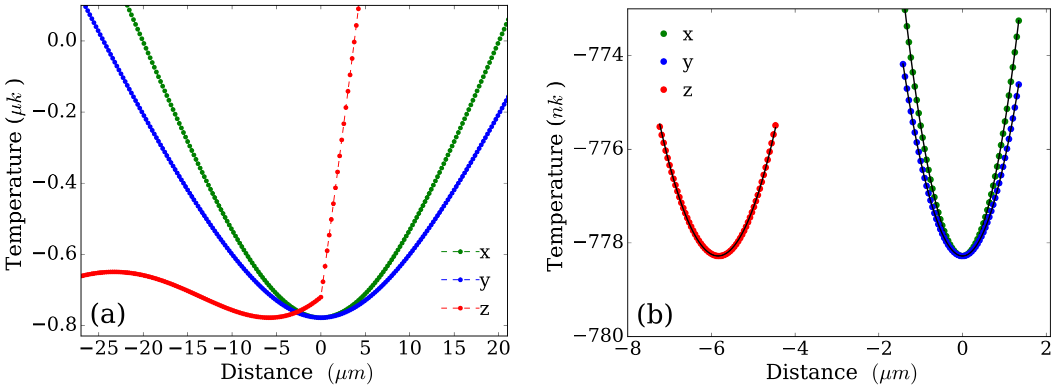

Figure 4.7: Modelling of the total trapping potential: (a) Cross sections along x, y, z direction of the numerically simulated trapping potential (U_{Total}) across the trap minima at $P = 3.6$ mW. (b) Shows the second order polynomial fit (solid black lines) to the cross sections near the trap minima. from the fit, trap frequencies are estimated to be $\nu_{\mathrm{x}} = 116$ Hz , $\nu_{\mathrm{y}} = 99$ Hz , $\nu_{\mathrm{z}} = 83$ Hz

.

Trap frequencies along three different directions were found as $\nu_x = 116$ Hz, $\nu_y = 99$ Hz, $\nu_{\mathrm{z}} = 83$ Hz. In the figure, for convenience potential energy is converted into temperature equivalent by dividing the potential energy with the Boltzmann constant k_{B}.

4.4.2 Experimental Measurement

After numerically estimating the trap frequencies which showed a 70-80 % trap symmetry, we measured the trap frequencies using the method of parametric heating [297, 298]. As the mode volume of our trap was small, the usual method of observing the center of mass motion of the atomic cloud to measure the trap frequency could not be implemented in our setup. This method is typically adopted in the case of magnetic traps (large mode volume). In the parametric heating method, trap depth is modulated sinusoidally by modulating the power of one of the trapping beams. In our setup, we modulate the power of beam passing through 110 MHz AOM. When modulation frequency ω_{m} approaches close to the harmonics of the unperturbed trap frequency (ω_0) as given by Eq. (4.21), energy is transferred to the atoms. Optical potential has a finite trap depth which is not able to hold the atoms with extra acquired energy and this results in heating and significant loss of atoms from the trap.

$$\omega_{\mathrm{m}} = \frac{2\omega_0}{n} \tag{4.21}$$

where $n = 1, 2, 3...$

For a parametrically driven oscillator the equation of motion can be written as

$$\ddot{x} + \beta(t)\dot{x} + \omega(t)^2 x = 0 \tag{4.22}$$

with trap frequency $\omega(t)$, damping coefficient $\beta(t)$ where time dependent trap frequency, $\omega(t)$ can be written as is give as

$$\omega(t)^2 = \omega_0^2 \left[1 + \epsilon \sin(\omega_{\mathrm{m}} t)\right] \tag{4.23}$$

here, ϵ is the modulation amplitude, ω_{m} is the modulation frequency and ω_0 is the unperturbed trap frequency. These parametrically driven system exhibits resonances given by Eq. (4.21). When resonance condition is satisfied, the energy of the system grows exponentially resulting in loss of atoms from the trap.

The widths of these resonances vary as $\epsilon^n \omega_0$ and also the frequency difference between subsequent resonances reduces as we move towards the higher harmonics which usually allows one to observe only first two resonances in the experiment. Trap frequency scales with the power of the dipole beams as $\nu \propto \sqrt{P}$. We measure parametric resonances at three different end powers of the dipole beams to make sure that we observed the correct first two resonances of the trap. For 3.6 mW power in the dipole beams, we modulated the trap depth by 20%. We had to increase this modulation depth up to 40% to observe the significant loss (resonances) at higher power in the dipole beams. At 3.6 mW end power in both the dipole beams, we keep the modulation on for about 45 ms then, after turning off the modulation, we hold the atoms in the trap for ~150 ms to thermalise. The atomic cloud is imaged after time-of-flight of 14 ms to estimate the total number of atoms left in the trap. We repeat this measurement for different modulation frequency to generate Fig. 4.8(a) which shows the number of atoms in the trap for different modulation frequencies. As the modulation frequency is swept from 0 to 400 Hz, a significant loss in atoms number near 83 Hz (ω_0) and 180 Hz ($\sim 2\omega_0$) is observed. These two resonances closely follow the resonance condition. Here we observe a single peak at ω_0 which suggest the three trapping frequencies would be

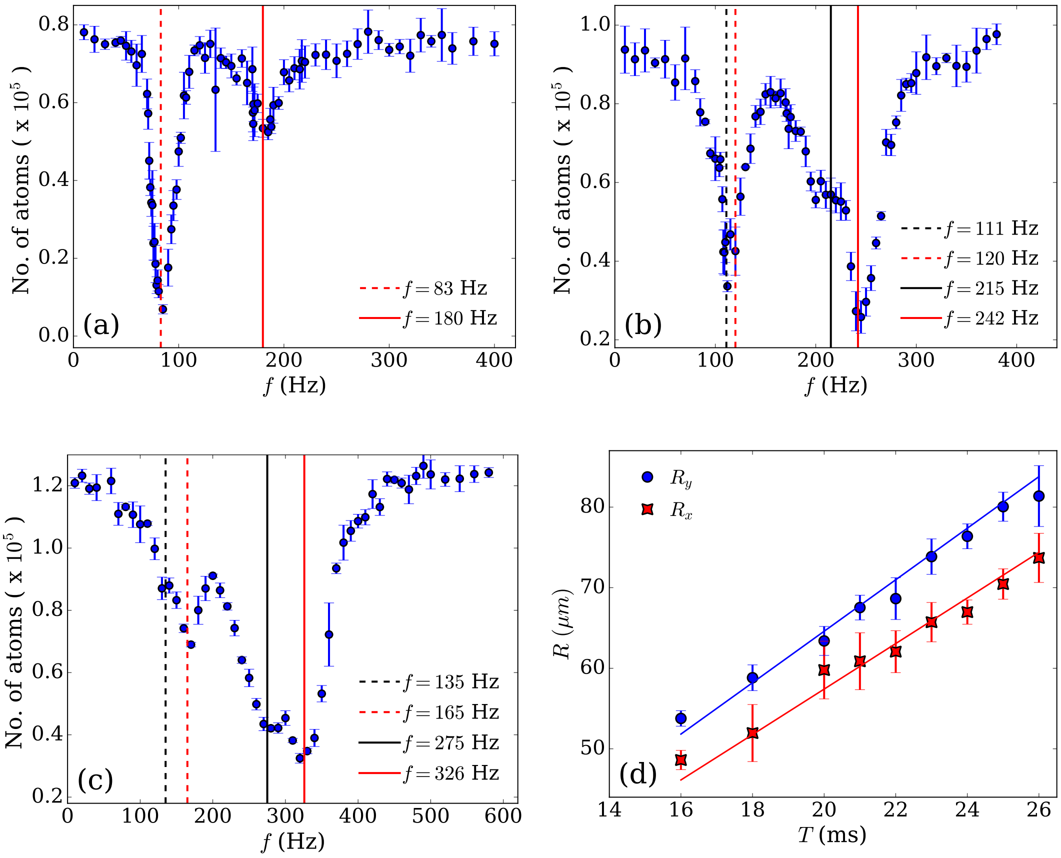

Figure 4.8: Trap frequency measurement using parametric heating method: (a), (b), (c) shows parametric resonances at different end power of the dipole trap where solid and dashed red line represents the first (2ν) and second (ν) harmonic of the trap frequency respectively while black and red color of line shows non degenerate frequencies of the trap. (a) Resonances at P $\sim$ 3.6 mW power in dipole beam, (b) P $\sim$ 7.2 mW, (c) P $\sim$ 14.4 mW. All Resonances are found to be in agreement with $\nu \propto \sqrt{P}$ scaling. (d) shows the time evolution of Thomas-Fermi radius of condensate. The solid line shows the fitted profile. Trap frequency from the fit found to be $\nu_x \sim$ 62 Hz and $\nu_y \sim$76 Hz.

nearly the same. This supports our earlier observations about the aspect ratio of cloud which was found to be nearly ~ 90 %

By increasing the power of the dipole beams, we expected to observe the shift in the position of these two resonances accordingly. Therefore we increased the end powers of the dipole beam to ~ 7 mW. Here, modulation was kept on for 90 ms followed by a hold time of 300 ms. Detection was done after a time of flight of 14 ms. Fig. 4.8(b) shows the corresponding plot with a shift in resonance position. Resonances start to resolve at higher power. The dashed line in the plot represents the second harmonic (ω_0, when $n = 2$) and the solid line represents the position of first harmonic ($2\omega_0$, when $n = 1$). As we doubled the power of dipole beams, we expected the shift in frequency by a factor of $\sqrt{2}$. It can be seen from the plot this scaling and resonance condition is satisfied very well. We also notice the resonances become broader at higher trap depth and loss is more at the first harmonic. Another measurement was taken at 14 mW power (dipole beams) where modulation was kept on for 90 ms followed by a hold time of 300 ms. Detection was done after an 8 ms time of flight as shown in Fig. 4.8(c). Here also, first two resonances scales in accordance with the increase in power of the dipole beams. The difference in the trap frequencies starts to appear. Here a low time-of-flight was used since, at such powers of the dipole beams, we have a thermal cloud in the trap which then expands quickly after the trap is switched off and reduces the signal to noise ratio at longer times.

In addition to parametric resonances, evolution of cloud width over time can be used to get an estimate of the trap frequencies as shown in Fig. 4.8(d). Thomas-Fermi radius of the cloud for a nearly symmetric trap scales as $R_i = R_{0,i}\sqrt{1 + (\omega_i t)^2}$ where $R_0 = \sqrt{\frac{2\hbar\mu}{m\omega}}$, $\mu = \frac{\hbar\omega}{2}\left(\frac{15g}{4\pi}\right)^{2/5}$, $g = \frac{4\pi\hbar^2 aN}{m}$. Assuming a spherically symmetric trap, We fit the evolution of cloud width, keeping trap frequency as the only fitting parameter. We found the trap frequencies to be ~ 62 Hz and ~ 76 Hz along horizontal and vertical direction suggesting a trap symmetry of 80 %.

We compare all the above measurement of trap frequencies and found that numerical modelling of the trap overestimates the trap frequencies compared to the experimental measurements. This could be attributed to the errors in the input parameter for the model such as the angle between the dipole beams, powers in the dipole beam, beam waist at the focus etc. Although the difference in the estimated trap frequencies from two experimental methods is not significant. The small deviation in trap frequencies measurement from parametric resonances and evolution of cloud width can be attributed to the assumption of a nearly symmetric trap and the input parameter used during fitting (number of atoms). For numerically simulating the dynamics of condensate in the linear regime, we used a spherical symmetric trap with trap frequency 80 Hz and the atomic cloud with 6×10^4 atoms. In the next section, we describe an experiment conducted to probe the linear regime of the condensate.

4.5 Bouncing BEC Experiment

We probe the condensate in linear regime by the "Bouncing BEC" experiment. We release the condensate from the trap, let it expand and fall freely under gravity. Due to expansion, the density of the condensate decreases resulting in negligible atom-atom interactions which sets the condensate in the linear regime. In this section, we discuss the setup, observations and results of the experiment. Towards the end of this section, we describe the efforts to numerically model the experimental observations.

4.5.1 Experimental Setup: Bouncing BEC

In the experiment, we released the condensate from the trap and let it fall freely under gravity on a Gaussian optical barrier. This barrier is formed by a focussed blue detuned laser beam and placed ~ 100 μm below the trap center. Barrier beam propagates at an angle of $\sim 10°$ with respect to imaging axis as shown in Fig. 4.6.

Barrier beam is prepared on a different optical table than the main optical table (BEC experiment). The beam is transported to the main experimental optical table through a polarization maintaining single mode fiber with FC-APC connector at both ends (60 FC series from Shäfter + Kirchoff). Fig. 4.9 shows the optical arrangement of the setup used to prepare barrier beam. A tunable diode laser (Toptica, DLPro) is used to generate the barrier beam with a wavelength range of 765-795 nm. A combination of HWP and PBS splits the beam into two parts (reflected and transmitted). The reflected beam is sent to wavemeter to monitor the wavelength, and the transmitted part is used to prepare the barrier. This beam size is reduced using a 4:1 telescope, formed by a combination of two lenses (f = 100 mm and f = 25 mm) and passed through an AOM (ATM - 801A2) to get maximum coupling efficiency in the first-order deflection. AOM is used for controlling the power (height of the barrier) and fast on-off switching

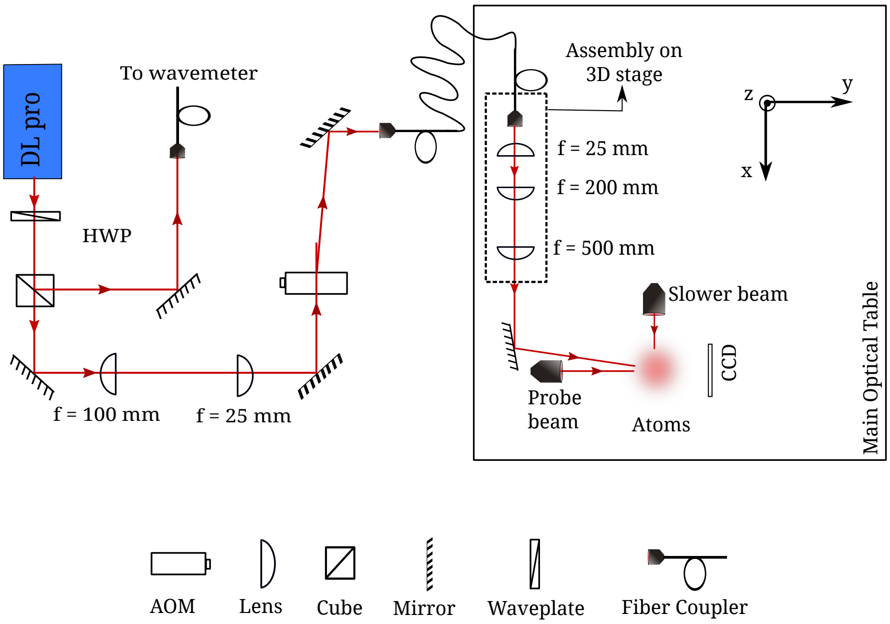
DL pro
To wavemeter
HWP
f = 100 mm
f = 25 mm
Assembly on
3D stage
f = 25 mm
f = 200 mm
f = 500 mm
z
y
x
Slower beam
CCD
Probe
beam
Atoms
Main Optical Table
AOM
Lens
Cube
Mirror
Waveplate
Fiber Coupler

Figure 4.9: Optical layout for barrier beam preparation

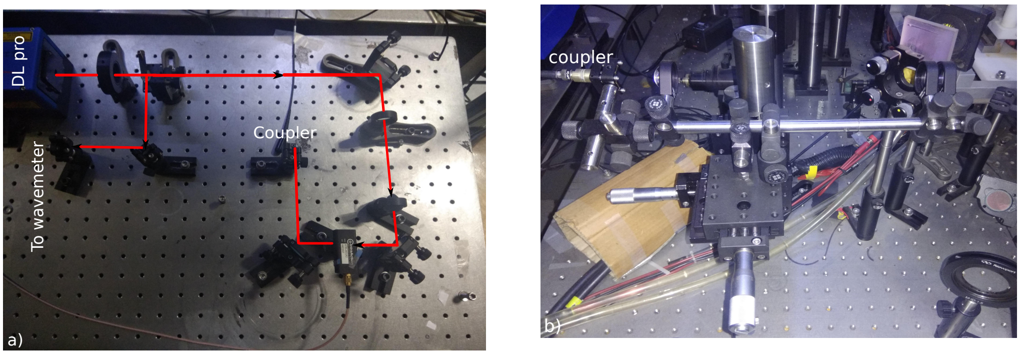
DL pro
To wavemeter
Coupler
a)
coupler
b)

Figure 4.10: Image showing the setup to generate optical barrier: (a) Beam prepared on a separate optical table using a tunable DLpro laser diode. The output of this laser diode is split into two beams. one of the beams is transported to the main optical table and another beam is sent to wavemeter for monitoring the wavelength of the beam. (b) Shows the assembly of fiber coupler and three lenses, mounted on 3D stage to align the beam with respect to atomic cloud

.

of the beam. This first order deflection of the AOM is coupled into the fiber using a collimator which transports the beam to the main optical table (BEC experiment). On the main optical table, fiber output is collimated using another collimator and passed through a 1:8 telescope formed by two 1" diameter lenses of focal length $f = 25$ mm and $f = 200$ mm. This lens combination expands the beam and generates a collimated beam of diameter ~ 1 cm. This collimated beam is focused at the trap center using a final 1" diameter lens of focal length $f = 500$ mm. A mirror is used in between to direct the beam towards the condensate. To align the beam with respect to the atomic cloud along x, y, z-direction, the whole assembly consisting of the collimator and the last three lenses, are mounted on a 3D translating stage. Fig. 4.10 shows the photographs of the beam preparation setup. Fig. 4.10(a) shows the coupling of the first-order deflection to the collimator and the Fig. 4.10(b), shows the 3D stage to steer the barrier beam.

4.5.2 Experimental Results

We measure the beam waist of the barrier at the focus to be 30 μm using the knife-edge method. The alignment of the beam is done in two steps. First, we make the coarse adjustment during the continuous loading of the MOT where atoms are held in the $|F = 2\rangle$ ground state of D2 line. We tune the wavelength of the barrier beam to resonance ($|F = 2\rangle \longrightarrow |F' = 3\rangle$), such that when the atoms come in contact with the beam, light is absorbed and atoms are heated, reducing the atom number in MOT. This effect can be observed on the MOT by blocking and unblocking the barrier beam. To improve the alignment, we reduce the MOT size by increasing the detuning of the MOT beam and current in the quadrupole coil.

In the second step, we align the barrier beam to the centre of the dipole trap by looking at the absorption images. Size of the cloud in MOT is much larger than the barrier beam, and the presence of the barrier beam in the absorption images can be seen by a dip in the optical density of the cloud. We keep on reducing the size of the atomic cloud by adjusting the end power of the dipole beams in the evaporation phase and scan the barrier beam to reduce the optical density of the cloud. Once this is optimized, OD is minimized by reducing the power and duration of the barrier beam. To finally align the focus of the beam, we red detuned the barrier beam such that intensity maxima of the beam act like a potential well for the atoms. The focus is aligned by capturing the condensate in this potential well and maximizing the OD.

Once the alignment was done, we tuned the frequency of the barrier beam to 384.76553 THz which made the barrier 25.7 THz blue detuned with respect to the center of D1 and D2 line during the experiment. Barrier beam was displaced vertically down by $\sim 100\ \mu$m below the trap center. The wavelength of the DLpro laser was not locked, and we observed a shift of 10-20 MHz in the frequency of barrier beam over the duration of the experiment. Barrier beam is turned off just after releasing the condensate from the trap and kept on all the time until the detection. Fig. 4.11 shows a sequence of absorption images and corresponding 1D cross-section along the vertical direction for a BEC hitting the optical barrier with power 12.5 mW. Here the power of the barrier beam was measured at the output of collimator placed on 3D stage.

Fig. 4.12 shows the images after the first reflection of BEC from the barrier. Our barrier acts like a Gaussian hill for the incoming atoms instead of a flat sheet. Therefore, BEC acquires an arc shape during the first reflection as the atoms at the periphery penetrates well within the Gaussian hill whereas the atoms at the centre start to move upward. As cloud moves upwards, splitting of the condensate wave packet along vertical direction can be observed which is similar to the one reported in [294]. This splitting feature enhances as condensate travel upwards towards the initial altitude and disappears when it starts to fall back. Fig. 4.13 shows the further evolution of condensate where condensate begins to revert and splitting feature starts to disappear. Fig. 4.14 shows the second reflection of the condensate from the barrier at 14.41 ms. The condensate size at this point along the horizontal direction becomes much larger compared to the size of the barrier. Therefore a central part of the condensate is reflected to form a bulge in the atomic density whereas atoms in the side arms continue to fall downwards.

Fig. 4.15 shows fringe pattern emerging from the interference between the upward moving reflected wave packet and the falling side arms of the condensate. These fringes are observed near the edges of the bulge only and not extended to the side arms. We also encounter some fringes in the central part of the reflected cloud, which is attributed to the deformed beam profile of the barrier. A small misalignment of the barrier beam (10 μm) with respect to condensate can give an overall tilt to the reflected wave packet which is responsible for the formation of the fringes in one side of the arc only. To

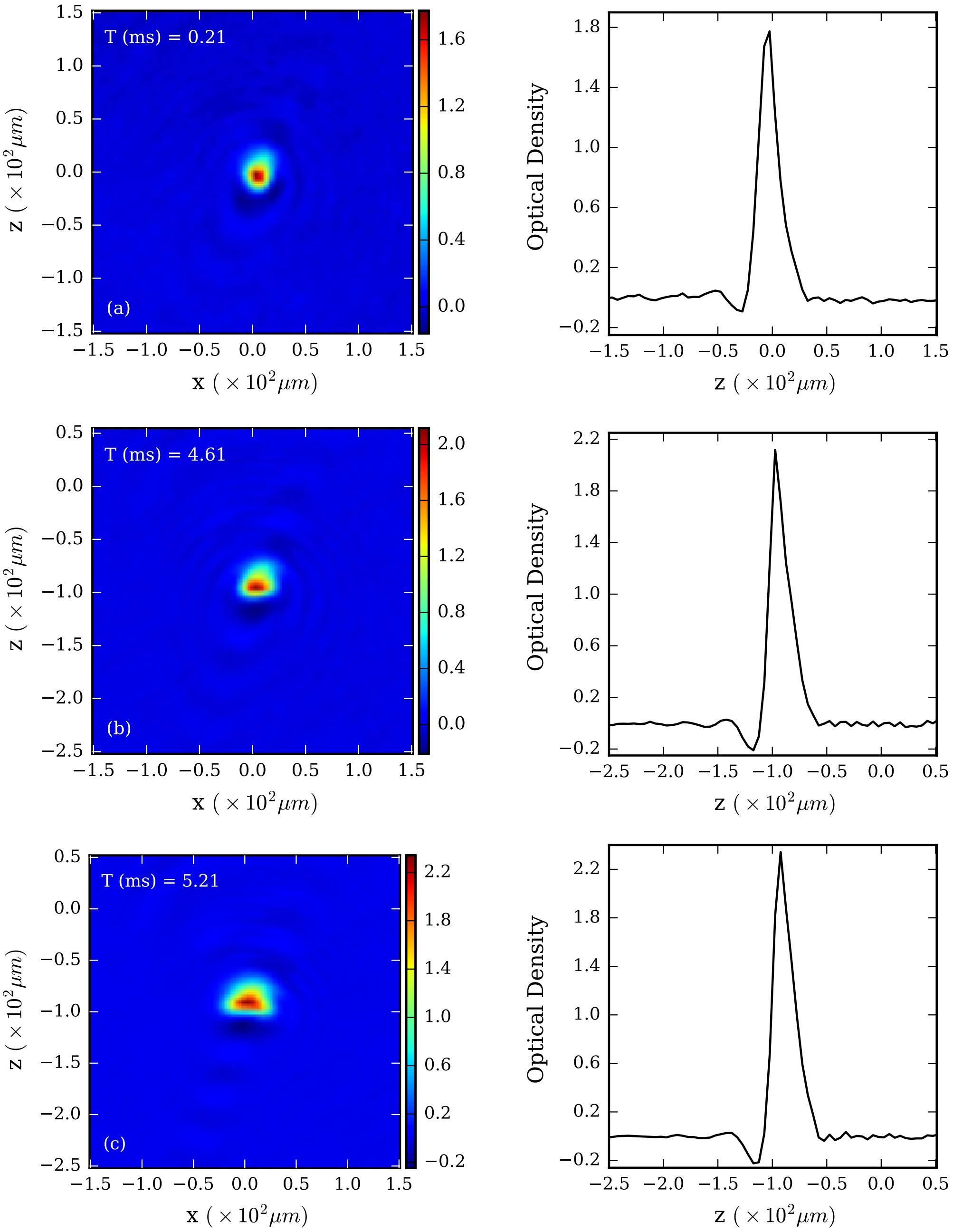

Figure 4.11: Bouncing dynamics of BEC from a Gaussian barrier: Left panel: shows absorption images of free fall evolution of BEC in the presence of optical barrier with 12.5 mW of optical power, beam waist, $w_{\text{barrier}} \sim 30\ \mu$m at frequency, $\omega_{\text{barrier}} = 384.76553$ THz. Barrier beam is placed $\sim 100\ \mu$m below the in-trap condensate position. Right panel: shows 1D vertical cross-section of the center of the condensate. (a) Shows the initial condensate after a TOF of 0.21 ms (b) Shows the first hit at the barrier after a TOF of 4.61 ms (c) Shows the squeezing of the condensate along the vertical direction where it interacts with the barrier for about 0.6 ms before reverting

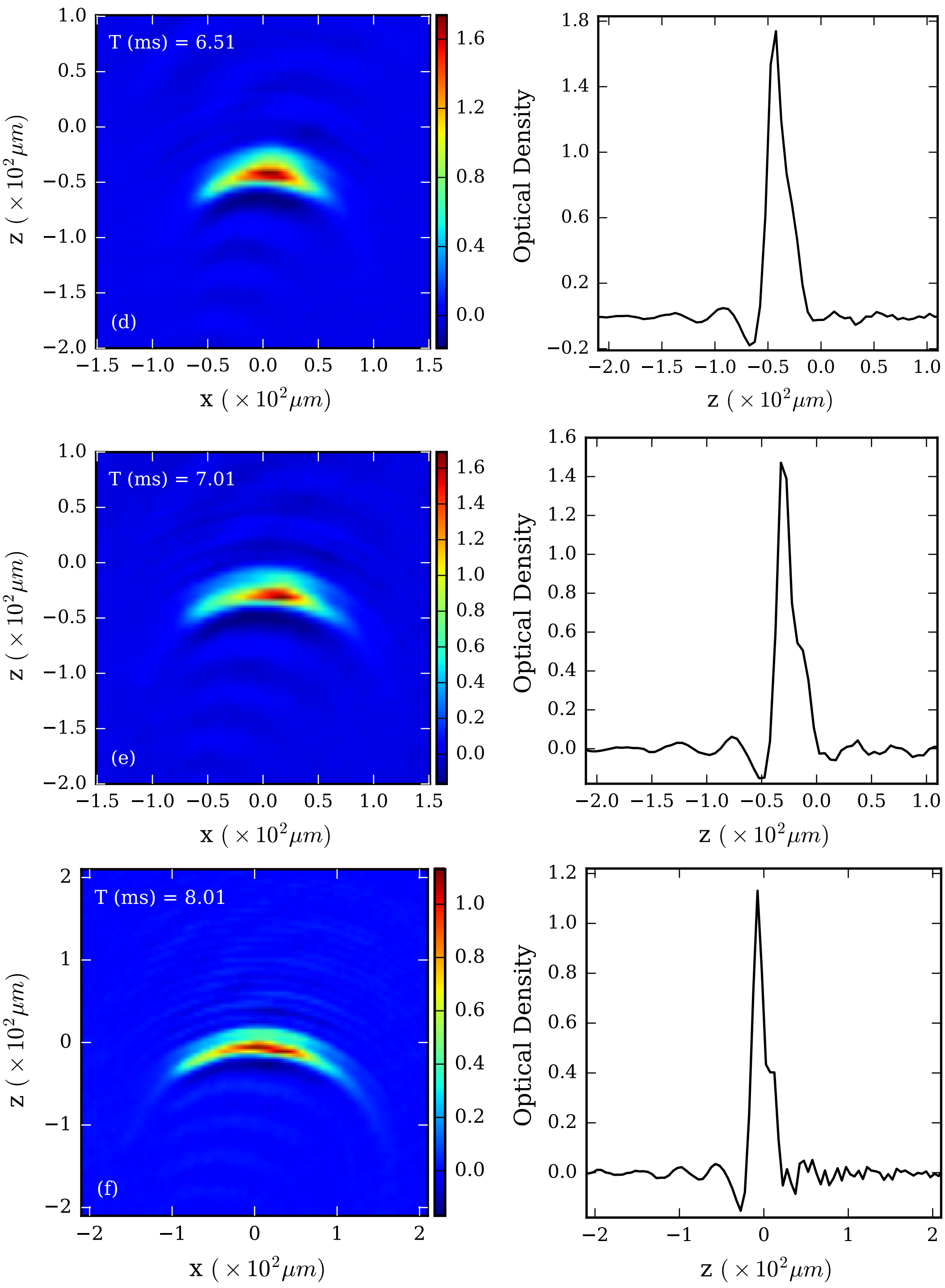

Figure 4.12: Free fall evolution of BEC in the presence of barrier continues: (d) Condensate moving upward, starts to develop double peak structure along the z axis (e) Double peak feature enhances (f) Wave packet continues to squeeze along the vertical direction and optical density of the condensate decreases due to quick expansion along the x direction

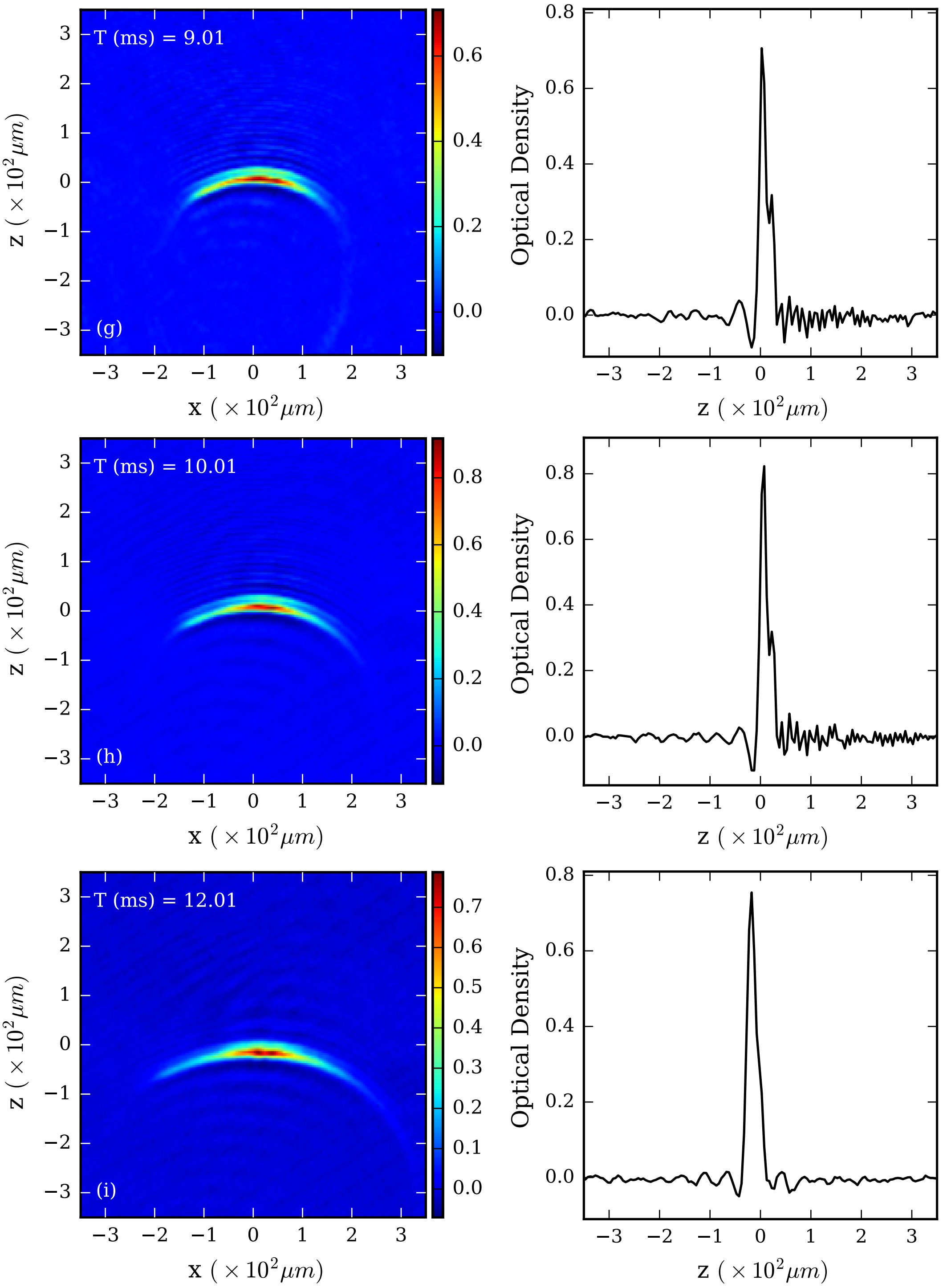

Figure 4.13: Further free fall evolution of BEC in the presence of barrier: (g) Splitting of the condensate along vertical direction becomes prominent (h) Condensate reaches the initial height and after this point, it starts to come downwards again where the vertical split of the condensate starts to merge (i) Splitting feature has disappeared

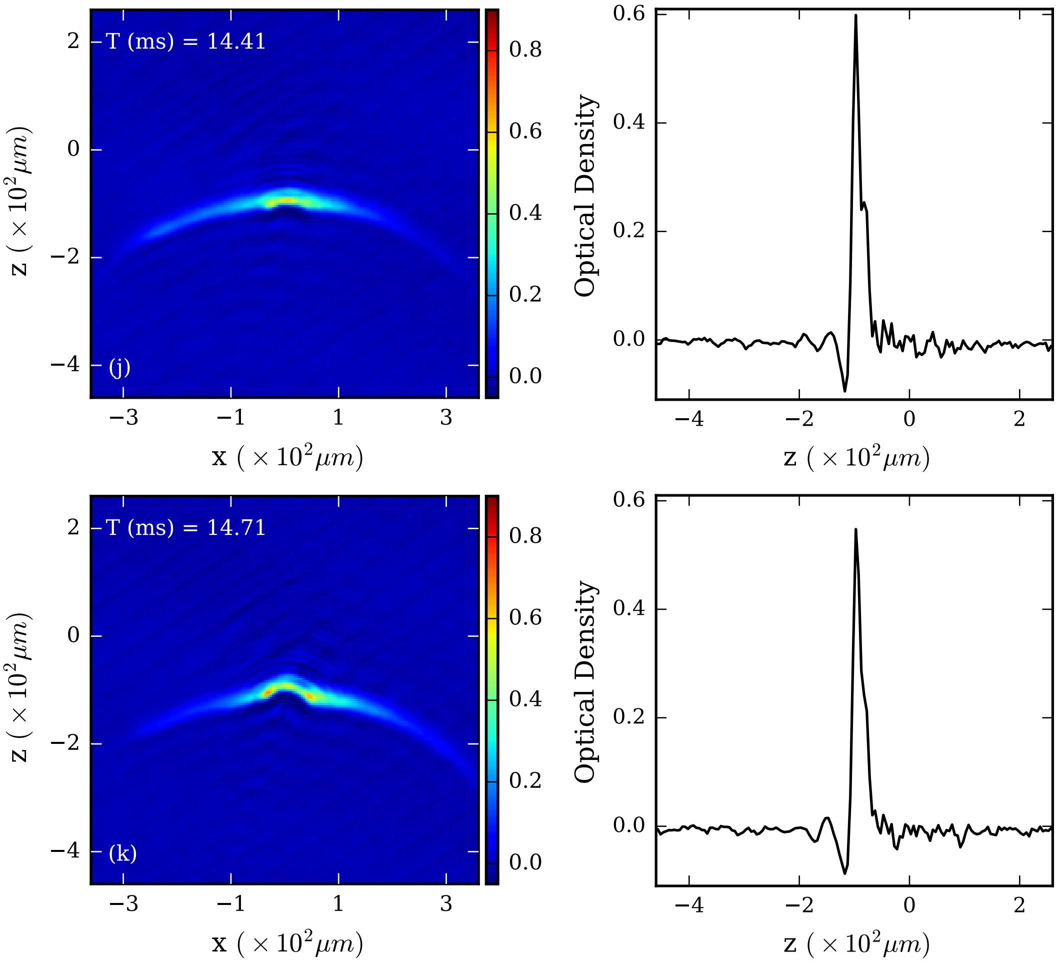

Figure 4.14: Continuation of free fall evolution of BEC in the presence of the barrier: (j) Second hit of the condensate at the barrier. The extent of the condensate along horizontal direction becomes much larger than the barrier (k) Central part of the condensate interacts with the barrier and reflected back while rest of the condensate continues to fall downwards

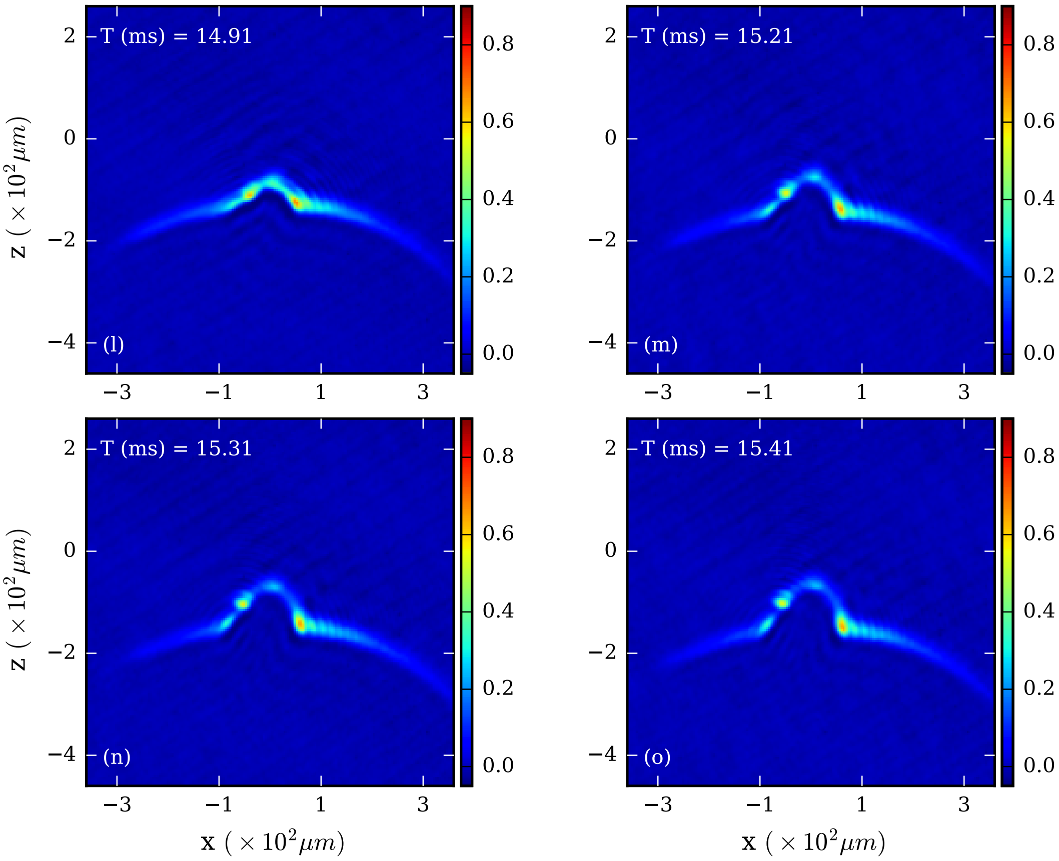

Figure 4.15: Evolution of the secondary reflection from barrier continues: (l) Interference fringes starts to appear at the corners of outer arms of the condensate (m) A deformation of barrier beam profile has lead to the formation of the fringes in the top reflected part (n) Contrast of the fringe pattern enhances. Misalignment of the barrier (∼ 10 μm) with respect to centre of the condensate causes an overall tilt with respect to the vertical axis (asymmetry) in the reflection which causes fringes to appear only on one side of the arm

.

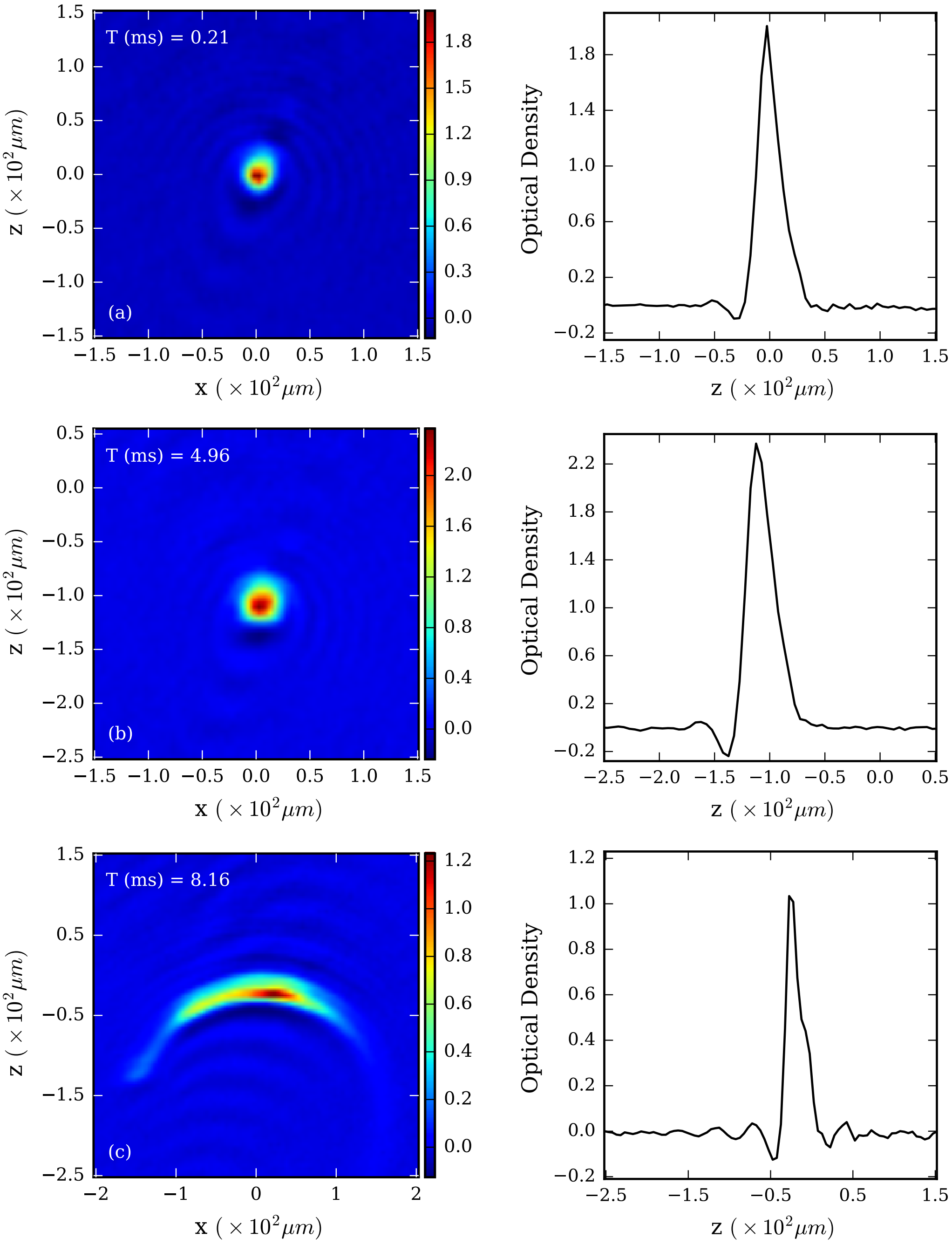

Figure 4.16: Bouncing dynamics of BEC from a Gaussian barrier: Left Panel: Absorption images of freely falling BEC in the presence of barrier placed ~ 130 μm below the trap center. Power and detuning of the barrier beam kept unaltered. Right panel: shows the corresponding 1D vertical cross section of the images through the center of cloud (a) Condensate after a TOF of 0.21 ms (b) First hit at the barrier, wave packet shrinks along the vertical direction and subsequent increment in the OD is observed (c) Reflected wave packet starts to develop splitting feature

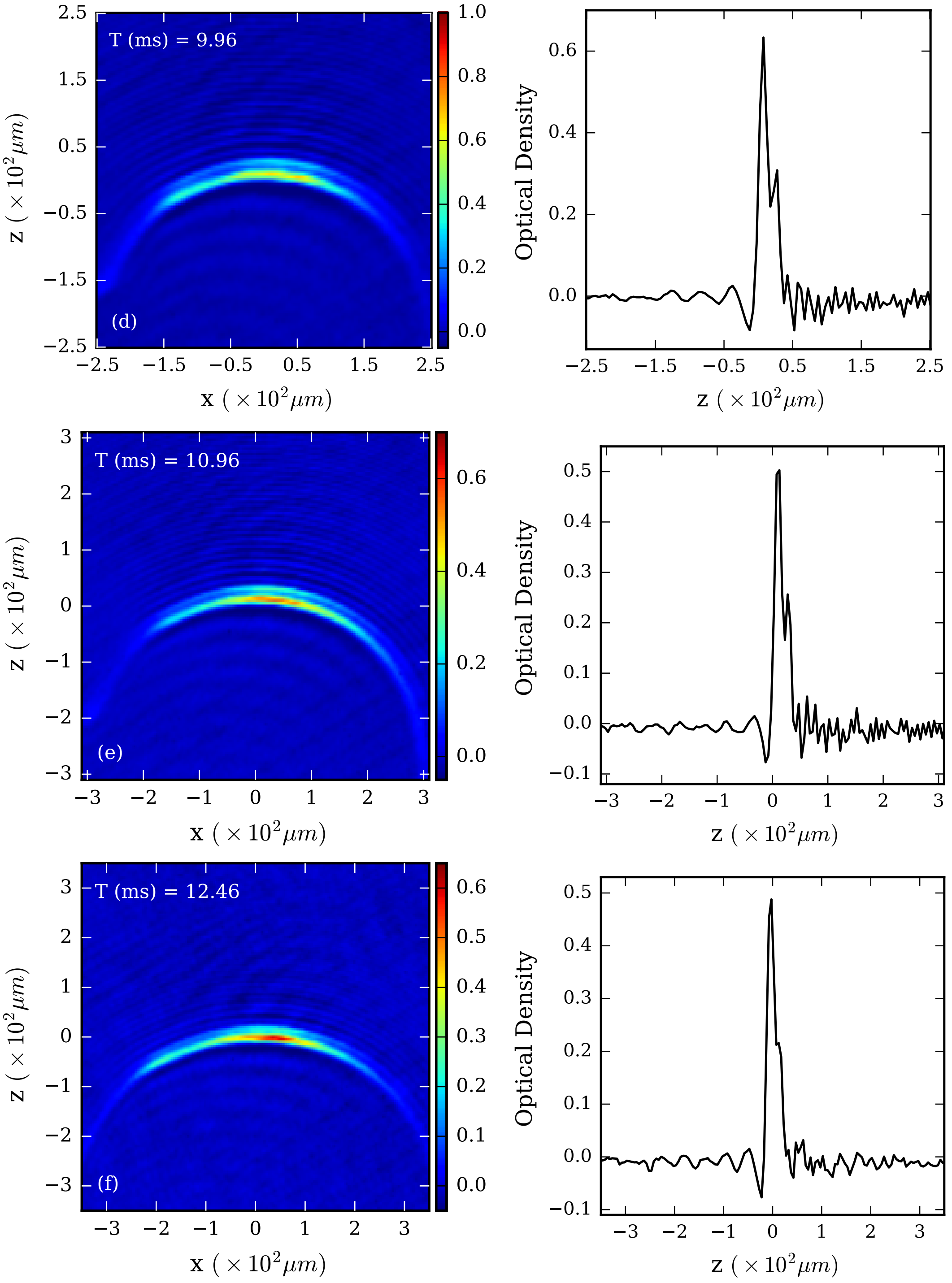

Figure 4.17: Continuation of the evolution of the condensate after the first hit at barrier: (d) Splitting feature along vertical direction enhances (e) Wave packet reaches the maximum altitude and continues to squeeze along the vertical direction (f) Condensate starts to revert and splitting feature starts to disappear

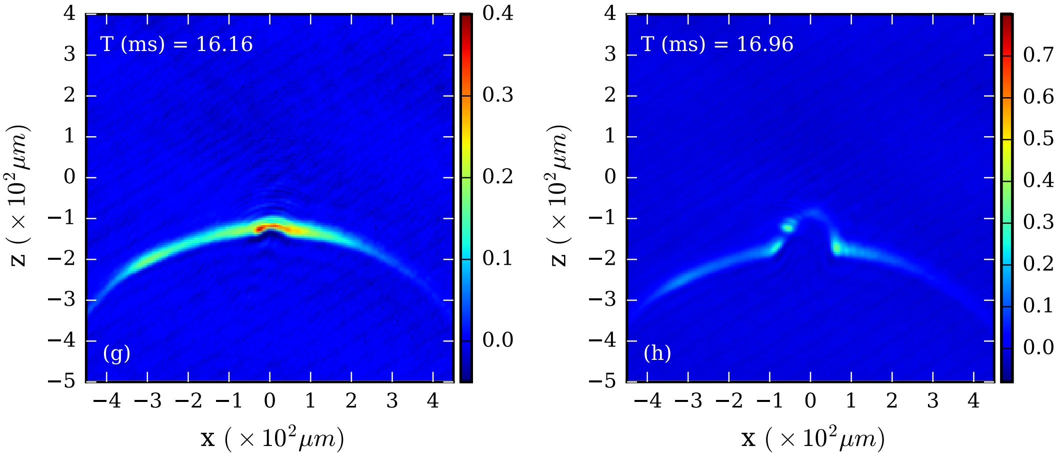

Figure 4.18: Absorption images of the falling condensate during second hit on the barrier: (g) Extent of the cloud becomes larger than the barrier size during the second hit therefore, the only central part is reflected back (h) Shows the emergence of fringe pattern in the falling side arm of the condensate. Asymmetric reflection makes the fringes appear only at the right side of the condensate arc

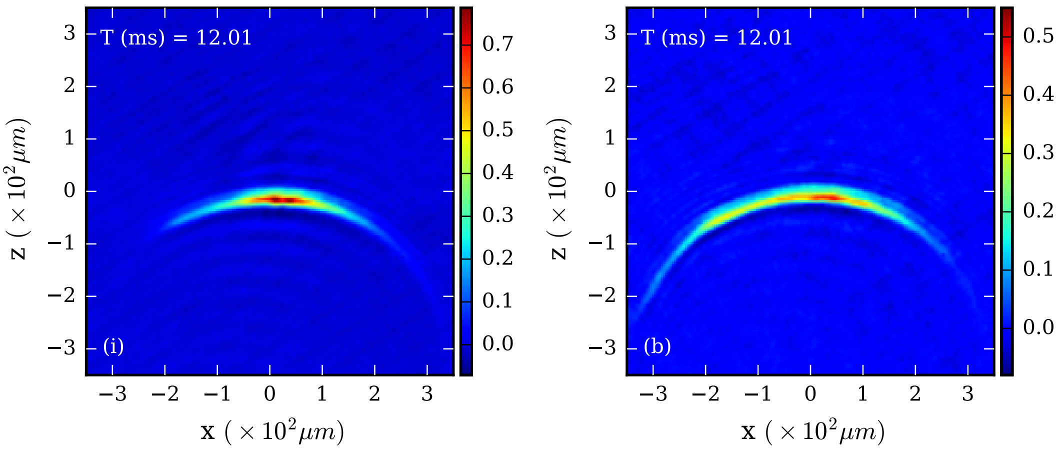

Figure 4.19: Absorption images of the reflected condensate for two different barrier strength: Images taken after a TOF of 12.01 ms. Barrier is placed 100 μm below the condensate. (a) Reflection for barrier beam power, P = 12.5 mW (b) Reflection for barrier beam power, P = 7.4 mW. Arc length of the reflected condensate is found to be more in case of weaker barrier. Also, the curvature of the arc is larger for weaker barrier

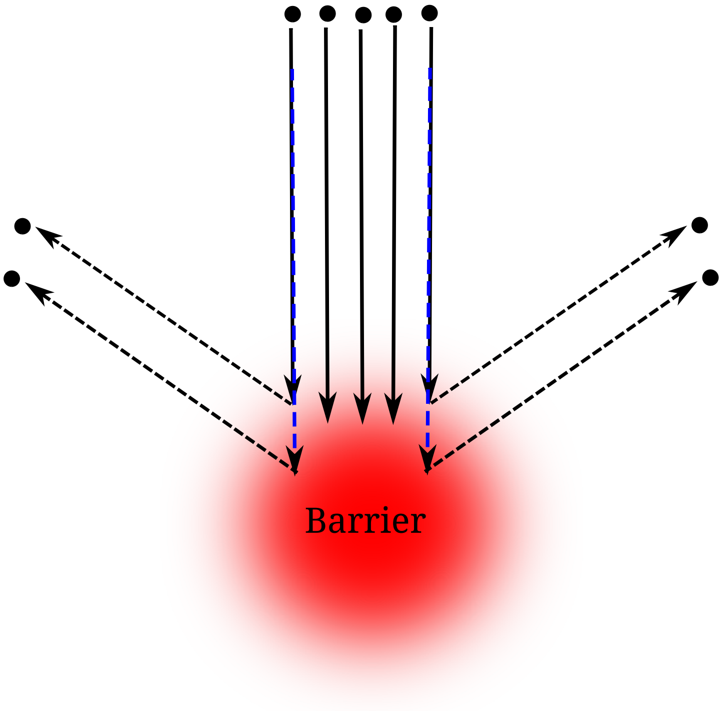

Figure 4.20: Illustration showing the reflection of the atoms from a Gaussian barrier: For reduced barrier power, atoms can penetrate deep into the barrier resulting in longer reflected arc compared to a strong barrier. Also, the curvature of the reflected arc will be larger in case of a weak barrier

improve the contrast of the fringes, each absorption images shown in the figures is the averaged of 7-10 frames.

Next, we changed the distance of the barrier from condensate to 130 μm which makes the impact velocity of the condensate larger at the barrier. This results in further penetration of the cloud into the barrier. We noticed that interaction time and overall dynamics of the condensate remains the same as shown in Fig. 4.16, 4.17 and 4.18. Due to increased separation between condensate and barrier, condensate takes a larger time to traverse the same. During this large time gap condensate expands and the density of the cloud falls significantly, affecting the contrast of the fringes during the second reflection.

In this experiment, we also explored the effect of barrier strength on the bouncing dynamics. Barrier strength can be changed by either changing the detuning or the power of the beam. In our experiment, we changed the barrier strength by varying the power of the barrier. Fig. 4.19 shows the reflected cloud at two different powers in the barrier beam. We observed the arc length of the reflected cloud for a weak barrier is larger than a hard barrier. Not only that but also we observed the curvature of the arms become larger for weak barrier. This can be understood by looking at the reflection of particles from a weak barrier as shown in Fig. 4.20. For a weak barrier, the particles penetrate deep into the barrier and get reflected from a smaller circle (inner part of the barrier beam) which leads to scattering of atoms in a larger arc.

The shape of the reflected arc depends on the momentum imparted in the horizontal direction to the atoms. For a weak barrier, the imparted momentum is low hence the shape of the reflected cloud is more like a parabola whereas, for the harder barrier, large imparted momentum makes the arc circular.

4.5.3 Simulation Results

We can't observe the dynamics for a long time in experiments, as the condensate expands very fast making the signal to noise ratio poor. Therefore, we numerically simulate the dynamics of bouncing BEC using Gross-Pitaevskii Equation. There were many challenges encountered in numerically simulating the dynamics which includes the geometry of our condensate. In our experiment, the trap is spherically symmetric which in principle demands a solution of the full 3D GP equation. For the given spatial and temporal length scales, 3D simulations become computationally expensive. We overcame this problem by adopting the numerical formulation from Ref. [294] where they reported the reflection of BEC from a flat optical barrier. They reduce the 3D GP equation to effective 1D GP equation which qualitatively reproduces the bouncing dynamics along the vertical direction (gravity axis). On similar lines, we converted the 3D GP equation into an adequate 2D GP equation including the ballistic expansion along the integration direction. This equation is solved numerically to see the dynamics of condensate along x and z-direction and can be written as

$$i\hbar\frac{\partial}{\partial t}\psi(x,z)=\left[-\frac{\hbar^2}{2m}\left(\frac{\partial^2}{\partial x^2}+\frac{\partial^2}{\partial z^2}\right)+V(x,z)+g_{\text{eff}}u(t)N|\psi(x,z)|^2\right]\psi(x,z) \quad (4.24)$$

where $V(x,z)$ describes the combined potential due to gravity and the Gaussian barrier given as

$$V(x,z)=v_0\exp\left[-2\left(\frac{z-z_0}{w_z}\right)^2-2\left(\frac{x}{w_x}\right)^2\right]+mg_{\text{acc}}z \quad (4.25)$$

where g_{acc} is the acceleration due to gravity and strength of the barrier is calculated as $v_0=\frac{2PU_0}{\pi w_z w_x}$ where w_x, w_y are the beam waist, z_0 is the position of the barrier beam with respect to condensate and P is the power in the barrier beam.

Effective mean field energy of atom-atom interactions is given by $g_{\text{eff}}u(t)N|\psi(x,z)|^2$ where $u(t)$ takes care of the condensate expansion along integration (y-axis) direction and N is the total number of atoms in the condensate.

$$g_{\text{eff}}=g\frac{\int|\psi(x,y,z)|^4dxdydz}{\int|\psi(x,z)|^4dxdz} \quad (4.26)$$

g_{eff} is estimated such that the total potential energy of atom-atom interactions in the effective 2D simulation at $t=0$ equals the total potential energy of atom-atom interactions of the 3D condensate as given by Eq. (4.26). Here $\psi(x,y,z)$ represent the initial ground state wave function of a 3D harmonic trap with Thomas-Fermi radii, R_x, R_y and R_z and $g=\frac{4\pi\hbar^2 a}{m}$ represent the corresponding atom-atom interaction.

$$|\psi(x,y,z)|^2=\begin{cases}\frac{15}{8\pi R_xR_yR_z}\left[1-\frac{x^2}{R_x^2}-\frac{y^2}{R_y^2}-\frac{z^2}{R_z^2}\right], & \text{if } x\le R_x, y\le R_y, z\le R_z\\ 0, & \text{otherwise}\end{cases} \quad (4.27)$$

$$|\psi(x,z)|^2=\begin{cases}\frac{2}{\pi R_xR_z}\left[1-\frac{x^2}{R_x^2}-\frac{z^2}{R_z^2}\right], & \text{if } x\le R_x, z\le R_z\\ 0, & \text{otherwise}\end{cases} \quad (4.28)$$

We estimate the effective interaction using Eq. (4.27) and (4.28), as $g_{\text{eff}}=g\frac{45\pi}{56R_y}$ where g_{eff} is found to be inversely proportional to the Thomas-Fermi radius, R_y (radius of condensate along the integration direction). During expansion of the cloud, R_y will change as $R_0\sqrt{1+(\omega_y t)^2}$ therefore, we consider the decay form of effective interactions as, $u(t) = \frac{1}{\sqrt{1+(\omega_y t)^2}}$ to include the effect of ballistic expansion along integration direction in effective 2D GP equation.

$$i\frac{\partial}{\partial\tilde{t}}\tilde{\psi}(\tilde{x},\tilde{z}) = \Big[-\frac{1}{2}(\frac{\partial^2}{\partial\tilde{x}^2}+\frac{\partial^2}{\partial\tilde{z}^2}) + \tilde{V}(\tilde{x},\tilde{z}) + \tilde{g}_{\text{eff}}u(\tilde{t})|\tilde{\psi}(\tilde{x},\tilde{z})|^2\Big]\tilde{\psi}(\tilde{x},\tilde{z}) \tag{4.29}$$

We scale the effective 2D GP equation and transform it into dimensionless form as given by Eq. (4.29), where $\tilde{g}_{\text{eff}} = \frac{45\pi\omega_z}{56\omega_y}\frac{\tilde{g}}{\sqrt{2\tilde{\mu}}}$. Scaling method and standard technique to solve GP equation are described in chapter 2. Reducing the 3D GP equation to 2D GP equation solves the problem partially. As mentioned in chapter 2, to simulate the dynamics of BEC, we calculate the initial ground state (wave function) on a defined spatial and momentum grid (array). The extent of the array is defined such that the at all times wave function is confined well within the spatial and momentum grid without hitting the boundaries. Also, our studies are not trap bound hence continuous expansion of BEC demands a large array to accommodate the expanding wave function in the grid at all times. Numerical simulation on a large array increases the computation time. To optimize over the computational time, we adopt the method of incrementing the extent of spatial grid iteratively over fixed intervals such that it does not alter the extent of momentum grid. The wave function is evolved initially on a smaller grid of fixed spatial resolution, and before the wave function hits the boundary of the array, the wave function is transferred to an empty larger grid with the same spatial resolution.

In simulation, we consider a spherically symmetric trap with trap frequencies, $\omega_z = \omega_y = \omega_x = 2\pi \times 80$ Hz (as found from parametric resonances) containing $N = 60000$ atoms and neglect the small angle between the propagation direction of barrier beam with respect to y-axis, we compute the ground state of the above harmonic oscillator in an effective 2D GP equation setup using imaginary time evolution with given scaled parameters such as $\tilde{\mu} = \frac{1}{2}(\frac{15\tilde{g}}{4\pi})^{2/5}$, $\tilde{g} = \frac{4\pi aN}{a_0}$ where a is the scattering length and m is the mass of the Rb atom, $\tilde{x} = x/a_0$, $\tilde{z} = z/a_0$, $\tilde{t} = \omega_z t$, $\tilde{V}(\tilde{x},\tilde{z}) = \frac{V(x,z)}{\hbar\omega_z}$ where harmonic oscillator length scale is given as $a_0 = \sqrt{\frac{\hbar}{m\omega_z}}$. This calculated ground state is used to evaluate the real-time evolution of the condensate in a combined potential due to barrier and gravity.

In the numerical simulation, we consider the barrier at a distance of 60 μm below the initial position of the condensate. This distance is shorter than what we have in

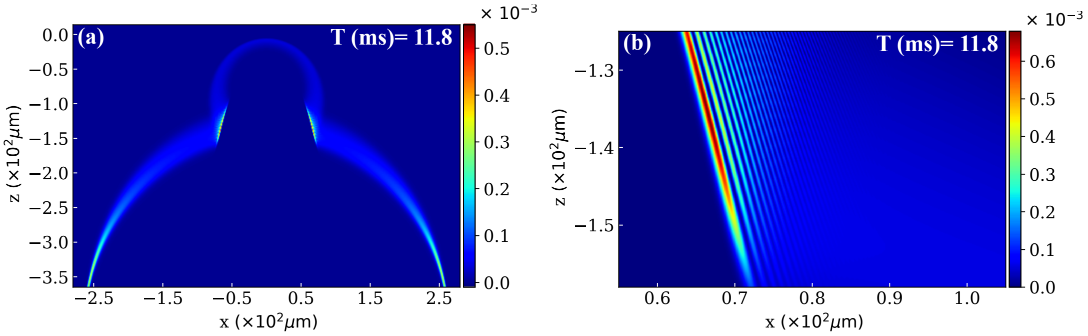

Figure 4.21: Numerical solution of effective 2D GP equation: Barrier is placed 60 μm below the condensate with barrier beam power, P = 11.5 mW. (a) A color plot shows the secondary reflection of the condensate at TOF of 11.8 ms. (b) Shows the zoom in area of the same plot where the formation of the fringe pattern similar to what we observed in the experiment can be seen. The plot shows the scaled density of the cloud.

the experiment. The barrier is kept at a shorter distance to save on the computation time as the distance between the condensate doesn't affect the dynamics significantly. Power in the barrier is taken as 11.5 mW instead of 12.5 mW (considering the losses by optical elements in the path of barrier beam and condensate), beam waist as 30 μm and detuning as 25.7 THz. We qualitatively reproduce the dynamics and features of the bouncing BEC as shown in Fig. 4.21 where the secondary reflection and fringe pattern similar to experimental finding, is observed. We also numerically reproduce the effect of stronger and weaker barrier on the dynamics of the condensate where weaker barrier results in longer arc length and larger curvature of the reflected cloud as shown in Fig. 4.22.

In the numerical simulation, the ground state of the harmonic oscillator was evaluated on an array of size $2^9 \times 2^{11}$. In numerics, we can't take an arbitrary spatial resolution, dx, of the grid as spatial resolution decides the extent of momentum grid ($P_{\text{max}} \propto \frac{1}{dx}$ where P_{max} is the extent of momentum grid). We need to keep the extent of momentum grid larger than the maximum momentum ($\sim$ 2 times) acquired by the condensate during the evolution.

Maximum momentum acquired by the freely falling condensate under the gravity keeps increasing until it hits the barrier. Therefore we can estimate the limits on the extent of momentum grid along the gravity direction but after reflection, the maximum momentum acquired in the horizontal direction depends on the size and strength of

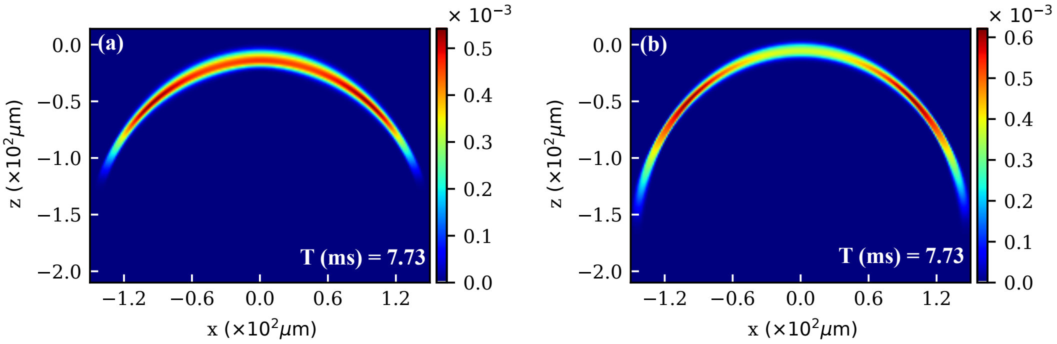

Figure 4.22: Numerical simulation: Comparison of reflected condensate for two different barrier strength at TOF of 7.73 ms. Barrier is placed 60 μm below the condensate. (a) Power in the barrier beam P = 10.3 mW (b) Power in the barrier beam P = 5.6 mW. In agreement with the experimental observation, length and curvature of the reflected arc is found to be more in case of weaker barrier

barrier, which could not be estimated at the beginning of the simulation. Therefore, we had to run initial trial programs to figure out what maximum limit on the extent of momentum grid needs to be put along the horizontal direction. Once, the two limits are known we decide the spatial resolution along x and z-direction to optimise the computational time and resources accordingly. We do the real-time evaluation on a dynamical grid where spatial resolution is fixed during the iterative increment of the spatial grid as the size of cloud increases during expansion. The grid size is increased by adding the data points in the power of 2 keeping the spatial resolution same. The maximum array/grid size in the iterative process reaches to $2^{14} \times 2^{15}$ points.

Decided by the extent of momentum grid, we use a spatial resolution of 0.039 μm and a temporal resolution of 0.74 μs. We evolve the condensate up to 12 ms. During numerical simulation, we also found that these fringes can be converted into solitons given the atom-atom interactions are increased.

4.6 Summary

In this chapter, we explored the dynamics of BEC in the linear regime. First, we reported the experimental setup and sequence to produce BEC of ^{87}Rb with 7.2×10^4 atoms in a cross-optical dipole trap. Then we presented the characterisation of trap using parametric resonances and through numerical modelling. We found the trap to be nearly spherically symmetric with trapping frequencies $\omega_x = \omega_y = \omega_z \sim 80$ Hz. Later, we described the experimental and numerical results on the dynamics of BEC in the linear regime where a freely falling condensate bounces off a Gaussian hill. We noticed a considerable difference between the dynamics of BEC bouncing off a Gaussian barrier and the one bouncing off a flat barrier which was reported earlier in Ref. [294]. We showed that in the case of a Gaussian barrier the reflected cloud carries the impression of potential and forms a circular arc. This arc expands quickly in the direction perpendicular to gravity and becomes much larger than the extent of the barrier until it reaches the barrier for the second reflection. We observed, the emergence of a fringe pattern during the second reflection which arose from the interference between the falling and reflected part of the condensate. In the end, we commented on the possibility of converting these fringes into solitons by increasing the atom-atom interactions in the system. We also discussed the effect of barrier strength and impact velocity of the cloud on the bouncing dynamics. We addressed some of the challenges in implementing the full 3D and effective 2D numerical simulation. In conclusion, we could reproduce the experimental observations qualitatively through our numerical simulations.

Chapter 5

Summary and Conclusion

In this work, we tried to understand the behaviour of ^{87}Rb Bose-Einstein condensate in two extreme regimes, one where the atom-atom interactions are dominant in the condensate and referred as a non-linear regime, and in the linear regime where interactions become negligible.

In the study of a nonlinear regime, we mainly focused on the generation and dynamics of dark solitons in a harmonically trapped two-dimensional condensate. With the aid of numerical simulations, we found how imprinting a smooth phase gradient (experimentally realizable condition) in contrast to sharp phase gradient can affect the dynamics of dark solitons. We noticed that by keeping a constant phase difference of π across the condensate and only making the gradient smoother, the instability dynamics of solitons gets modified. We found that a flatter phase gradient tends to produce moving gray solitons unlike stationary solitons in case of sharp phase gradient where the width of the gradient governs the velocity of solitons. Instability dynamics of solitons in case of smooth phase gradient was found to be noticeably different where solitons would start to break from the ends (near the edges of the trap) unlike in a stationary soliton where the instability first occurs at the centre of the trap. It is also observed that once the solitons break into a chain of vortices, the rate of decay of these vortices would depend on the width of the gradient. Smoother the gradient, faster is the decay. With this study, we explored the alternative method to generate dark solitons where we reported a new way of creating these structures in a double-well potential along with a periodic temporal variation of the interactions. This method resulted in the formation of a soliton lattice where the effect of the central barrier height on the properties of the solitons was explored. It was found that, for a feeble barrier strength, the periodic modulation of interactions in the system results in the formation of faraday pattern only, while for intermediate barrier strengths we noticed the coexistence of faraday pattern and a soliton lattice. For very high barrier strengths only soliton lattice is observed. A relation between the modulation frequency of the interactions and lattice periodicity was established and the lifetime of soliton lattice as a function of barrier strength was studied.

In the second part of the thesis, we discussed the limitation of realising the soliton lattice in our current experimental system and results of the experimental and numerical study to understand the behaviour of condensate in linear regime was reported. We looked at the results of a specific experiment where the bouncing dynamics of free falling condensate on a Gaussian hill was studied. The density of a freely falling condensate declines over time making the interactions in the condensate negligible. Initially, we discussed the experimental setup and sequence to produce BEC of ^{87}Rb atoms in a cross-optical dipole trap followed by the characterisation of trap using parametric resonances and through numerical modelling. The trap was found to be nearly spherically symmetric. We showed, in the case of a Gaussian barrier, reflected cloud carries the impression of potential and forms a circular arc. This arc expands quickly in the perpendicular direction to gravity and becomes much larger than the extent of the barrier when it reaches the barrier during the second reflection. We observed, the emergence of a fringe pattern during the second reflection which arose from the interference between the falling and reflected part of the condensate. In the numerical simulation, we found the possibility of converting these fringes into solitons by cranking up the atom-atom interactions in the condensate. We also discussed the effect of barrier strength and impact velocity of the cloud on the bouncing dynamics. Qualitatively the dynamics were reproduced through numerical simulations which were done to look at the condensate dynamics for a long time. Some of the challenges in implementing the full 3D and effective 2D numerical simulation were discussed.

In conclusion, We highlighted the dynamics of the condensate in the non-linear and linear regime.

Chapter 6

Future Outlook

In this chapter, we provide a path forward to realise formation of 2D soliton lattice (discussed in chapter 3) experimentally. Initially, we review the advancement of the generation of 2D condensate, double well potential and detection schemes. We discuss the possibilities and ways of modifying the current trap geometry from 3D to 2D. The modifications are suggested keeping in mind the constraints on the experimental setup. As it was found in our numerical study that soliton lattice can be formed either by periodically modulating the scattering length or by periodically modulating the barrier height, the latter being a simpler method, we discuss the implementation of barrier height modulation here.

6.1 Lower Dimensional Condensate and Previous Studies

Optical dipole traps have proved to be of great worth in realising highly anisotropic traps which allows changing the dimensionality of the gas by freezing the motion of atoms in one or two directions. Quantum gases in low dimension open the avenue to understand the rich physics of low-dimensional systems e.g. a two dimensional electron gas in condensed matter systems leads to an exciting research field where fractional quantum hall effect, Berezinskii – Kosterlitz – Thouless (BKT) crossover [77], One-Dimensional Tonks-Girardeau gas [76] can be observed. The mechanism and general framework for understanding the 2D condensation was described by Berezinskii [299], Kosterlitz and Thouless [300]. The BKT mechanism finds its application to many other physical phenomena in discrete systems such as the ordering of spins on a 2D lattice [301] and melting of 2D crystals [302, 303]. Initial experimental studies on 2D quantum gases mainly focused on their properties near BKT transition point [77, 304–309]. Details on the physics of 2D Bose fluids can be found in Ref. [310].

Dimensionality of physical systems influences the properties of phase transition and the kind of order present in the low-temperature states of matter. Typically highly ordered states are more robust in higher dimensions against thermal and quantum fluctuations than in lower dimensions. As mentioned earlier in chapter 1, for the case of infinite and uniform non-interacting 2D Bose gas, thermal fluctuations at any non-zero temperature are strong enough to destroy the fully ordered state, however, for an interacting system at low temperatures the ordered state (BEC) can be achieved against thermal fluctuations.

Strongly anisotropic traps are used to experimentally realize 2D atomic Bose gases. Simplest scheme to produce a 2D gas is to use a single dipole potential generated by a red-detuned light sheet. This scheme was implemented at MIT to produce the first quasi 2D condensate of sodium atoms [203] and later implemented at NIST to study the coherence properties of 2D gas [304]. Besides this scheme, many other ways were explored to produce 2D gas such as using evanescent light wave at the surface of a glass prism[311, 312]. In such cases, atoms are trapped few micrometers away from the glass surface which provides the tight confinement along vertical direction while an additional laser beam or a magnetic field is used to provide a shallow confinement in the plane. In such cases, as the confinement in the horizontal plane and along vertical direction have different origins, it offers the possibility to study the ballistic expansion of the atom in the XY plane by releasing only the planar confinement. Another system providing similar independent confinement has been undertaken at Oxford, where tight confinement along the direction of gravity is provided by a blue-detuned, single node Hermite Gaussian laser beam while the xy planar confinement is provided by a magnetic field gradient [313]. A 1D optical lattice setup is another convenient way to prepare stacks of 2D gases [80, 314–317]. A 1D optical lattice formed by two counter-propagating beams provides tight confinement along the direction of the propagation direction. The small lattice period in such a cases results in populating of many planes where addressing a single plane becomes difficult. A significant amount of work on 2D condensate in box type potential has been reported by the group of Prof. Jean Dalibard [318–320].

6.2 2D Optical Dipole Trap

As discussed in chapter 4, currently we have a crossed dipole trap set up to prepare the condensate. The linearly polarized two optical dipole beams are derived from a 1064 nm, 20 W CW fiber laser. These beams are prepared as a first-order deflection of Accousto-Optic Modulators (AOM's) which shifts the frequency of each beam by 110 MHz and 120 MHz respectively. AOMs are used for fast switching and to control the power of dipole beams individually. These first order deflections of both the beam are appropriately shaped and collimated. The diameter of the collimated beam is adjusted to 4.3 mm in the horizontal plane and 5 mm in the vertical direction. Both collimated beams are focused at the magnetic trap center using a plano-convex lens of $f = 200$ mm focal length. The angle between both the beams is nearly $\sim 55\ ^\circ$. This configuration can be modified as follows.

The imaging beam in the current setup propagates parallel to the optical table. In our study [196], we have considered a 2D condensate with 10^5 atoms in a harmonic trap with trapping frequencies $\omega_{x,y} = 10$ Hz and $\omega_z = 700$ Hz. For this kind of trap, a crossed dipole trap with light sheets can be created. To generate this trap instead of using a convex lens which gives a nearly symmetric focus $w_x = w_y$, a combination of cylindrical lenses can be used to focus the collimated beam to generate a highly asymmetric beam ($w_x \gg w_z$ or vice versa) to match the given trapping frequencies. As gravitational potential not only makes the trapping potential asymmetric at low powers but also reduces the depth of the trapping potential. Therefore, it is advantageous to keep tight confinement of the beam along z or vertical direction (along the gravity). This scenario would require the modification in our imaging setup where imaging beam needs to traverse vertically in contrast to the current setup where it lies in the horizontal plane. The imaging beam can be setup in the same way as it was there for the earlier version of the setup [1]. Using a combination of two cylindrical lenses with focal length $f = 100$ mm (Thorlabs) and $f = 1000$ mm, such that the focusing axis of both the lenses are perpendicular to each other, with the initial collimated beam of 5 mm beam waist, a focal spot of 13.4 μm by 134 μm can be generated at the center of magnetic trap. A slight asymmetry in the initial beam waists of the collimated beam will increase this ratio further. Assuming a 5 W power in each of the beam, a trap depth of 400 - 500 μK can be estimated which is sufficient for the loading of the cross dipole trap.

This configuration of the trap corresponds to the trapping frequencies $\omega_x = 440$ Hz, $\omega_y = 236$ Hz, $\omega_z = 4950$ Hz. The difference in the trapping frequencies along x and y-direction comes from the fact that the two beams are not perpendicular to each other. Evaporative cooling sequence can optimized with this configuration. Near the end of evaporative cooling cycle, assuming the powers in the beams is around 55 mW and 0.1 A current in the Quad-coils, a trap depth of 2 μk and corresponding trapping frequencies of $\omega_x = 46$ Hz, $\omega_y = 28$ Hz, $\omega_z = 500$ Hz can be estimated. This ratio of the trap frequencies and atoms $\leq 10^5$ atoms would strictly satisfy the condition of quasi 2D condensate.

6.3 Double Well Potential

To transform the 2D harmonic trap to double well potential, a barrier beam is required. In our work [196], the beam waist of the Gaussian barrier beam is taken around 0.6 μm. The method for barrier beam preparation mentioned in chapter 4 Sec. 4.5.1 can be used to split the condensate. However, to generate a focal spot of ~ 1 μm, a microscope objective would be suitable. The size of the glass cell would restrict the minimum working distance of the objective, allowing minimum working distance to be 20 mm. Therefore, large working distance microscope objective would be required, Objectives similar to MY20X-804 (0.42 NA) or MY10X-803 (0.28 NA) from Thorlabs can be used, which provides a working distance of 20 mm and 34 mm respectively. With full aperture illumination at the focus, spot size of 2.2 μm and 3.39 μm can be generated respectively. The barrier beam can be setup along the current imaging direction (along y-axis). With the given spot size, for 1 μW power, the barrier strength is estimated as $\overline{V_0} \sim 50$ and in our work [196], we have used the barrier strength of $\overline{V_0} \sim 0.003$. A cube and half wave plate just before the objective can be used to get better control over the intensity of the beam. Alternatively, a barrier beam may also be generated using a combination of laser beam collimator (60 FC-Q780-4-M100-37 currently available in the lab) and a cylindrical lens (Thorlabs, LJ1695RM-B) of $f = 50$ mm. A collimated beam of $1/e^2$ diameter of 22.5 mm can be focused to generate a sheet of focal spot size 22.5 mm × 2.2 μm.

6.4 Modulation of Interaction or Barrier Strength

As mentioned in chapter 3, the soliton lattice can be realised either by periodically modulating the interactions in the system or by modulating the strength of the barrier. Latter being a more simpler approach, can be implemented by modulating the input control voltage of barrier beam AOM. The frequency of modulation used in our numerical study [196] is about 0.2 ω_z – 0.6 ω_z which is around 140 Hz – 420 Hz.

6.5 Detection

The standard absorption imaging can be used to detect the soliton lattice. In our study, the periodicity of lattice varies from 4 μm to 8 μm. The imaging system can be modified to be able to resolve these structure. We have an EMCCD camera, where, each pixel is of 8 μm × 8 μm. Magnification of the image would be required to resolve these structures. Time of flight measurement would cause a quick expansion along the integration direction which should not disturb the lattice.

6.6 Summary

In this chapter, we have discussed some of the possible ways to modify the trap geometry to realise and detect the quasi-2D condensate subject to the experimental constraints.

Bibliography

[1] S. Kumar. *Towards distributed quantum information processing using coupling of neutral atoms to plasmonic nanostructures*. Ph.D. thesis, Indian Institute of Science Education and Research, Pune (2017). URL `http://210.212.192.152:8080/xmlui/handle/123456789/871`.

[2] A. Einstein. *Quantentheorie des einatomigen idealen Gases (chapt. 27)* (John Wiley and Sons, Ltd, ISBN: 9783527608959, 2006). URL `https://doi.org/10.1002/3527608958.ch27`.

[3] M. H. Anderson, J. R. Ensher, M. R. Matthews, C. E. Wieman, and E. A. Cornell, "Observation of Bose-Einstein condensation in a dilute atomic vapor", *Science* **269**, 198 (1995). URL `http://science.sciencemag.org/content/269/5221/198`.

[4] K. B. Davis, M. O. Mewes, M. R. Andrews, N. J. van Druten, D. S. Durfee, D. M. Kurn, and W. Ketterle, "Bose-Einstein condensation in a gas of sodium atoms", *Phys. Rev. Lett.* **75**, 3969 (1995). URL `https://link.aps.org/doi/10.1103/PhysRevLett.75.3969`.

[5] C. C. Bradley, C. A. Sackett, J. J. Tollett, and R. G. Hulet, "Evidence of Bose-Einstein condensation in an atomic gas with attractive interactions", *Phys. Rev. Lett.* **75**, 1687 (1995). URL `https://link.aps.org/doi/10.1103/PhysRevLett.75.1687`.

[6] G. Kirchhoff and R. Bunsen, "Chemische analyse durch spectralbeobachtungen", *Annalen der Physik* **186**, 161 (1860). URL `https://onlinelibrary.wiley.com/doi/abs/10.1002/andp.18601860602`.

[7] H. Hertz, "Ueber einen einfluss des ultravioletten lichtes auf die electrische entladung", *Annalen der Physik* **267**, 983 (1887). URL `http://adsabs.harvard.edu/abs/1887AnP...267..983H`.

[8] A. Einstein, "Über einen die Erzeugung und Verwandlung des Lichtes betreffenden heuristischen Gesichtspunkt", *Annalen der Physik* **322**, 132 (1905). URL `https://doi.org/10.1002/andp.19053220607`.

[9] P. M. L. De Broglie. *Recherches sur la théorie des quanta*. Ph.D. thesis, Masson, Paris (1924). URL `https://tel.archives-ouvertes.fr/tel-00006807/document`.

[10] Bose, "Plancks gesetz und lichtquantenhypothese", *Zeitschrift für Physik* **26**, 178 (1924). URL `https://doi.org/10.1007/BF01327326`.

[11] K. Huang. *Statistical mechanics (2nd edition)* (Wiley, ISBN: 0471815187, 1987).

[12] P. Kapitza, "Viscosity of liquid helium below the λ-point", *Nature* **141**, 74 (1938). URL `http://dx.doi.org/10.1038/141074a0`.

[13] J. F. Allen and A. D. Misener, "Flow of liquid helium II", *Nature* **141**, 75 (1938). URL `http://dx.doi.org/10.1038/141075a0`.

[14] F. London, "On the Bose-Einstein condensation", *Phys. Rev.* **54**, 947 (1938). URL `https://link.aps.org/doi/10.1103/PhysRev.54.947`.

[15] F. London, "The λ-phenomenon of liquid helium and the Bose-Einstein degeneracy", *Nature* **141**, 643 (1938). URL `http://dx.doi.org/10.1038/141643a0`.

[16] L. Landau, "Theory of the superfluidity of helium II", *Phys. Rev.* **60**, 356 (1941). URL `https://link.aps.org/doi/10.1103/PhysRev.60.356`.

[17] Bogoliubov, "On the theory of superfluidity", *Journal of Physics* **XI**, 23 (1947). URL `https://www.ufn.ru/dates/pdf/j_phys_ussr/j_phys_ussr_1947_11_1/3_bogolubov_j_phys_ussr_1947_11_1_23.pdf`.

[18] G. E. Brown. *Bose-Einstein condensation (Chapt. 18), edited by A. Griffin, D. W. Snoke and S. Stringari* (Cambridge University Press, ISBN: 9780511524240, 1995). URL `https://doi.org/10.1017/CBO9780511524240`.

[19] J. Ranninger. *Bose-Einstein condensation (Chapt. 16), edited by A. Griffin, D. W. Snoke and S. Stringari* (Cambridge University Press, ISBN: 9780511524240, 1995). URL `https://doi.org/10.1017/CBO9780511524240`.

[20] J. Bardeen, L. N. Cooper, and J. R. Schrieffer, "Microscopic theory of superconductivity", *Phys. Rev.* **106**, 162 (1957). URL `https://link.aps.org/doi/10.1103/PhysRev.106.162`.

[21] J. Bardeen, L. N. Cooper, and J. R. Schrieffer, "Theory of superconductivity", *Phys. Rev.* **108**, 1175 (1957). URL `https://link.aps.org/doi/10.1103/PhysRev.108.1175`.

[22] Q. Chen, J. Stajic, S. Tan, and K. Levin, "BCS-BEC crossover: from high temperature superconductors to ultracold superfluids", *Phys. Rep.* **412**, 1 (2005). URL `http://www.sciencedirect.com/science/article/pii/S0370157305001067`.

[23] F. Iachello. *Bose-Einstein condensation (Chapt. 17), edited by A. Griffin, D. W. Snoke and S. Stringari* (Cambridge University Press, ISBN: 9780511524240, 1995). URL `https://doi.org/10.1017/CBO9780511524240`.

[24] S. L. Cornish, N. R. Claussen, J. L. Roberts, E. A. Cornell, and C. E. Wieman, "Stable ^{85}Rb Bose-Einstein condensates with widely tunable interactions", *Phys. Rev. Lett.* **85**, 1795 (2000). URL `https://link.aps.org/doi/10.1103/PhysRevLett.85.1795`.

[25] G. Modugno, G. Ferrari, G. Roati, R. J. Brecha, A. Simoni, and M. Inguscio, "Bose-Einstein condensation of potassium atoms by sympathetic cooling", *Science* **294**, 1320 (2001). URL `http://science.sciencemag.org/content/294/5545/1320`.

[26] T. Weber, J. Herbig, M. Mark, H.-C. Nägerl, and R. Grimm, "Bose-Einstein condensation of cesium", *Science* **299**, 232 (2003). URL `http://science.sciencemag.org/content/299/5604/232`.

[27] S. Kraft, F. Vogt, O. Appel, F. Riehle, and U. Sterr, "Bose-Einstein condensation of alkaline earth atoms: ^{40}Ca", *Phys. Rev. Lett.* **103**, 130401 (2009). URL `https://link.aps.org/doi/10.1103/PhysRevLett.103.130401`.

[28] S. Stellmer, M. K. Tey, B. Huang, R. Grimm, and F. Schreck, "Bose-Einstein condensation of strontium", *Phys. Rev. Lett.* **103**, 200401 (2009). URL `https://link.aps.org/doi/10.1103/PhysRevLett.103.200401`.

[29] Y. N. M. de Escobar, P. G. Mickelson, M. Yan, B. J. DeSalvo, S. B. Nagel, and T. C. Killian, "Bose-Einstein condensation of ^{84}Sr", *Phys. Rev. Lett.* **103**, 200402 (2009). URL `https://link.aps.org/doi/10.1103/PhysRevLett.103.200402`.

[30] S. Stellmer, M. K. Tey, R. Grimm, and F. Schreck, "Bose-Einstein condensation of ^{86}Sr", *Phys. Rev. A* **82**, 041602 (2010). URL `https://link.aps.org/doi/10.1103/PhysRevA.82.041602`.

[31] P. G. Mickelson, Y. N. Martinez de Escobar, M. Yan, B. J. DeSalvo, and T. C. Killian, "Bose-Einstein condensation of ^{88}Sr through sympathetic cooling with ^{87}Sr", *Phys. Rev. A* **81**, 051601 (2010). URL `https://link.aps.org/doi/10.1103/PhysRevA.81.051601`.

[32] D. G. Fried, T. C. Killian, L. Willmann, D. Landhuis, S. C. Moss, D. Kleppner, and T. J. Greytak, "Bose-Einstein condensation of atomic hydrogen", *Phys. Rev. Lett.* **81**, 3811 (1998). URL `https://link.aps.org/doi/10.1103/PhysRevLett.81.3811`.

[33] A. Robert, O. Sirjean, A. Browaeys, J. Poupard, S. Nowak, D. Boiron, C. I. Westbrook, and A. Aspect, "A Bose-Einstein condensate of metastable atoms", *Science* **292**, 461 (2001). URL `http://science.sciencemag.org/content/292/5516/461`.

[34] A. Griesmaier, J. Werner, S. Hensler, J. Stuhler, and T. Pfau, "Bose-Einstein condensation of chromium", *Phys. Rev. Lett.* **94**, 160401 (2005). URL `https://link.aps.org/doi/10.1103/PhysRevLett.94.160401`.

[35] K. Aikawa, A. Frisch, M. Mark, S. Baier, A. Rietzler, R. Grimm, and F. Ferlaino, "Bose-Einstein condensation of erbium", *Phys. Rev. Lett.* **108**, 210401 (2012). URL `https://link.aps.org/doi/10.1103/PhysRevLett.108.210401`.

[36] Y. Takasu, K. Maki, K. Komori, T. Takano, K. Honda, M. Kumakura, T. Yabuzaki, and Y. Takahashi, “Spin-singlet Bose-Einstein condensation of two-electron atoms”, *Phys. Rev. Lett.* **91**, 040404 (2003). URL `https://link.aps.org/doi/10.1103/PhysRevLett.91.040404`.

[37] M. Lu, N. Q. Burdick, S. H. Youn, and B. L. Lev, “Strongly dipolar Bose-Einstein condensate of dysprosium”, *Phys. Rev. Lett.* **107**, 190401 (2011). URL `https://link.aps.org/doi/10.1103/PhysRevLett.107.190401`.

[38] S. O. Demokritov, V. E. Demidov, O. Dzyapko, G. A. Melkov, A. A. Serga, B. Hillebrands, and A. N. Slavin, “Bose-Einstein condensation of quasi-equilibrium magnons at room temperature”, *Nature* **443**, 430 (2006). URL `http://dx.doi.org/10.1038/nature05117`.

[39] L. V. Butov, C. W. Lai, A. L. Ivanov, A. C. Gossard, and D. S. Chemla, “Towards Bose-Einstein condensation of excitons in potential traps”, *Nature* **417**, 47 (2002). URL `https://doi.org/10.1038/417047a`.

[40] H. Deng, G. Weihs, C. Santori, J. Bloch, and Y. Yamamoto, “Condensation of semiconductor microcavity exciton polaritons”, *Science* **298**, 199 (2002). URL `http://science.sciencemag.org/content/298/5591/199`.

[41] J. Kasprzak, M. Richard, S. Kundermann, A. Baas, P. Jeambrun, J. M. J. Keeling, F. M. Marchetti, M. H. Szymaska, R. Andr, J. L. Staehli, V. Savona, P. B. Littlewood, B. Deveaud, and L. S. Dang, “Bose-Einstein condensation of exciton polaritons”, *Nature* **443**, 409 (2006). URL `http://dx.doi.org/10.1038/nature05131`.

[42] G. Modugno, M. Modugno, F. Riboli, G. Roati, and M. Inguscio, “Two atomic species superfluid”, *Phys. Rev. Lett.* **89**, 190404 (2002). URL `https://link.aps.org/doi/10.1103/PhysRevLett.89.190404`.

[43] D. J. McCarron, H. W. Cho, D. L. Jenkin, M. P. Köppinger, and S. L. Cornish, “Dual-species Bose-Einstein condensate of ^{87}Rb and ^{133}Cs”, *Phys. Rev. A* **84**, 011603 (2011). URL `https://link.aps.org/doi/10.1103/PhysRevA.84.011603`.

[44] I. Ferrier-Barbut, M. Delehaye, S. Laurent, A. T. Grier, M. Pierce, B. S. Rem, F. Chevy, and C. Salomon, "A mixture of Bose and Fermi superfluids", *Science* **345**, 1035 (2014). URL `http://science.sciencemag.org/content/345/6200/1035`.

[45] C. J. Pethick and H. Smith. *Bose-Einstein condensation in dilute gases* (Cambridge University Press, ISBN:9780511802850, 2008). URL `https://doi.org/10.1017/CBO9780511802850`.

[46] F. Dalfovo, S. Giorgini, L. P. Pitaevskii, and S. Stringari, "Theory of Bose-Einstein condensation in trapped gases", *Rev. Mod. Phys.* **71**, 463 (1999). URL `https://link.aps.org/doi/10.1103/RevModPhys.71.463`.

[47] C. C. Bradley, C. A. Sackett, and R. G. Hulet, "Bose-Einstein condensation of lithium: observation of limited condensate number", *Phys. Rev. Lett.* **78**, 985 (1997). URL `https://link.aps.org/doi/10.1103/PhysRevLett.78.985`.

[48] E. A. Donley, N. R. Claussen, S. Cornish, J. Roberts, E. Cornell, and C. E. Weiman, "Dynamics of collapsing and exploding Bose-Einstein condensates", *Nat. Phys.* **412**, 295 (2001). URL `http://dx.doi.org/10.1038/35085500`.

[49] J. M. Gerton, D. Strekalov, I. Prodan, and R. G. Hulet, "Direct observation of growth and collapse of a Bose-Einstein condensate with attractive interactions", *Nat. Phys.* **408**, 692 (2000). URL `http://dx.doi.org/10.1038/35047030`.

[50] L. Khaykovich, F. Schreck, G. Ferrari, T. Bourdel, J. Cubizolles, L. D. Carr, Y. Castin, and C. Salomon, "Formation of a matter-wave bright soliton", *Science* **296**, 1290 (2002). URL `http://science.sciencemag.org/content/296/5571/1290`.

[51] K. E. Strecker, G. B. Partridge, A. G. Truscott, and R. G. Hulet, "Formation and propagation of matter-wave soliton trains", *Nature* **417**, 150 (2002). URL `http://dx.doi.org/10.1038/nature747`.

[52] C. Chin, R. Grimm, P. Julienne, and E. Tiesinga, "Feshbach resonances in ultracold gases", *Rev. Mod. Phys.* **82**, 1225 (2010). URL `https://link.aps.org/doi/10.1103/RevModPhys.82.1225`.

[53] R. Yamazaki, S. Taie, S. Sugawa, and Y. Takahashi, "Submicron spatial modulation of an interatomic interaction in a Bose-Einstein condensate", *Phys. Rev. Lett.* **105**, 050405 (2010). URL `https://link.aps.org/doi/10.1103/PhysRevLett.105.050405`.

[54] W. D. Phillips, "Nobel lecture: Laser cooling and trapping of neutral atoms", *Rev. Mod. Phys.* **70**, 721 (1998). URL `https://link.aps.org/doi/10.1103/RevModPhys.70.721`.

[55] S. Chu, "Nobel lecture: The manipulation of neutral particles", *Rev. Mod. Phys.* **70**, 685 (1998). URL `https://link.aps.org/doi/10.1103/RevModPhys.70.685`.

[56] C. N. Cohen-Tannoudji, "Nobel lecture: Manipulating atoms with photons", *Rev. Mod. Phys.* **70**, 707 (1998). URL `https://link.aps.org/doi/10.1103/RevModPhys.70.707`.

[57] H. F. Hess, "Evaporative cooling of magnetically trapped and compressed spin-polarized hydrogen", *Phys. Rev. B* **34**, 3476 (1986). URL `https://link.aps.org/doi/10.1103/PhysRevB.34.3476`.

[58] W. Ketterle, "Nobel lecture: When atoms behave as waves: Bose-Einstein condensation and the atom laser", *Rev. Mod. Phys.* **74**, 1131 (2002). URL `https://link.aps.org/doi/10.1103/RevModPhys.74.1131`.

[59] E. A. Cornell and C. E. Wieman, "Nobel lecture: Bose-Einstein condensation in a dilute gas, the first 70 years and some recent experiments", *Rev. Mod. Phys.* **74**, 875 (2002). URL `https://link.aps.org/doi/10.1103/RevModPhys.74.875`.

[60] I. F. Silvera and J. T. M. Walraven, "Stabilization of atomic hydrogen at low temperature", *Phys. Rev. Lett.* **44**, 164 (1980). URL `https://link.aps.org/doi/10.1103/PhysRevLett.44.164`.

[61] I. F. Silvera and M. Reynolds, "Spin-polarized hydrogen: A weakly interacting boson gas", *J. Low Temp. Phys.* **87**, 343 (1992). URL `https://doi.org/10.1007/BF00114909`.

[62] W. D. Phillips and H. Metcalf, “Laser deceleration of an atomic beam”, *Phys. Rev. Lett.* **48**, 596 (1982). URL `https://link.aps.org/doi/10.1103/PhysRevLett.48.596`.

[63] K. Dieckmann, R. J. C. Spreeuw, M. Weidemüller, and J. T. M. Walraven, “Two-dimensional magneto-optical trap as a source of slow atoms”, *Phys. Rev. A* **58**, 3891 (1998). URL `https://link.aps.org/doi/10.1103/PhysRevA.58.3891`.

[64] C. Monroe, W. Swann, H. Robinson, and C. Wieman, “Very cold trapped atoms in a vapor cell”, *Phys. Rev. Lett.* **65**, 1571 (1990). URL `https://link.aps.org/doi/10.1103/PhysRevLett.65.1571`.

[65] M. R. Andrews, C. G. Townsend, H.-J. Miesner, D. S. Durfee, D. M. Kurn, and W. Ketterle, “Observation of interference between two Bose condensates”, *Science* **275**, 637 (1997). URL `http://science.sciencemag.org/content/275/5300/637`.

[66] L. Deng, E. W. Hagley, J. Wen, M. Trippenbach, Y. Band, P. S. Julienne, J. E. Simsarian, K. Helmerson, S. L. Rolston, and W. D. Phillips, “Four-wave mixing with matter waves”, *Nature* **398**, 218 (1999). URL `http://dx.doi.org/10.1038/18395`.

[67] K. W. Madison, F. Chevy, W. Wohlleben, and J. Dalibard, “Vortex formation in a stirred Bose-Einstein condensate”, *Phys. Rev. Lett.* **84**, 806 (2000). URL `https://link.aps.org/doi/10.1103/PhysRevLett.84.806`.

[68] D. M. Stamper-Kurn, A. P. Chikkatur, A. Görlitz, S. Inouye, S. Gupta, D. E. Pritchard, and W. Ketterle, “Excitation of phonons in a Bose-Einstein condensate by light scattering”, *Phys. Rev. Lett.* **83**, 2876 (1999). URL `https://link.aps.org/doi/10.1103/PhysRevLett.83.2876`.

[69] I. Bloch, T. W. Hnsch, and T. Esslinger, “Measurement of the spatial coherence of a trapped Bose gas at the phase”, *Nature* **403**, 166 (2000). URL `http://dx.doi.org/10.1038/35003132`.

[70] I. Bloch, T. W. Hänsch, and T. Esslinger, “Atom laser with a cw output coupler”, *Phys. Rev. Lett.* **82**, 3008 (1999). URL `https://link.aps.org/doi/10.1103/PhysRevLett.82.3008`.

[71] L. V. Hau, S. E. Harris, Z. Dutton, and C. H. Behroozi, “Light speed reduction to 17 metres per second in an ultracold atomic gas”, *Nature* **397**, 594 (1999). URL `http://dx.doi.org/10.1038/17561`.

[72] S. Burger, K. Bongs, S. Dettmer, W. Ertmer, K. Sengstock, A. Sanpera, G. V. Shlyapnikov, and M. Lewenstein, “Dark solitons in Bose-Einstein condensates”, *Phys. Rev. Lett.* **83**, 5198 (1999). URL `http://dx.doi.org/10.1103/PhysRevLett.83.5198`.

[73] Z. Dutton, M. Budde, C. Slowe, and L. V. Hau, “Observation of quantum shock waves created with ultra- compressed slow light pulses in a Bose-Einstein condensate”, *Science* **293**, 663 (2001). URL `http://science.sciencemag.org/content/293/5530/663`.

[74] M. Schellekens, R. Hoppeler, A. Perrin, J. V. Gomes, D. Boiron, A. Aspect, and C. I. Westbrook, “Hanbury Brown Twiss effect for ultracold quantum gases”, *Science* **310**, 648 (2005). URL `http://science.sciencemag.org/content/310/5748/648`.

[75] N. S. Ginsberg, S. R. Garner, and L. V. Hau, “Coherent control of optical information with matter wave dynamics”, *Nature* **445**, 623 (2007). URL `http://dx.doi.org/10.1038/nature05493`.

[76] T. Kinoshita, T. Wenger, and D. S. Weiss, “Observation of a one-dimensional Tonks-Girardeau gas”, *Science* **305**, 1125 (2004). URL `http://science.sciencemag.org/content/305/5687/1125`.

[77] Z. Hadzibabic, P. Krger, M. Cheneau, B. Battelier, and J. Dalibard, “Berezinskii-Kosterlitz-Thouless crossover in a trapped atomic gas”, *Nature* **441**, 1118 (2006). URL `https://doi.org/10.1038/nature04851`.

[78] B. DeMarco and D. S. Jin, “Onset of Fermi degeneracy in a trapped atomic gas”, *Science* **285**, 1703 (1999). URL `http://science.sciencemag.org/content/285/5434/1703`.

[79] S. Giorgini, L. P. Pitaevskii, and S. Stringari, “Theory of ultracold atomic Fermi gases”, *Rev. Mod. Phys.* **80**, 1215 (2008). URL `https://link.aps.org/doi/10.1103/RevModPhys.80.1215`.

[80] O. Morsch and M. Oberthaler, “Dynamics of Bose-Einstein condensates in optical lattices”, *Rev. Mod. Phys.* **78**, 179 (2006). URL `https://link.aps.org/doi/10.1103/RevModPhys.78.179`.

[81] M. Lewenstein, A. Sanpera, V. Ahufinger, B. Damski, A. Sen(De), and U. Sen, “Ultracold atomic gases in optical lattices: mimicking condensed matter physics and beyond”, *Adv. Phys.* **56**, 243 (2007). URL `https://doi.org/10.1080/00018730701223200`.

[82] D. Jaksch, C. Bruder, J. I. Cirac, C. W. Gardiner, and P. Zoller, “Cold bosonic atoms in optical lattices”, *Phys. Rev. Lett.* **81**, 3108 (1998). URL `https://link.aps.org/doi/10.1103/PhysRevLett.81.3108`.

[83] M. Greiner, O. Mandel, T. Esslinger, T. W. Hnsch, and I. Bloch, “Quantum phase transition from a superfluid to a mott insulator in a gas of ultracold atoms”, *Nature* **415**, 39 (2002). URL `http://dx.doi.org/10.1038/415039a`.

[84] R. P. Feynman, “Simulating physics with computers”, *Int. J. Theor. Phys.* **21**, 467 (1982). URL `https://doi.org/10.1007/BF02650179`.

[85] B. Paredes, A. Widera, V. Murg, O. Mandel, S. Flling, I. Cirac, G. V. Shlyapnikov, T. W. Hnsch, and I. Bloch, “Tonks-girardeau gas of ultracold atoms in an optical lattice”, *Nature* **429**, 277 (2004). URL `http://dx.doi.org/10.1038/nature02530`.

[86] I. Bloch, J. Dalibard, and W. Zwerger, “Many-body physics with ultracold gases”, *Rev. Mod. Phys.* **80**, 885 (2008). URL `https://link.aps.org/doi/10.1103/RevModPhys.80.885`.

[87] M. Lewenstein, A. Sanpera, and V. Ahufinger. *Ultracold atoms in optical lattices: simulating quantum many-body systems* (Oxford University Press, ISBN: 9780199573127, 2013). URL `http://www.oxfordscholarship.com/view/10.1093/acprof:oso/9780199573127.001.0001/acprof-9780199573127`.

[88] Z. Wu, L. Zhang, W. Sun, X.-T. Xu, B.-Z. Wang, S.-C. Ji, Y. Deng, S. Chen, X.-J. Liu, and J.-W. Pan, “Realization of two-dimensional spin-orbit coupling for Bose-Einstein condensates”, *Science* **354**, 83 (2016). URL `http://science.sciencemag.org/content/354/6308/83`.

[89] F. Wilczek, "Quantum time crystals", *Phys. Rev. Lett.* **109**, 160401 (2012). URL `https://link.aps.org/doi/10.1103/PhysRevLett.109.160401`.

[90] J. Smits, L. Liao, H. T. C. Stoof, and P. van der Straten, "Observation of a space-time crystal in a superfluid quantum gas", *Phys. Rev. Lett.* **121**, 185301 (2018). URL `https://link.aps.org/doi/10.1103/PhysRevLett.121.185301`.

[91] G. Tino, L. Cacciapuoti, K. Bongs, C. Bord, P. Bouyer, H. Dittus, W. Ertmer, A. Grlitz, M. Inguscio, A. Landragin, P. Lemonde, C. Lammerzahl, A. Peters, E. Rasel, J. Reichel, C. Salomon, S. Schiller, W. Schleich, K. Sengstock, U. Sterr, and M. Wilkens, "Atom interferometers and optical atomic clocks: new quantum sensors for fundamental physics experiments in space", *Nuclear Physics B - Proceedings Supplements* **166**, 159 (2007). Proceedings of the Third International Conference on Particle and Fundamental Physics in Space, URL `http://www.sciencedirect.com/science/article/pii/S0920563206010152`.

[92] M. J. Snadden, J. M. McGuirk, P. Bouyer, K. G. Haritos, and M. A. Kasevich, "Measurement of the earth's gravity gradient with an atom interferometer based gravity gradiometer", *Phys. Rev. Lett.* **81**, 971 (1998). URL `https://link.aps.org/doi/10.1103/PhysRevLett.81.971`.

[93] J. B. Fixler, G. T. Foster, J. M. McGuirk, and M. A. Kasevich, "Atom interferometer measurement of the newtonian constant of gravity", *Science* **315**, 74 (2007). URL `http://science.sciencemag.org/content/315/5808/74`.

[94] M. Cadoret, E. de Mirandes, P. Cladé, S. Guellati-Khélifa, C. Schwob, F. m. c. Nez, L. Julien, and F. m. c. Biraben, "Combination of bloch oscillations with a Ramsey-Bordé interferometer: new determination of the fine structure constant", *Phys. Rev. Lett.* **101**, 230801 (2008). URL `https://link.aps.org/doi/10.1103/PhysRevLett.101.230801`.

[95] G. Amelino-Camelia, C. Lämmerzahl, F. Mercati, and G. M. Tino, "Constraining the energy-momentum dispersion relation with Planck-scale sensitivity using cold atoms", *Phys. Rev. Lett.* **103**, 171302 (2009). URL `https://link.aps.org/doi/10.1103/PhysRevLett.103.171302`.

[96] G. M. Tino and F. Vetrano, "Is it possible to detect gravitational waves with atom interferometers?", *Class. Quantum Grav.* **24**, 2167 (2007). URL `http://stacks.iop.org/0264-9381/24/i=9/a=001`.

[97] G. M. Tino, F. Vetrano, and C. Lämmerzahl, "Editorial on the grg special issue on "gravitational waves detection with atom interferometry"", *Gen. Rel. Gravit.* **43**, 1901 (2011). URL `https://doi.org/10.1007/s10714-011-1196-4`.

[98] D. M. Stamper-Kurn, M. R. Andrews, A. P. Chikkatur, S. Inouye, H.-J. Miesner, J. Stenger, and W. Ketterle, "Optical confinement of a Bose-Einstein condensate", *Phys. Rev. Lett.* **80**, 2027 (1998). URL `https://link.aps.org/doi/10.1103/PhysRevLett.80.2027`.

[99] J.-R. Li, J. Lee, W. Huang, S. Burchesky, B. Shteynas, F. . Top, A. O. Jamison, and W. Ketterle, "A stripe phase with supersolid properties in spin-orbit-coupled Bose-Einstein condensates", *Nature* **543**, 91 (2017). URL `http://dx.doi.org/10.1038/nature21431`.

[100] Z. Wu, J. K. Block, and G. M. Bruun, "Liquid crystal phases of two-dimensional dipolar gases and Berezinskii-Kosterlitz-Thouless melting", *Sci. Rep.* **6**, 19038 (2016). URL `http://dx.doi.org/10.1038/srep19038`.

[101] S. Palzer, C. Zipkes, C. Sias, and M. Köhl, "Quantum transport through a Tonks-Girardeau gas", *Phys. Rev. Lett.* **103**, 150601 (2009). URL `https://link.aps.org/doi/10.1103/PhysRevLett.103.150601`.

[102] J. Catani, G. Lamporesi, D. Naik, M. Gring, M. Inguscio, F. Minardi, A. Kantian, and T. Giamarchi, "Quantum dynamics of impurities in a one-dimensional Bose gas", *Phys. Rev. A* **85**, 023623 (2012). URL `https://link.aps.org/doi/10.1103/PhysRevA.85.023623`.

[103] J. Steinhauer, "Observation of self-amplifying Hawking radiation in an analogue black-hole laser", *Nat. Phys.* **10**, 864 (2014). URL `http://dx.doi.org/10.1038/nphys3104`.

[104] J. Steinhauer, "Observation of quantum Hawking radiation and its entanglement in an analogue black hole", *Nat. Phys.* **12**, 959 (2016). URL `http://dx.doi.org/10.1038/nphys3863`.

[105] K. D. Nelson, X. Li, and D. S. Weiss, "Imaging single atoms in a three-dimensional array", *Nat. Phys.* **3**, 556 (2007). URL `http://dx.doi.org/10.1038/nphys645`.

[106] W. S. Bakr, J. I. Gillen, A. Peng, S. Flling, and M. Greiner, "A quantum gas microscope for detecting single atoms in a Hubbard-regime optical lattice", *Nature* **462**, 74 (2009). URL `http://dx.doi.org/10.1038/nature08482`.

[107] J. F. Sherson, C. Weitenberg, M. Endres, M. Cheneau, I. Bloch, and S. Kuhr, "Single-atom resolved fluorescence imaging of an atomic mott insulator", *Nature* **467**, 68 (2010). URL `http://dx.doi.org/10.1038/nature09378`.

[108] L. Pitaevskii and S. Stringari. *Bose-Einstein condensation* (Clarendon Press, ISBN: 9780198507192, 2003). URL `https://books.google.co.in/books/about/Bose_Einstein_Condensation.html?id=rIobbOxC4j4C&redir_esc=y`.

[109] M. Inguscio, S. Stringari, and C. Wieman, "Bose-Einstein condensation in atomic gases "Enrico Fermi", course cxl", *Proceedings of the International School of Physics "Enrico Fermi", IOS Press, ISBN: 978-0-96733-555-1* (1999). URL `https://www.iospress.nl/book/bose-einstein-condensation-in-atomic-gases/`.

[110] A. J. Leggett, "Bose-Einstein condensation in the alkali gases: Some fundamental concepts", *Rev. Mod. Phys.* **73**, 307 (2001). URL `https://link.aps.org/doi/10.1103/RevModPhys.73.307`.

[111] A. L. Migdall, J. V. Prodan, W. D. Phillips, T. H. Bergeman, and H. J. Metcalf, "First observation of magnetically trapped neutral atoms", *Phys. Rev. Lett.* **54**, 2596 (1985). URL `https://link.aps.org/doi/10.1103/PhysRevLett.54.2596`.

[112] R. Grimm, M. Weidemller, and Y. B. Ovchinnikov, "Optical dipole traps for neutral atoms", *Adv. At. Mol. Opt. Phys.* **42**, 95 (2000). URL `http://www.sciencedirect.com/science/article/pii/S1049250X0860186X`.

[113] I. Bloch, "Ultracold quantum gases in optical lattices", *Nat. Phys.* **1**, 23 (2005). URL `http://dx.doi.org/10.1038/nphys138`.

[114] D. Schumayer and B. Apagyi, "Relation between optical and atomic solitons", *Phys. Rev. A* **65**, 053614 (2002). URL `https://link.aps.org/doi/10.1103/PhysRevA.65.053614`.

[115] A. Scott. *Encyclopedia of nonlinear science (pp. 639-643)* (Routledge, ISBN: 9781579583859, 2005). URL `https://books.google.co.in/books?id=eSeLQgAACAAJ`.

[116] H.-H. Chen and C.-S. Liu, "Solitons in nonuniform media", *Phys. Rev. Lett.* **37**, 693 (1976). URL `https://link.aps.org/doi/10.1103/PhysRevLett.37.693`.

[117] A. Fetter, "Vortices and dynamics in trapped Bose-Einstein condensates", *J Low Temp Phys* **161**, 445 (2010). URL `https://doi.org/10.1007/s10909-010-0202-7`.

[118] C. Lobo, A. Sinatra, and Y. Castin, "Vortex lattice formation in Bose-Einstein condensates", *Phys. Rev. Lett.* **92**, 020403 (2004). URL `https://link.aps.org/doi/10.1103/PhysRevLett.92.020403`.

[119] I. S. Aranson and L. Kramer, "The world of the complex Ginzburg-Landau equation", *Rev. Mod. Phys.* **74**, 99 (2002). URL `https://link.aps.org/doi/10.1103/RevModPhys.74.99`.

[120] M. C. Cross and P. C. Hohenberg, "Pattern formation outside of equilibrium", *Rev. Mod. Phys.* **65**, 851 (1993). URL `https://link.aps.org/doi/10.1103/RevModPhys.65.851`.

[121] J. S. Russell, "Report on waves", *Report of the fourteenth meeting of the British Association for the Advancement of Science* **311**, Plates XLVII (1845). URL `https://archive.org/stream/reportonwavesma00russgoog#page/n7`.

[122] N. J. Zabusky and M. D. Kruskal, "Interaction of "solitons" in a collisionless plasma and the recurrence of initial states", *Phys. Rev. Lett.* **15**, 240 (1965). URL `https://link.aps.org/doi/10.1103/PhysRevLett.15.240`.

[123] C. S. Gardner, J. M. Greene, M. D. Kruskal, and R. M. Miura, "Method for solving the Korteweg-deVries equation", *Phys. Rev. Lett.* **19**, 1095 (1967). URL `https://link.aps.org/doi/10.1103/PhysRevLett.19.1095`.

[124] P. G. Drazin, "Solitons, nonlinear evolution equations and inverse scattering (london mathematical society lecture note series 149)", *Bulletin of the London Mathematical Society* **25**, 620. URL `https://londmathsoc.onlinelibrary.wiley.com/doi/abs/10.1112/blms/25.6.620`.

[125] T. Heimburg and A. D. Jackson, "On soliton propagation in biomembranes and nerves", *Proceedings of the National Academy of Sciences* **102**, 9790 (2005). URL `http://www.pnas.org/content/102/28/9790`.

[126] Z. Sinkala, "Soliton/exciton transport in proteins", *J. Theor. Biol.* **241**, 919 (2006). URL `http://www.sciencedirect.com/science/article/pii/S0022519306000403`.

[127] A. Porter and N. F. Smyth, "Modelling the morning glory of the gulf of carpentaria", *J. Fluid Mech.* **454**, 1 (2002). URL `https://doi.org/10.1017/S0022112001007455`.

[128] N. Akhmediev and A. Ankiewicz. *Dissipative solitons: from optics to biology and medicine* (Springer-Verlag Berlin Heidelberg, ISBN: 978-3-540-78216-2, 2008). URL `https://www.springer.com/in/book/9783540782162`.

[129] M. Remoissenet. *Waves called solitons: concepts and experiments* (Springer-Verlag Berlin Heidelberg, ISBN: 978-3-662-03790-4, 2013). URL `https://www.springer.com/in/book/9783540659198`.

[130] P. Drazin and R. Johnson. *Solitons: an introduction* (Cambridge University Press, ISBN: 052133389X, 1989). URL `https://books.google.co.in/books/about/Solitons.html?id=HPmbIDk2u-gC&redir_esc=y`.

[131] S. Stellmer, C. Becker, P. Soltan-Panahi, E.-M. Richter, S. Dörscher, M. Baumert, J. Kronjäger, K. Bongs, and K. Sengstock, "Collisions of dark solitons in elongated Bose-Einstein condensates", *Phys. Rev. Lett.* **101**, 120406 (2008). URL `http://dx.doi.org/10.1103/PhysRevLett.101.120406`.

[132] D. L. Feder, M. S. Pindzola, L. A. Collins, B. I. Schneider, and C. W. Clark, "Dark-soliton states of Bose-Einstein condensates in anisotropic traps", *Phys. Rev. A* **62**, 053606 (2000). URL `http://dx.doi.org/10.1103/PhysRevA.62.053606`.

[133] J. Brand and W. P. Reinhardt, "Solitonic vortices and the fundamental modes of the "snake instability": Possibility of observation in the gaseous Bose-Einstein condensate", *Phys. Rev. A* **65**, 043612 (2002). URL `https://link.aps.org/doi/10.1103/PhysRevA.65.043612`.

[134] V. Tikhonenko, J. Christou, B. Luther-Davies, and Y. S. Kivshar, "Observation of vortex solitons created by the instability of dark soliton stripes", *Opt. Lett.* **21**(15), 1129 (1996). URL `http://dx.doi.org/10.1364/OL.21.001129`.

[135] L. D. Carr, C. W. Clark, and W. P. Reinhardt, "Stationary solutions of the one-dimensional nonlinear Schrödinger equation. ii. case of attractive nonlinearity", *Phys. Rev. A* **62**, 063611 (2000). URL `https://link.aps.org/doi/10.1103/PhysRevA.62.063611`.

[136] L. D. Carr, C. W. Clark, and W. P. Reinhardt, "Stationary solutions of the one-dimensional nonlinear Schrödinger equation. i. case of repulsive nonlinearity", *Phys. Rev. A* **62**, 063610 (2000). URL `http://dx.doi.org/10.1103/PhysRevA.62.063610`.

[137] H. C. Kim, R. L. Stenzel, and A. Y. Wong, "Development of "cavitons" and trapping of rf field", *Phys. Rev. Lett.* **33**, 886 (1974). URL `https://link.aps.org/doi/10.1103/PhysRevLett.33.886`.

[138] K. A. Naugolnykh, L. A. Ostrovsky, O. A. Sapozhnikov, and M. F. Hamilton, "Nonlinear wave processes in acoustics", *J. Acoust. Soc. Am.* **108**, 14 (2000). URL `https://doi.org/10.1121/1.429483`.

[139] G. Agrawal. *Nonlinear Fiber Optics* (Academic Press, ISBN: 978-0-12-397023-7, 2013). URL `https://www.sciencedirect.com/science/article/pii/B978012397023700019X`.

[140] A. Hasegawa and Y. Kodama. *Solitons in optical communications* (Clarendon Press, ISBN: 9780198565079, 1995). URL `https://global.oup.com/academic/product/solitons-in-optical-communications-9780198565079?lang=en&cc=no`.

[141] D. J. Frantzeskakis, “Dark solitons in atomic Bose–Einstein condensates: from theory to experiments”, *J. Phys. A: Mathematical and Theoretical* **43**(21), 213001 (2010). URL `http://stacks.iop.org/1751-8121/43/i=21/a=213001`.

[142] P. G. Kevrekidis, D. J. Frantzeskakis, and R. Carretero-González. *Emergent nonlinear phenomena in Bose-Einstein condensates: theory and experiment* (Springer, ISBN 978-3-540-73590-8, 2008). URL `https://doi.org/10.1007/978-3-540-73591-5`.

[143] P. Emplit, J. Hamaide, F. Reynaud, C. Froehly, and A. Barthelemy, “Picosecond steps and dark pulses through nonlinear single mode fibers”, *Opt. Commun.* **62**, 374 (1987). URL `http://www.sciencedirect.com/science/article/pii/0030401887900034`.

[144] D. Krökel, N. J. Halas, G. Giuliani, and D. Grischkowsky, “Dark-pulse propagation in optical fibers”, *Phys. Rev. Lett.* **60**, 29 (1988). URL `http://dx.doi.org/10.1103/PhysRevLett.60.29`.

[145] G. A. Swartzlander, D. R. Andersen, J. J. Regan, H. Yin, and A. E. Kaplan, “Spatial dark-soliton stripes and grids in self-defocusing materials”, *Phys. Rev. Lett.* **66**, 1583 (1991). URL `http://dx.doi.org/10.1103/PhysRevLett.66.1583`.

[146] B. Denardo, W. Wright, S. Putterman, and A. Larraza, “Observation of a kink soliton on the surface of a liquid”, *Phys. Rev. Lett.* **64**, 1518 (1990). URL `http://dx.doi.org/10.1103/PhysRevLett.64.1518`.

[147] B. Denardo, B. Galvin, A. Greenfield, A. Larraza, S. Putterman, and W. Wright, “Observations of localized structures in nonlinear lattices: Domain walls and kinks”, *Phys. Rev. Lett.* **68**, 1730 (1992). URL `http://dx.doi.org/10.1103/PhysRevLett.68.1730`.

[148] M. Chen, M. A. Tsankov, J. M. Nash, and C. E. Patton, “Microwave magnetic-envelope dark solitons in yttrium iron garnet thin films”, *Phys. Rev. Lett.* **70**, 1707 (1993). URL `http://dx.doi.org/10.1103/PhysRevLett.70.1707`.

[149] R. Heidemann, S. Zhdanov, R. Sütterlin, H. M. Thomas, and G. E. Morfill, “Dissipative dark soliton in a complex plasma”, *Phys. Rev. Lett.* **102**, 135002 (2009). URL `http://dx.doi.org/10.1103/PhysRevLett.102.135002`.

[150] A. Chabchoub, O. Kimmoun, H. Branger, N. Hoffmann, D. Proment, M. Onorato, and N. Akhmediev, “Experimental observation of dark solitons on the surface of water”, *Phys. Rev. Lett.* **110**, 124101 (2013). URL `https://link.aps.org/doi/10.1103/PhysRevLett.110.124101`.

[151] A. Chabchoub, O. Kimmoun, H. Branger, C. Kharif, N. Hoffmann, M. Onorato, and N. Akhmediev, “Gray solitons on the surface of water”, *Phys. Rev. E* **89**, 011002 (2014). URL `https://link.aps.org/doi/10.1103/PhysRevE.89.011002`.

[152] T. Tsuzuki, “Nonlinear waves in the pitaevskii-gross equation”, *J. Low Temp. Phys.* **4**, 441 (1971). URL `https://doi.org/10.1007/BF00628744`.

[153] J. Denschlag, J. E. Simsarian, D. L. Feder, C. W. Clark, L. A. Collins, J. Cubizolles, L. Deng, E. W. Hagley, K. Helmerson, W. P. Reinhardt, S. L. Rolston, B. I. Schneider, and W. D. Phillips, “Generating solitons by phase engineering of a Bose-Einstein condensate”, *Science* **287**, 97 (2000). URL `http://dx.doi.org/10.1126/science.287.5450.97`.

[154] B. P. Anderson, P. C. Haljan, C. A. Regal, D. L. Feder, L. A. Collins, C. W. Clark, and E. A. Cornell, “Watching dark solitons decay into vortex rings in a Bose-Einstein condensate”, *Phys. Rev. Lett.* **86**, 2926 (2001). URL `http://dx.doi.org/10.1103/PhysRevLett.86.2926`.

[155] Y. S. Kivshar, T. J. Alexander, and S. K. Turitsyn, “Nonlinear modes of a macroscopic quantum oscillator”, *Phys. Lett. A* **278**, 225 (2001). URL `http://www.sciencedirect.com/science/article/pii/S037596010000774X`.

[156] L. M. Pismen. *Vorticies in nonlinear fields* (Clarendon Press, ISBN: 9780198501671, 1990). URL `https://global.oup.com/academic/product/vortices-in-nonlinear-fields-9780198501671?cc=in&lang=en&`.

[157] W. H. Zurek, “Causality in condensates: gray solitons as relics of BEC formation”, *Phys. Rev. Lett.* **102**, 105702 (2009). URL `http://dx.doi.org/10.1103/PhysRevLett.102.105702`.

[158] B. Damski and W. H. Zurek, "Soliton creation during a Bose-Einstein condensation", *Phys. Rev. Lett.* **104**, 160404 (2010). URL `http://dx.doi.org/10.1103/PhysRevLett.104.160404`.

[159] J. Anglin, "Quantum canaries learn to fly", *Nat. Phys.* **4**, 437 (2008). URL `http://dx.doi.org/10.1038/nphys980`.

[160] R. G. Scott, T. E. Judd, and T. M. Fromhold, "Exploiting soliton decay and phase fluctuations in atom chip interferometry of Bose-Einstein condensates", *Phys. Rev. Lett.* **100**, 100402 (2008). URL `https://link.aps.org/doi/10.1103/PhysRevLett.100.100402`.

[161] M. I. Shaukat, E. V. Castro, and H. Terças, "Quantum dark solitons as qubits in Bose-Einstein condensates", *Phys. Rev. A* **95**, 053618 (2017). URL `https://link.aps.org/doi/10.1103/PhysRevA.95.053618`.

[162] A. L. Fetter and A. A. Svidzinsky, "Vortices in a trapped dilute Bose-Einstein condensate", *J. Phys. Condens. Matter* **13**, R135 (2001). URL `http://stacks.iop.org/0953-8984/13/i=12/a=201`.

[163] E. J. Yarmchuk, M. J. V. Gordon, and R. E. Packard, "Observation of stationary vortex arrays in rotating superfluid helium", *Phys. Rev. Lett.* **43**, 214 (1979). URL `https://link.aps.org/doi/10.1103/PhysRevLett.43.214`.

[164] E. Hodby, G. Hechenblaikner, S. A. Hopkins, O. M. Maragò, and C. J. Foot, "Vortex nucleation in Bose-Einstein condensates in an oblate, purely magnetic potential", *Phys. Rev. Lett.* **88**, 010405 (2001). URL `https://link.aps.org/doi/10.1103/PhysRevLett.88.010405`.

[165] J. R. Abo-Shaeer, C. Raman, J. M. Vogels, and W. Ketterle, "Observation of vortex lattices in Bose-Einstein condensates", *Science* **292**, 476 (2001). URL `http://science.sciencemag.org/content/292/5516/476`.

[166] W. H. Zurek, "Cosmological experiments in superfluid helium?", *Nature* **317**, 505 (1985). URL `http://dx.doi.org/10.1038/317505a0`.

[167] G. Lamporesi, S. Donadello, S. Serafini, F. Dalfovo, and G. Ferrari, "Spontaneous creation of Kibble-Zurek solitons in a Bose-Einstein condensate", *Nat. Phys.* **9**(10), 656 (2013). URL `http://dx.doi.org/10.1038/nphys2734`.

[168] P. C. Haljan, I. Coddington, P. Engels, and E. A. Cornell, "Driving Bose-Einstein condensate vorticity with a rotating normal cloud", *Phys. Rev. Lett.* **87**, 210403 (2001). URL `https://link.aps.org/doi/10.1103/PhysRevLett.87.210403`.

[169] M. R. Matthews, B. P. Anderson, P. C. Haljan, D. S. Hall, C. E. Wieman, and E. A. Cornell, "Vortices in a Bose-Einstein condensate", *Phys. Rev. Lett.* **83**, 2498 (1999). URL `https://link.aps.org/doi/10.1103/PhysRevLett.83.2498`.

[170] L. Dobrek, M. Gajda, M. Lewenstein, K. Sengstock, G. Birkl, and W. Ertmer, "Optical generation of vortices in trapped Bose-Einstein condensates", *Phys. Rev. A* **60**, R3381 (1999). URL `https://link.aps.org/doi/10.1103/PhysRevA.60.R3381`.

[171] S. Inouye, S. Gupta, T. Rosenband, A. P. Chikkatur, A. Görlitz, T. L. Gustavson, A. E. Leanhardt, D. E. Pritchard, and W. Ketterle, "Observation of vortex phase singularities in Bose-Einstein condensates", *Phys. Rev. Lett.* **87**, 080402 (2001). URL `https://link.aps.org/doi/10.1103/PhysRevLett.87.080402`.

[172] A. E. Leanhardt, A. Görlitz, A. P. Chikkatur, D. Kielpinski, Y. Shin, D. E. Pritchard, and W. Ketterle, "Imprinting vortices in a Bose-Einstein condensate using topological phases", *Phys. Rev. Lett.* **89**, 190403 (2002). URL `https://link.aps.org/doi/10.1103/PhysRevLett.89.190403`.

[173] E. A. L. Henn, J. A. Seman, G. Roati, K. M. F. Magalhães, and V. S. Bagnato, "Emergence of turbulence in an oscillating Bose-Einstein condensate", *Phys. Rev. Lett.* **103**, 045301 (2009). URL `https://link.aps.org/doi/10.1103/PhysRevLett.103.045301`.

[174] J. R. Abo-Shaeer, C. Raman, and W. Ketterle, "Formation and decay of vortex lattices in Bose-Einstein condensates at finite temperatures", *Phys. Rev. Lett.* **88**, 070409 (2002). URL `https://link.aps.org/doi/10.1103/PhysRevLett.88.070409`.

[175] W. J. Kwon, G. Moon, J.-y. Choi, S. W. Seo, and Y.-i. Shin, "Relaxation of superfluid turbulence in highly oblate Bose-Einstein condensates", *Phys. Rev. A* **90**, 063627 (2014). URL `http://dx.doi.org/10.1103/PhysRevA.90.063627`.

[176] T. W. Neely, E. C. Samson, A. S. Bradley, M. J. Davis, and B. P. Anderson, "Observation of vortex dipoles in an oblate Bose-Einstein condensate", *Phys. Rev. Lett.* **104**, 160401 (2010). URL `http://dx.doi.org/10.1103/PhysRevLett.104.160401`.

[177] P. Engels, I. Coddington, P. C. Haljan, V. Schweikhard, and E. A. Cornell, "Observation of long-lived vortex aggregates in rapidly rotating Bose-Einstein condensates", *Phys. Rev. Lett.* **90**, 170405 (2003). URL `https://link.aps.org/doi/10.1103/PhysRevLett.90.170405`.

[178] Y. Shin, M. Saba, M. Vengalattore, T. A. Pasquini, C. Sanner, A. E. Leanhardt, M. Prentiss, D. E. Pritchard, and W. Ketterle, "Dynamical instability of a doubly quantized vortex in a Bose-Einstein condensate", *Phys. Rev. Lett.* **93**, 160406 (2004). URL `https://link.aps.org/doi/10.1103/PhysRevLett.93.160406`.

[179] C. Raman, J. R. Abo-Shaeer, J. M. Vogels, K. Xu, and W. Ketterle, "Vortex nucleation in a stirred Bose-Einstein condensate", *Phys. Rev. Lett.* **87**, 210402 (2001). URL `https://link.aps.org/doi/10.1103/PhysRevLett.87.210402`.

[180] D. V. Freilich, D. M. Bianchi, A. M. Kaufman, T. K. Langin, and D. S. Hall, "Real-time dynamics of single vortex lines and vortex dipoles in a Bose-Einstein condensate", *Science* **329**(5996), 1182 (2010). URL `http://dx.doi.org/10.1126/science.1191224`.

[181] A. T. Powis, S. J. Sammut, and T. P. Simula, "Vortex gyroscope imaging of planar superfluids", *Phys. Rev. Lett.* **113**, 165303 (2014). URL `https://link.aps.org/doi/10.1103/PhysRevLett.113.165303`.

[182] K. Sasaki, N. Suzuki, and H. Saito, "Bénard–Von Kármán vortex street in a Bose-Einstein condensate", *Phys. Rev. Lett.* **104**, 150404 (2010). URL `https://link.aps.org/doi/10.1103/PhysRevLett.104.150404`.

[183] W. J. Kwon, J. H. Kim, S. W. Seo, and Y. Shin, “Observation of von kármán vortex street in an atomic superfluid gas”, *Phys. Rev. Lett.* **117**, 245301 (2016). URL `https://link.aps.org/doi/10.1103/PhysRevLett.117.245301`.

[184] K. Staliunas, S. Longhi, and G. J. de Valcárcel, “Faraday patterns in Bose-Einstein condensates”, *Phys. Rev. Lett.* **89**, 210406 (2002). URL `http://dx.doi.org/10.1103/PhysRevLett.89.210406`.

[185] S. Ronen, J. L. Bohn, L. E. Halmo, and M. Edwards, “Dynamical pattern formation during growth of a dual-species Bose-Einstein condensate”, *Phys. Rev. A* **78**, 053613 (2008). URL `https://link.aps.org/doi/10.1103/PhysRevA.78.053613`.

[186] M. Leadbeater, T. Winiecki, D. C. Samuels, C. F. Barenghi, and C. S. Adams, “Sound emission due to superfluid vortex reconnections”, *Phys. Rev. Lett.* **86**, 1410 (2001). URL `https://link.aps.org/doi/10.1103/PhysRevLett.86.1410`.

[187] M. Leadbeater, D. C. Samuels, C. F. Barenghi, and C. S. Adams, “Decay of superfluid turbulence via Kelvin-wave radiation”, *Phys. Rev. A* **67**, 015601 (2003). URL `https://link.aps.org/doi/10.1103/PhysRevA.67.015601`.

[188] N. G. Berloff, “Interactions of vortices with rarefaction solitary waves in a Bose-Einstein condensate and their role in the decay of superfluid turbulence”, *Phys. Rev. A* **69**, 053601 (2004). URL `https://link.aps.org/doi/10.1103/PhysRevA.69.053601`.

[189] A. C. White, B. P. Anderson, and V. S. Bagnato, “Vortices and turbulence in trapped atomic condensates”, *Proceedings of the National Academy of Sciences* **111**, 4719 (2014). URL `http://www.pnas.org/content/111/Supplement_1/4719`.

[190] R. Robinett, “Quantum wave packet revivals”, *Phys. Rep.* **392**, 1 (2004). URL `http://www.sciencedirect.com/science/article/pii/S0370157303004381`.

[191] G. Della Valle, M. Savoini, M. Ornigotti, P. Laporta, V. Foglietti, M. Finazzi, L. Duò, and S. Longhi, “Experimental observation of a photon bouncing ball”,

Phys. Rev. Lett. **102**, 180402 (2009). URL `https://link.aps.org/doi/10.1103/PhysRevLett.102.180402`.

[192] V. V. Nesvizhevsky, H. G. Brner, A. K. Petukhov, H. Abele, S. Baeler, F. J. Rue, T. Stferle, A. Westphal, A. M. Gagarski, G. A. Petrov, and A. V. Strelkov, "Quantum states of neutrons in the earth's gravitational field", *Nature* **415**, 297 (2002). URL `http://dx.doi.org/10.1038/415297a`.

[193] V. V. Nesvizhevsky, H. G. Börner, A. M. Gagarski, A. K. Petoukhov, G. A. Petrov, H. Abele, S. Baeßler, G. Divkovic, F. J. Rueß, T. Stöferle, A. Westphal, A. V. Strelkov, K. V. Protasov, and A. Y. Voronin, "Measurement of quantum states of neutrons in the earth's gravitational field", *Phys. Rev. D* **67**, 102002 (2003). URL `https://link.aps.org/doi/10.1103/PhysRevD.67.102002`.

[194] L. Viola and R. Onofrio, "Testing the equivalence principle through freely falling quantum objects", *Phys. Rev. D* **55**, 455 (1997). URL `https://link.aps.org/doi/10.1103/PhysRevD.55.455`.

[195] O. Bertolami and F. M. Nunes, "Ultracold neutrons, quantum effects of gravity and the weak equivalence principle", *Class. Quantum Grav.* **20**(5), L61 (2003). URL `http://stacks.iop.org/0264-9381/20/i=5/a=103`.

[196] G. Verma, U. D. Rapol, and R. Nath, "Generation of dark solitons and their instability dynamics in two-dimensional condensates", *Phys. Rev. A* **95**, 043618 (2017). URL `https://link.aps.org/doi/10.1103/PhysRevA.95.043618`.

[197] N. Parker. *Numerical studies of vortices and dark solitons in atomic Bose-Einstein condensates.* Ph.D. thesis, University of Durham (2004). URL `http://etheses.dur.ac.uk/3014/`.

[198] P. Hohenberg and P. Martin, "Microscopic theory of superfluid helium", *Ann. Phys.* **34**, 291 (1965). URL `http://www.sciencedirect.com/science/article/pii/0003491665902800`.

[199] N. P. Proukakis and B. Jackson, "Finite-temperature models of Bose-Einstein condensation", *J. Phys. B: At. Mol. Opt. Phys.* **41**, 203002 (2008). URL `http://stacks.iop.org/0953-4075/41/i=20/a=203002`.

[200] P. Roberts and N. Berloff. *Quantized vortex dynamics and superfluid turbulence* (Springer-Verlag Berlin Heidelberg, ISBN: 978-3-540-42226-6, 2001). URL `https://www.springer.com/in/book/9783540422266`.

[201] L. Warszawski and A. Melatos, "Gross-Pitaevskii model of pulsar glitches", *Mon. Notices Royal Astron. Soc.* **415**, 1611 (2011). URL `http://adsabs.harvard.edu/abs/2011MNRAS.415.1611W`.

[202] D. S. Petrov, G. V. Shlyapnikov, and J. T. M. Walraven, "Regimes of quantum degeneracy in trapped 1d gases", *Phys. Rev. Lett.* **85**, 3745 (2000). URL `https://link.aps.org/doi/10.1103/PhysRevLett.85.3745`.

[203] A. Görlitz, J. M. Vogels, A. E. Leanhardt, C. Raman, T. L. Gustavson, J. R. Abo-Shaeer, A. P. Chikkatur, S. Gupta, S. Inouye, T. Rosenband, and W. Ketterle, "Realization of Bose-Einstein condensates in lower dimensions", *Phys. Rev. Lett.* **87**, 130402 (2001). URL `https://link.aps.org/doi/10.1103/PhysRevLett.87.130402`.

[204] W. Bao and W. Tang, "Ground-state solution of Bose-Einstein condensate by directly minimizing the energy functional", *J. Comput. Phys.* **187**, 230 (2003). URL `http://www.sciencedirect.com/science/article/pii/S0021999103000974`.

[205] J. M. Thijssen. *Computational physics* (Cambridge University Press, ISBN: 0521575885, 1999). URL `https://books.google.co.in/books?id=flolqBpoJeEC&source=gbs_book_other_versions`.

[206] M. Edwards and K. Burnett, "Numerical solution of the nonlinear Schrödinger equation for small samples of trapped neutral atoms", *Phys. Rev. A* **51**, 1382 (1995). URL `https://link.aps.org/doi/10.1103/PhysRevA.51.1382`.

[207] M. L. Chiofalo, S. Succi, and M. P. Tosi, "Ground state of trapped interacting Bose-Einstein condensates by an explicit imaginary-time algorithm", *Phys. Rev. E* **62**, 7438 (2000). URL `https://link.aps.org/doi/10.1103/PhysRevE.62.7438`.

[208] J. A. C. Weideman and B. M. Herbst, "Split-step methods for the solution of the nonlinear Schrödinger equation", *SIAM J. Numer. Anal.* **23**, 485 (1986). URL `http://www.jstor.org/stable/2157521`.

[209] A. Muryshev, G. V. Shlyapnikov, W. Ertmer, K. Sengstock, and M. Lewenstein, "Dynamics of dark solitons in elongated Bose-Einstein condensates", *Phys. Rev. Lett.* **89**, 110401 (2002). URL `http://dx.doi.org/10.1103/PhysRevLett.89.110401`.

[210] A. V. Mamaev, M. Saffman, and A. A. Zozulya, "Propagation of dark stripe beams in nonlinear media: snake instability and creation of optical vortices", *Phys. Rev. Lett.* **76**, 2262 (1996). URL `http://dx.doi.org/10.1103/PhysRevLett.76.2262`.

[211] A. E. Muryshev, H. B. van Linden van den Heuvell, and G. V. Shlyapnikov, "Stability of standing matter waves in a trap", *Phys. Rev. A* **60**, R2665 (1999). URL `http://dx.doi.org/10.1103/PhysRevA.60.R2665`.

[212] P. O. Fedichev, A. E. Muryshev, and G. V. Shlyapnikov, "Dissipative dynamics of a kink state in a Bose-condensed gas", *Phys. Rev. A* **60**, 3220 (1999). URL `https://link.aps.org/doi/10.1103/PhysRevA.60.3220`.

[213] T. Busch and J. R. Anglin, "Motion of dark solitons in trapped Bose-Einstein condensates", *Phys. Rev. Lett.* **84**, 2298 (2000). URL `http://dx.doi.org/10.1103/PhysRevLett.84.2298`.

[214] G. Huang, J. Szeftel, and S. Zhu, "Dynamics of dark solitons in quasi-one-dimensional Bose-Einstein condensates", *Phys. Rev. A* **65**, 053605 (2002). URL `https://link.aps.org/doi/10.1103/PhysRevA.65.053605`.

[215] J. Dziarmaga, Z. P. Karkuszewski, and K. Sacha, "Images of the dark soliton in a depleted condensate", *J. Phys. B: At. Mol. Opt. Phys.* **36**, 1217 (2003). URL `http://stacks.iop.org/0953-4075/36/i=6/a=311`.

[216] G. Theocharis, D. J. Frantzeskakis, P. G. Kevrekidis, B. A. Malomed, and Y. S. Kivshar, "Ring dark solitons and vortex necklaces in Bose-Einstein condensates", *Phys. Rev. Lett.* **90**, 120403 (2003). URL `https://link.aps.org/doi/10.1103/PhysRevLett.90.120403`.

[217] L. D. Carr and C. W. Clark, "Vortices and ring solitons in Bose-Einstein condensates", *Phys. Rev. A* **74**, 043613 (2006). URL `https://link.aps.org/doi/10.1103/PhysRevA.74.043613`.

[218] R. Nath, P. Pedri, and L. Santos, "Stability of dark solitons in three dimensional dipolar Bose-Einstein condensates", *Phys. Rev. Lett.* **101**, 210402 (2008). URL `https://link.aps.org/doi/10.1103/PhysRevLett.101.210402`.

[219] M. Faraday, "On a peculiar class of acoustical figures; and on certain forms assumed by groups of particles upon vibrating elastic surfaces", *Phil. Trans. R. Soc.* **3**, 49 (1830). URL `http://www.jstor.org/stable/110265`.

[220] P. Engels, C. Atherton, and M. A. Hoefer, "Observation of Faraday waves in a Bose-Einstein condensate", *Phys. Rev. Lett.* **98**, 095301 (2007). URL `https://link.aps.org/doi/10.1103/PhysRevLett.98.095301`.

[221] K. Staliunas, S. Longhi, and G. J. de Valcárcel, "Faraday patterns in low-dimensional Bose-Einstein condensates", *Phys. Rev. A* **70**, 011601 (2004). URL `https://link.aps.org/doi/10.1103/PhysRevA.70.011601`.

[222] A. I. Nicolin, R. Carretero-González, and P. G. Kevrekidis, "Faraday waves in Bose-Einstein condensates", *Phys. Rev. A* **76**, 063609 (2007). URL `https://link.aps.org/doi/10.1103/PhysRevA.76.063609`.

[223] A. B. Bhattacherjee, "Faraday instability in a two-component Bose-Einstein condensate", *Phys. Scr.* **78**, 045009 (2008). URL `http://stacks.iop.org/1402-4896/78/i=4/a=045009`.

[224] R. Nath and L. Santos, "Faraday patterns in two-dimensional dipolar Bose-Einstein condensates", *Phys. Rev. A* **81**, 033626 (2010). URL `https://link.aps.org/doi/10.1103/PhysRevA.81.033626`.

[225] Y. S. Kivshar and B. Luther-Davies, "Dark optical solitons: physics and applications", *Phys. Rep.* **298**(2–3), 81 (1998). URL `http://dx.doi.org/10.1016/S0370-1573(97)00073-2`.

[226] P. G. Kevrekidis, D. J. Frantzeskakis, and R. Carretero-González. *The defocusing nonlinear Schrödinger equation: from dark solitons to vortices and vortex rings* (Society for Industrial and Applied Mathematics, ISBN: 978-1-61197-393-8, 2015). URL `https://doi.org/10.1137/1.9781611973945`.

[227] N. Meyer, H. Proud, M. Perea-Ortiz, C. O'Neale, M. Baumert, M. Holynski, J. Kronjäger, G. Barontini, and K. Bongs, "Observation of two-dimensional localized Jones-Roberts solitons in Bose-Einstein condensates", *Phys. Rev. Lett.* **119**, 150403 (2017). URL `https://link.aps.org/doi/10.1103/PhysRevLett.119.150403`.

[228] J. J. Chang, P. Engels, and M. A. Hoefer, "Formation of dispersive shock waves by merging and splitting Bose-Einstein condensates", *Phys. Rev. Lett.* **101**, 170404 (2008). URL `http://dx.doi.org/10.1103/PhysRevLett.101.170404`.

[229] F. K. Abdullaev, A. M. Kamchatnov, V. V. Konotop, and V. A. Brazhnyi, "Adiabatic dynamics of periodic waves in Bose-Einstein condensates with time dependent atomic scattering length", *Phys. Rev. Lett.* **90**, 230402 (2003). URL `http://dx.doi.org/10.1103/PhysRevLett.90.230402`.

[230] L. D. Carr, J. Brand, S. Burger, and A. Sanpera, "Dark-soliton creation in Bose-Einstein condensates", *Phys. Rev. A* **63**, 051601 (2001). URL `http://dx.doi.org/10.1103/PhysRevA.63.051601`.

[231] S. Burger, L. D. Carr, P. Öhberg, K. Sengstock, and A. Sanpera, "Generation and interaction of solitons in Bose-Einstein condensates", *Phys. Rev. A* **65**, 043611 (2002). URL `http://dx.doi.org/10.1103/PhysRevA.65.043611`.

[232] C. Becker, S. Stellmer, P. Soltan-Panahi, S. Dorscher, M. Baumert, E.-M. Richter, J. Kronjager, K. Bongs, and K. Sengstock, "Oscillations and interactions of dark and dark-bright solitons in Bose-Einstein condensates", *Nat. Phys.* **4**(6), 496 (2008). URL `http://dx.doi.org/10.1038/nphys962`.

[233] P. Engels and C. Atherton, "Stationary and nonstationary fluid flow of a Bose-Einstein condensate through a penetrable barrier", *Phys. Rev. Lett.* **99**, 160405 (2007). URL `http://dx.doi.org/10.1103/PhysRevLett.99.160405`.

[234] I. Shomroni, E. Lahoud, S. Levy, and J. Steinhauer, "Evidence for an oscillating soliton/vortex ring by density engineering of a Bose-Einstein condensate", *Nat. Phys.* **5**(3), 193 (2009). URL `http://dx.doi.org/10.1038/nphys1177`.

[235] A. Weller, J. P. Ronzheimer, C. Gross, J. Esteve, M. K. Oberthaler, D. J. Frantzeskakis, G. Theocharis, and P. G. Kevrekidis, “Experimental observation of oscillating and interacting matter wave dark solitons”, *Phys. Rev. Lett.* **101**, 130401 (2008). URL `http://dx.doi.org/10.1103/PhysRevLett.101.130401`.

[236] D. R. Scherer, C. N. Weiler, T. W. Neely, and B. P. Anderson, “Vortex formation by merging of multiple trapped Bose-Einstein condensates”, *Phys. Rev. Lett.* **98**, 110402 (2007). URL `http://dx.doi.org/10.1103/PhysRevLett.98.110402`.

[237] B. Wu, J. Liu, and Q. Niu, “Controlled generation of dark solitons with phase imprinting”, *Phys. Rev. Lett.* **88**, 034101 (2002). URL `http://dx.doi.org/10.1103/PhysRevLett.88.034101`.

[238] P. G. Kevrekidis, G. Theocharis, D. J. Frantzeskakis, and B. A. Malomed, “Feshbach resonance management for Bose-Einstein condensates”, *Phys. Rev. Lett.* **90**, 230401 (2003). URL `http://dx.doi.org/10.1103/PhysRevLett.90.230401`.

[239] D. Gallucci and N. P. Proukakis, “Engineering dark solitary waves in ring-trap Bose–Einstein condensates”, *New J. Phys.* **18**(2), 025004 (2016). URL `http://stacks.iop.org/1367-2630/18/i=2/a=025004`.

[240] G. Theocharis, P. Kevrekidis, H. Nistazakis, D. Frantzeskakis, and A. Bishop, “Generation of dark solitons in oscillating Bose–Einstein condensates”, *Phys. Lett. A* **337**(4–6), 441 (2005). URL `http://dx.doi.org/10.1016/j.physleta.2005.01.068`.

[241] G. Theocharis, P. Schmelcher, P. G. Kevrekidis, and D. J. Frantzeskakis, “Matter-wave solitons of collisionally inhomogeneous condensates”, *Phys. Rev. A* **72**, 033614 (2005). URL `http://dx.doi.org/10.1103/PhysRevA.72.033614`.

[242] A. Radouani, “Soliton and phonon production by an oscillating obstacle in a quasi-one-dimensional trapped repulsive Bose-Einstein condensate”, *Phys. Rev. A* **70**, 013602 (2004). URL `http://dx.doi.org/10.1103/PhysRevA.70.013602`.

[243] A. D. Jackson, G. M. Kavoulakis, and C. J. Pethick, “Solitary waves in clouds of Bose-Einstein condensed atoms”, *Phys. Rev. A* **58**, 2417 (1998). URL `http://dx.doi.org/10.1103/PhysRevA.58.2417`.

[244] E. A. Kuznetsov and J. J. Rasmussen, “Instability of two-dimensional solitons and vortices in defocusing media”, *Phys. Rev. E* **51**, 4479 (1995). URL `http://dx.doi.org/10.1103/PhysRevE.51.4479`.

[245] G. Huang, V. A. Makarov, and M. G. Velarde, “Two-dimensional solitons in Bose-Einstein condensates with a disk-shaped trap”, *Phys. Rev. A* **67**, 023604 (2003). URL `http://dx.doi.org/10.1103/PhysRevA.67.023604`.

[246] N. G. Parker, N. P. Proukakis, M. Leadbeater, and C. S. Adams, “Soliton-sound interactions in quasi-one-dimensional Bose-Einstein condensates”, *Phys. Rev. Lett.* **90**, 220401 (2003). URL `http://dx.doi.org/10.1103/PhysRevLett.90.220401`.

[247] N. P. Proukakis, N. G. Parker, C. F. Barenghi, and C. S. Adams, “Parametric driving of dark solitons in atomic Bose-Einstein condensates”, *Phys. Rev. Lett.* **93**, 130408 (2004). URL `http://dx.doi.org/10.1103/PhysRevLett.93.130408`.

[248] D. E. Pelinovsky, D. J. Frantzeskakis, and P. G. Kevrekidis, “Oscillations of dark solitons in trapped Bose-Einstein condensates”, *Phys. Rev. E* **72**, 016615 (2005). URL `http://dx.doi.org/10.1103/PhysRevE.72.016615`.

[249] N. G. Parker, N. P. Proukakis, M. Leadbeater, and C. S. Adams, “Deformation of dark solitons in inhomogeneous Bose–Einstein condensates”, *J. Phys. B: At. Mol. Opt. Phys.* **36**(13), 2891 (2003). URL `http://stacks.iop.org/0953-4075/36/i=13/a=318`.

[250] B. A. Malomed, H. E. Nistazakis, D. J. Frantzeskakis, and P. G. Kevrekidis, “Static and rotating domain-wall cross patterns in Bose-Einstein condensates”, *Phys. Rev. A* **70**, 043616 (2004). URL `http://dx.doi.org/10.1103/PhysRevA.70.043616`.

[251] G. Huang, L. Deng, and C. Hang, “Davey-stewartson description of two-dimensional nonlinear excitations in Bose-Einstein condensates”, *Phys. Rev. E* **72**, 036621 (2005). URL `http://dx.doi.org/10.1103/PhysRevE.72.036621`.

[252] A. Gallemí, M. Guilleumas, R. Mayol, and A. M. Mateo, "Multidimensional josephson vortices in spin-orbit-coupled Bose-Einstein condensates: Snake instability and decay through vortex dipoles", *Phys. Rev. A* **93**, 033618 (2016). URL `http://dx.doi.org/10.1103/PhysRevA.93.033618`.

[253] C. T. Law and G. A. Swartzlander, "Optical vortex solitons and the stability of dark soliton stripes", *Opt. Lett.* **18**(8), 586 (1993). URL `http://dx.doi.org/10.1364/OL.18.000586`.

[254] G. McDonald, K. Syed, and W. Firth, "Dark spatial soliton break-up in the transverse plane", *Opt. Commun.* **95**(4), 281 (1993). URL `http://dx.doi.org/10.1016/0030-4018(93)90679-Y`.

[255] Y. S. Kivshar and D. E. Pelinovsky, "Self-focusing and transverse instabilities of solitary waves", *Phys. Rep.* **331**(4), 117 (2000). URL `http://dx.doi.org/10.1016/S0370-1573(99)00106-4`.

[256] P. G. Kevrekidis, G. Theocharis, D. J. Frantzeskakis, and A. Trombettoni, "Avoiding infrared catastrophes in trapped Bose-Einstein condensates", *Phys. Rev. A* **70**, 023602 (2004). URL `http://dx.doi.org/10.1103/PhysRevA.70.023602`.

[257] M. Ma, R. Carretero-González, P. G. Kevrekidis, D. J. Frantzeskakis, and B. A. Malomed, "Controlling the transverse instability of dark solitons and nucleation of vortices by a potential barrier", *Phys. Rev. A* **82**, 023621 (2010). URL `http://dx.doi.org/10.1103/PhysRevA.82.023621`.

[258] L. A. Toikka and K.-A. Suominen, "Snake instability of ring dark solitons in toroidally trapped Bose-Einstein condensates", *Phys. Rev. A* **87**, 043601 (2013). URL `http://dx.doi.org/10.1103/PhysRevA.87.043601`.

[259] A. Cetoli, J. Brand, R. G. Scott, F. Dalfovo, and L. P. Pitaevskii, "Snake instability of dark solitons in fermionic superfluids", *Phys. Rev. A* **88**, 043639 (2013). URL `http://dx.doi.org/10.1103/PhysRevA.88.043639`.

[260] S. Middelkamp, P. G. Kevrekidis, D. J. Frantzeskakis, R. Carretero-González, and P. Schmelcher, "Bifurcations, stability, and dynamics of multiple matter-wave vortex states", *Phys. Rev. A* **82**, 013646 (2010). URL `http://dx.doi.org/10.1103/PhysRevA.82.013646`.

[261] D. S. Rokhsar, "Vortex stability and persistent currents in trapped Bose gases", *Phys. Rev. Lett.* **79**, 2164 (1997). URL `http://dx.doi.org/10.1103/PhysRevLett.79.2164`.

[262] E. J. M. Madarassy and C. F. Barenghi, "Vortex dynamics in trapped Bose-Einstein condensate", *J. Low Temp. Phys.* **152**(3), 122 (2008). URL `http://dx.doi.org/10.1007/s10909-008-9811-9`.

[263] R. Navarro, R. Carretero-González, P. J. Torres, P. G. Kevrekidis, D. J. Frantzeskakis, M. W. Ray, E. Altuntaş, and D. S. Hall, "Dynamics of a few corotating vortices in Bose-Einstein condensates", *Phys. Rev. Lett.* **110**, 225301 (2013). URL `http://dx.doi.org/10.1103/PhysRevLett.110.225301`.

[264] L.-C. Crasovan, V. Vekslerchik, V. M. Pérez-García, J. P. Torres, D. Mihalache, and L. Torner, "Stable vortex dipoles in nonrotating Bose-Einstein condensates", *Phys. Rev. A* **68**, 063609 (2003). URL `http://dx.doi.org/10.1103/PhysRevA.68.063609`.

[265] Q. Zhou and H. Zhai, "Vortex dipole in a trapped atomic Bose-Einstein condensate", *Phys. Rev. A* **70**, 043619 (2004). URL `http://dx.doi.org/10.1103/PhysRevA.70.043619`.

[266] M. Möttönen, S. M. M. Virtanen, T. Isoshima, and M. M. Salomaa, "Stationary vortex clusters in nonrotating Bose-Einstein condensates", *Phys. Rev. A* **71**, 033626 (2005). URL `http://dx.doi.org/10.1103/PhysRevA.71.033626`.

[267] V. Pietilä, M. Möttönen, T. Isoshima, J. A. M. Huhtamäki, and S. M. M. Virtanen, "Stability and dynamics of vortex clusters in nonrotated Bose-Einstein condensates", *Phys. Rev. A* **74**, 023603 (2006). URL `http://dx.doi.org/10.1103/PhysRevA.74.023603`.

[268] A. Klein, D. Jaksch, Y. Zhang, and W. Bao, "Dynamics of vortices in weakly interacting Bose-Einstein condensates", *Phys. Rev. A* **76**, 043602 (2007). URL `http://dx.doi.org/10.1103/PhysRevA.76.043602`.

[269] W. Li, M. Haque, and S. Komineas, "Vortex dipole in a trapped two-dimensional Bose-Einstein condensate", *Phys. Rev. A* **77**, 053610 (2008). URL `http://dx.doi.org/10.1103/PhysRevA.77.053610`.

[270] P. Torres, P. Kevrekidis, D. Frantzeskakis, R. Carretero-González, P. Schmelcher, and D. Hall, "Dynamics of vortex dipoles in confined Bose–Einstein condensates", *Phys. Lett. A* **375**(33), 3044 (2011). URL `http://dx.doi.org/10.1016/j.physleta.2011.06.061`.

[271] P. Kuopanportti, J. A. M. Huhtamäki, and M. Möttönen, "Size and dynamics of vortex dipoles in dilute Bose-Einstein condensates", *Phys. Rev. A* **83**, 011603 (2011). URL `http://dx.doi.org/10.1103/PhysRevA.83.011603`.

[272] S. Middelkamp, P. J. Torres, P. G. Kevrekidis, D. J. Frantzeskakis, R. Carretero-González, P. Schmelcher, D. V. Freilich, and D. S. Hall, "Guiding-center dynamics of vortex dipoles in Bose-Einstein condensates", *Phys. Rev. A* **84**, 011605 (2011). URL `http://dx.doi.org/10.1103/PhysRevA.84.011605`.

[273] W. J. Kwon, S. W. Seo, and Y.-i. Shin, "Periodic shedding of vortex dipoles from a moving penetrable obstacle in a Bose-Einstein condensate", *Phys. Rev. A* **92**, 033613 (2015). URL `http://dx.doi.org/10.1103/PhysRevA.92.033613`.

[274] R. H. Goodman, P. G. Kevrekidis, and R. Carretero-González, "Dynamics of vortex dipoles in anisotropic Bose–Einstein condensates", *SIAM J. Appl. Dyn. Syst.* **14**(2), 699 (2015). URL `http://dx.doi.org/10.1137/140992345`.

[275] S. Prabhakar, R. P. Singh, S. Gautam, and D. Angom, "Annihilation of vortex dipoles in an oblate Bose–Einstein condensate", *J. Phys. B: At. Mol. Opt. Phys.* **46**(12), 125302 (2013). URL `http://stacks.iop.org/0953-4075/46/i=12/a=125302`.

[276] G. W. Stagg, A. J. Allen, N. G. Parker, and C. F. Barenghi, "Generation and decay of two-dimensional quantum turbulence in a trapped Bose-Einstein condensate", *Phys. Rev. A* **91**, 013612 (2015). URL `http://dx.doi.org/10.1103/PhysRevA.91.013612`.

[277] Y. Du, C. Niu, Y. Tian, and H. Zhang, "Holographic thermal relaxation in superfluid turbulence", *J. High Energy Phys.* **2015**(12), 18 (2015). URL `http://dx.doi.org/10.1007/JHEP12(2015)018`.

[278] C. Rorai, K. R. Sreenivasan, and M. E. Fisher, "Propagating and annihilating vortex dipoles in the gross-pitaevskii equation", *Phys. Rev. B* **88**, 134522 (2013). URL `http://dx.doi.org/10.1103/PhysRevB.88.134522`.

[279] T. Simula, M. J. Davis, and K. Helmerson, "Emergence of order from turbulence in an isolated planar superfluid", *Phys. Rev. Lett.* **113**, 165302 (2014). URL `http://dx.doi.org/10.1103/PhysRevLett.113.165302`.

[280] A. J. Groszek, T. P. Simula, D. M. Paganin, and K. Helmerson, "Onsager vortex formation in Bose-Einstein condensates in two-dimensional power-law traps", *Phys. Rev. A* **93**, 043614 (2016).

[281] W. P. Reinhardt and S. B. McKinney, "Dynamical and wave chaos in the Bose–Einstein condensate", *Phys. Scr.* **2001**(T90), 202 (2001). URL `http://stacks.iop.org/1402-4896/2001/i=T90/a=030`.

[282] V. V. Konotop and V. E. Vekslerchik, "Randomly modulated dark soliton", *J. Phys. A: Math. Gen.* **24**(4), 767 (1991). URL `http://stacks.iop.org/0305-4470/24/i=4/a=013`.

[283] V. V. Konotop and L. Pitaevskii, "Landau dynamics of a grey soliton in a trapped condensate", *Phys. Rev. Lett.* **93**, 240403 (2004). URL `http://dx.doi.org/10.1103/PhysRevLett.93.240403`.

[284] V. A. Brazhnyi, V. V. Konotop, and L. P. Pitaevskii, "Dark solitons as quasiparticles in trapped condensates", *Phys. Rev. A* **73**, 053601 (2006). URL `http://dx.doi.org/10.1103/PhysRevA.73.053601`.

[285] A. M. Mateo and J. Brand, "Stability and dispersion relations of three-dimensional solitary waves in trapped Bose–Einstein condensates", *New J. Phys.* **17**(12), 125013 (2015). URL `http://stacks.iop.org/1367-2630/17/i=12/a=125013`.

[286] L. A. Smirnov and A. I. Smirnov, "Scattering of two-dimensional dark solitons by a single quantum vortex in a Bose-Einstein condensate", *Phys. Rev. A* **92**, 013636 (2015). URL `http://dx.doi.org/10.1103/PhysRevA.92.013636`.

[287] C. Lee, E. A. Ostrovskaya, and Y. S. Kivshar, "Nonlinearity-assisted quantum tunnelling in a matter-wave interferometer", *J. Phys. B: At. Mol. Opt. Phys.* **40**(21), 4235 (2007). URL `http://stacks.iop.org/0953-4075/40/i=21/a=010`.

[288] T. F. Scott, R. J. Ballagh, and K. Burnett, "Formation of fundamental structures in Bose-Einstein condensates", *J. Phys. B: At. Mol. Opt. Phys.* **31**(8), L329 (1998). URL `http://stacks.iop.org/0953-4075/31/i=8/a=001`.

[289] S. E. Pollack, D. Dries, R. G. Hulet, K. M. F. Magalhães, E. A. L. Henn, E. R. F. Ramos, M. A. Caracanhas, and V. S. Bagnato, "Collective excitation of a Bose-Einstein condensate by modulation of the atomic scattering length", *Phys. Rev. A* **81**, 053627 (2010). URL `http://dx.doi.org/10.1103/PhysRevA.81.053627`.

[290] H. Pu, P. Maenner, W. Zhang, and H. Y. Ling, "Adiabatic condition for nonlinear systems", *Phys. Rev. Lett.* **98**, 050406 (2007). URL `http://dx.doi.org/10.1103/PhysRevLett.98.050406`.

[291] Y. B. Band, B. Malomed, and M. Trippenbach, "Adiabaticity in nonlinear quantum dynamics: Bose-Einstein condensate in a time-varying box", *Phys. Rev. A* **65**, 033607 (2002). URL `http://dx.doi.org/10.1103/PhysRevA.65.033607`.

[292] M. Theis, G. Thalhammer, K. Winkler, M. Hellwig, G. Ruff, R. Grimm, and J. H. Denschlag, "Tuning the scattering length with an optically induced Feshbach resonance", *Phys. Rev. Lett.* **93**, 123001 (2004). URL `https://link.aps.org/doi/10.1103/PhysRevLett.93.123001`.

[293] G. Thalhammer, M. Theis, K. Winkler, R. Grimm, and J. H. Denschlag, “Inducing an optical Feshbach resonance via stimulated raman coupling”, *Phys. Rev. A* **71**, 033403 (2005). URL `https://link.aps.org/doi/10.1103/PhysRevA.71.033403`.

[294] K. Bongs, S. Burger, G. Birkl, K. Sengstock, K. Ertmer, W. andRzażėwski, A. Sanpera, and M. Lewenstein, “Coherent evolution of bouncing Bose-Einstein condensates”, *Phys. Rev. Lett.* **83**, 3577 (1999). URL `https://link.aps.org/doi/10.1103/PhysRevLett.83.3577`.

[295] C. G. Townsend, N. H. Edwards, C. J. Cooper, K. P. Zetie, C. J. Foot, A. M. Steane, P. Szriftgiser, H. Perrin, and J. Dalibard, “Phase-space density in the magneto-optical trap”, *Phys. Rev. A* **52**, 1423 (1995). URL `https://link.aps.org/doi/10.1103/PhysRevA.52.1423`.

[296] K. Dieckmann. *Bose-Einstein condensation with high atom number in a deep magnetic trap.* Ph.D. thesis, University of Amsterdam (2001).

[297] S. Friebel, C. D’Andrea, J. Walz, M. Weitz, and T. W. Hänsch, “CO_2-laser optical lattice with cold rubidium atoms”, *Phys. Rev. A* **57**, R20 (1998). URL `https://link.aps.org/doi/10.1103/PhysRevA.57.R20`.

[298] R. Jáuregui, “Nonperturbative and perturbative treatments of parametric heating in atom traps”, *Phys. Rev. A* **64**, 053408 (2001). URL `https://link.aps.org/doi/10.1103/PhysRevA.64.053408`.

[299] V. L. Berezinskii, “Destruction of long-range order in one-dimensional and two-dimensional system possessing a continuous symmetry group - II quantum systems”, *J. Exp. Theor. Phys.* **34**, 610 (1971).

[300] J. M. Kosterlitz and D. J. Thouless, “Ordering, metastability and phase transitions in two-dimensional systems”, *J. Phys. Condens. Matter* **6**, 1181 (1973). URL `http://stacks.iop.org/0022-3719/6/i=7/a=010`.

[301] J. M. Kosterlitz, “The critical properties of the two-dimensional xy model”, *J. Phys. Condens. Matter* **7**, 1046 (1974). URL `http://stacks.iop.org/0022-3719/7/i=6/a=005`.

[302] K. J. Strandburg, “Two-dimensional melting”, *Rev. Mod. Phys.* **60**, 161 (1988). URL `https://link.aps.org/doi/10.1103/RevModPhys.60.161`.

[303] D. R. Nelson and B. I. Halperin, “Dislocation-mediated melting in two dimensions”, *Phys. Rev. B* **19**, 2457 (1979). URL `https://link.aps.org/doi/10.1103/PhysRevB.19.2457`.

[304] P. Cladé, C. Ryu, A. Ramanathan, K. Helmerson, and W. D. Phillips, “Observation of a 2d Bose gas: from thermal to quasicondensate to superfluid”, *Phys. Rev. Lett.* **102**, 170401 (2009). URL `https://link.aps.org/doi/10.1103/PhysRevLett.102.170401`.

[305] S. Tung, G. Lamporesi, D. Lobser, L. Xia, and E. A. Cornell, “Observation of the presuperfluid regime in a two-dimensional Bose gas”, *Phys. Rev. Lett.* **105**, 230408 (2010). URL `https://link.aps.org/doi/10.1103/PhysRevLett.105.230408`.

[306] J.-y. Choi, S. W. Seo, W. J. Kwon, and Y.-i. Shin, “Probing phase fluctuations in a 2d degenerate Bose gas by free expansion”, *Phys. Rev. Lett.* **109**, 125301 (2012). URL `https://link.aps.org/doi/10.1103/PhysRevLett.109.125301`.

[307] J.-y. Choi, S. W. Seo, and Y.-i. Shin, “Observation of thermally activated vortex pairs in a quasi-2d Bose gas”, *Phys. Rev. Lett.* **110**, 175302 (2013). URL `https://link.aps.org/doi/10.1103/PhysRevLett.110.175302`.

[308] S. W. Seo, J.-y. Choi, and Y.-i. Shin, “Scaling behavior of density fluctuations in an expanding quasi-two-dimensional degenerate Bose gas”, *Phys. Rev. A* **89**, 043606 (2014). URL `https://link.aps.org/doi/10.1103/PhysRevA.89.043606`.

[309] V. Schweikhard, S. Tung, and E. A. Cornell, “Vortex proliferation in the Berezinskii-Kosterlitz-Thouless regime on a two-dimensional lattice of Bose-Einstein condensates”, *Phys. Rev. Lett.* **99**, 030401 (2007). URL `https://link.aps.org/doi/10.1103/PhysRevLett.99.030401`.

[310] Z. Hadzibabic and J. Dalibard, “Two-dimensional Bose fluids: An atomic physics perspective”, *La Rivista del Nuovo Cimento* **34**, 389 (2011). URL `https://www.sif.it/riviste/sif/ncr/econtents/2011/034/06/article/0`.

[311] D. Rychtarik, B. Engeser, H.-C. Nägerl, and R. Grimm, "Two-dimensional Bose-Einstein condensate in an optical surface trap", *Phys. Rev. Lett.* **92**, 173003 (2004). URL `https://link.aps.org/doi/10.1103/PhysRevLett.92.173003`.

[312] J. I. Gillen, W. S. Bakr, A. Peng, P. Unterwaditzer, S. Fölling, and M. Greiner, "Two-dimensional quantum gas in a hybrid surface trap", *Phys. Rev. A* **80**, 021602 (2009). URL `https://link.aps.org/doi/10.1103/PhysRevA.80.021602`.

[313] N. L. Smith, W. H. Heathcote, G. Hechenblaikner, E. Nugent, and C. J. Foot, "Quasi-2d confinement of a BEC in a combined optical and magnetic potential", *J. Phys. B: At. Mol. Opt. Phys.* **38**, 223 (2005). URL `http://stacks.iop.org/0953-4075/38/i=3/a=007`.

[314] C. Orzel, A. K. Tuchman, M. L. Fenselau, M. Yasuda, and M. A. Kasevich, "Squeezed states in a Bose-Einstein condensate", *Science* **291**, 2386 (2001). URL `http://science.sciencemag.org/content/291/5512/2386`.

[315] S. Burger, F. S. Cataliotti, C. Fort, P. Maddaloni, F. Minardi, and M. Inguscio, "Quasi-2d Bose-Einstein condensation in an optical lattice", *Euro. phys. Lett.* **57**, 1 (2002). URL `http://stacks.iop.org/0295-5075/57/i=1/a=001`.

[316] I. B. Spielman, W. D. Phillips, and J. V. Porto, "Mott-insulator transition in a two-dimensional atomic Bose gas", *Phys. Rev. Lett.* **98**, 080404 (2007). URL `https://link.aps.org/doi/10.1103/PhysRevLett.98.080404`.

[317] Z. Hadzibabic, S. Stock, B. Battelier, V. Bretin, and J. Dalibard, "Interference of an array of independent Bose-Einstein condensates", *Phys. Rev. Lett.* **93**, 180403 (2004). URL `https://link.aps.org/doi/10.1103/PhysRevLett.93.180403`.

[318] L. Chomaz. *Coherence and superfluidity of Bose gases in reduced dimensions : from harmonic traps to uniform fluids.* Ph.D. thesis, Ecole normale suprieure - ENS PARIS (2014). URL `https://tel.archives-ouvertes.fr/tel-01449982`.

[319] L. Corman. *The two-dimensional Bose gas in box potentials.* Ph.D. thesis, PSL Research University (2016). URL `https://tel.archives-ouvertes.fr/tel-01357602/`.

[320] J.-L. Ville. *Quantum gases in box potentials: sound and light in bosonic flatland.* Ph.D. thesis, PSL Research University (2018).